UNIVERSITY of TASMANIA

Direct georeferencing and footprint characterisation of a non-imaging spectroradiometer mounted on an unmanned aircraft system

by

Deepak Gautam

School of Technology, Environments and Design

Submitted in fulfilment of the requirements for the Degree of Doctor of Philosophy

University of Tasmania
February, 2019

Declaration of Originality

This thesis contains no material which has been accepted for a degree or diploma by the University or any other institution, except by way of background information and duly acknowledged in the thesis, and to the best of my knowledge and belief no material previously published or written by another person except where due acknowledgement is made in the text of the thesis, nor does the thesis contain any material that infringes copyright.

Deepak Gautam

13 February 2019

Statement of Co-Authorship

The following people and institution contributed to the publication of the research undertaken as a part of this thesis:

Deepak Gautam, School of Technology, Environments and Design, University of Tasmania
Arko Lucieer, School of Technology, Environments and Design, University of Tasmania
Zbyněk Malenovský, School of Technology, Environments and Design, University of Tasmania
Christopher Watson, School of Technology, Environments and Design, University of Tasmania
Juliane Bendig, School of Technology, Environments and Design, University of Tasmania
Colin McCoull, School of Technology, Environments and Design, University of Tasmania

All the authors in relevant chapters contributed to the idea and its development: Gautam performed the experiments, data processing, and analysis. Proportion of work undertaken by each of the co-authors for all the chapters are presented as a percentage value.

Paper 1 (Chapter 2): Gautam (85%), Lucieer (5%), Malenovský (5%), Watson (5%)

Paper 2 (Chapter 3): Gautam (85%), Watson (5%), Lucieer (5%), Malenovský (5%)

Paper 3 (Chapter 4): Gautam (85%), Lucieer (5%), Watson (5%), McCoull (5%)

Paper 4 (Chapter 5): Gautam (80%), Lucieer (5%), Bendig (5%), Malenovský (5%), Watson (5%)

We the undersigned agree with the above stated "proportion of work undertaken" for each of the above published (or submitted) peer-reviewed manuscripts contributing to this thesis:

Candidate: **Deepak Gautam** (06/08/2018)

Arko Lucieer (12/08/2018)

Christopher Watson (06/08/2018)

Zbyněk Malenovský (06/08/2018)

Juliane Bendig (08/08/2018)

Colin McCoull (08/08/2018)

Authority of Access

Deepak Gautam

13 February 2018

Abstract

Point-measuring spectroradiometers have gained interest in recent years for airborne spectroscopy from unmanned aircraft systems (UAS) facilitated by miniaturisation and improvements in signal quality. Spectroradiometers sample radiance and reflectance measurement at a very high spectral resolution, and are commonly used for laboratory measurements and outdoor proximal remote sensing. When mounted on a UAS, they offer a unique potential in quantifying vegetation properties, such as solar-induced fluorescence (SIF), in unprecedented spatial detail. To understand and to correctly interpret the spectral signal measured from the UAS, the extent and geolocation of the measurement spot, referred to as the spectral footprint becomes crucial. This thesis investigates how the footprint of a point-measuring spectroradiometer on a UAS can be determined. The focus of the thesis is on the pre-requisites for the footprint determination, specifically a) selection of position and orientation (pose) measurement sensors, b) their detailed geolocation error budget and c) geometric calibration, followed by d) the footprint determination and validation. This study is motivated by the upcoming Fluorescence Explorer (FLEX) satellite mission of the European Space Agency, equipped with a fluorescence imaging spectrometer. This study is an enabler for mapping the spatial distribution of the SIF signal in detail, which subsequently has the potential to contribute to validation of FLEX observations and an improved understanding of the fluorescence signal.

A UAS-based spectroradiometer system, equipped with inertial measurement units (IMUs), global navigation satellite system (GNSS) receivers, a monochrome camera, and an on-board computer, was designed for this study. The primary IMU/GNSS is used to measure the spectroradiometer pose, while the secondary IMU/GNSS measures the orientation of the UAS airframe. To determine the most suitable primary IMU/GNSS, two microelectromechanical systems (MEMS)-based units were tested in a series of ground-based experiments. The IMU/GNSS units were assessed in their performance accuracy, size and weight, and synchronisation capability with the spectroradiometer. Accordingly, the Spatial Dual IMU with its dual-frequency dual antenna GNSS was determined as the most suitable sensor to measure the spectroradiometer pose on a UAS.

The selected IMU/GNSS unit was used to develop an error budget model aiming to estimate the uncertainty associated with the footprint geolocation. The model propagates, through an aerial data georeferencing formula, the input uncertainties originating from a) the on-board IMU/GNSS sensors, b) the sensor calibration, and c) the digital surface

model (DSM). The model was used to investigate the effect of various spectroradiometer field of view (FOV), integration time, UAS flying speed and flying height values, as well as the grade of the IMU device on the footprint geolocation error. The orientation accuracy of the spectroradiometer, resulting from IMU and boresight angle errors, was found to be the dominant source of the footprint geolocation uncertainty.

Subsequently, the lever-arm offset and boresight angle must be properly calibrated and the spectroradiometer FOV correctly determined in order to achieve the accurate computation of the footprint. The lever-arm offsets were measured using a scaled three-dimensional point cloud representation of the UAS-spectroradiometer system. The point cloud was created from the photos of the airframe processed with the structure-from-motion (SfM) algorithm. The boresight angles were estimated from stationary experiments that computed the difference between the orientations of IMU, spectroradiometer, and camera. The footprint size of the spectroradiometer for a known distance to the target was measured experimentally, thereby enabling the FOV angle to be determined. The lever-arm and boresight correction was applied to the in-flight dataset and the correction was validated through data acquired by the co-mounted camera processed using the SfM algorithm.

The footprint geolocation was derived via a ray-casting algorithm that uses the calibrated spectrometer pose measurement together with a DSM of the observed terrain. The combined effect of spectroradiometer integration time, UAS flying speed, spectroradiometer pointing angle, and terrain slope was incorporated in the footprint calculation. Using the ray-casting algorithm, the constituent boundary points of the footprint were computed for each IMU/GNSS epoch, and these points were connected to form an instantaneous footprint. The series of instantaneous footprints collected during the integration time of the spectroradiometer were combined to form the final footprint shape. To validate the spectroradiometer footprint location, the ray-casting technique was applied to isolated pixels of the co-mounted camera. The resulting geolocation of the isolated pixels were compared with the surveyed ground control points. The footprint spectral validation was performed by comparing UAS-based and ground-measured reflectance signatures of natural targets.

The overarching goal of this thesis, to determine geolocation and extent of the spectroradiometer footprint, was achieved with a spatial accuracy of 15 cm $\pm 1\sigma$ for a flying height of 10 m. The achieved level of spatial detail and accuracy can be considered as sufficient to retrieve a SIF signal over heterogeneous vegetated surfaces. Hence, this study made significant steps towards robust UAS-based acquisition of spatially explicit SIF

measurements, which will facilitate the validation of future FLEX satellite observations. The work in this thesis has contributed to improved acquisition and understanding of the SIF signal, which will in turn improve our ability to monitor photosynthetic activity of vegetation at the global scale.

Acknowledgements

I joined the TerraLuma research group, the University of Tasmania in November 2014 to pursue PhD degree. It has been a great journey of my life and there are many people to be thankful of for their direct and indirect contributions professionally and personally towards the completion of the degree.

Firstly, I sincerely thank my supervisors Associate Professor Arko Lucieer, Dr Zbyněk Malenovský, and Dr Christopher Watson for your help, support, and guidance throughout my candidature. I consider myself very fortunate to have had a chance to pursue PhD with my supervisor Arko who has been a great source of inspiration and motivation through his exemplary work. I could not thank you enough for enabling involvement in a wide range of research projects to tailor my academic career.

Numerous individuals and groups must be thanked for their help in field data collection, processing, as well as technical support. Thanks to Dr Juliane Bendig and Dr Darren Turner, for being such an awesome mentor and source of inspiration I gained a lot from both of you. Thanks to amazing engineer Richard Ballard - I would not have achieved this much in my PhD if not for Richard's engineering and manufacturing work. Thanks to Dr Colin McCoull, Dr Steve Harwin, Iain Clarke, Rob Andreas, Matt Dell, Rhys Wyber, Sachit Rajbhandari, Bjarke Madsen, and Nicolo Camarretta for assistance at different stages of my PhD including during collection of data, processing, and use of equipment.

All the member of the TerraLuma research group and the discipline of GIS and remote sensing, thank you for helping along the way. I will cherish the regular table tennis breaks that boosted our productivity and maintained sanity.

Many thanks to my mother Renuka and father Narishowr, I appreciate your dedication and hard work that helped me progress to this point. My dear sister Laxmi and brother Dipesh, thank you for bearing with me during my busy days.

Finally, and most importantly, a big thanks to my beautiful and lovely wife Pratiksha for being so understanding during my struggles, difficult times, and especially when I was busy while you needed me the most. Your unconditional support and encouragement paved the path for me to follow my dream. Thank you my love, I look forward to the next phase of our lives together along with our daughter Dia.

Glossary of Abbreviations

3D : Three-dimensional

A1 : Front antenna of the dual antenna setup

AGL : Above ground level

ALS : Airborne Laser Scanning/Scanner

ASD : Analytical spectral devices

BRDF : Bidirectional reflectance distribution function

C/A : Coarse/acquisition

CCD : Charged-coupled device

CEP : Circular error probability

CF : Chlorophyll fluorescence

DEM : Digital elevation model

DN : Digital number

DSM: Digital surface model

ESA : European space agency

FLEX : Fluorescence explorer

FLORIS : Fluorescence imageing spectrometer

FOG : Fiberoptic gyroscope

FOV: Field of view

FWHM : Full width at half maximum

GC : Gimbal centre

GCP : Ground control point

GDA94 : Geocentric datum of Australia 1994

GNSS : Global navigation satellite system

GPS : Global positioning system

IMU_boom : IMU placed in the antenna

IMU_gimbal : IMU placed in the gimbal

IMU : Inertial measurement unit

LiDAR : Light detection and ranging

MEMS : Micro-electro-mechanical systems

MGA55 : Map grid of Australia zone 55

NDVI : Normalised difference vegetation index

NED : North east down

PRI : Photochemical reflectance index

Pose : Position and orientation

RINEX : Receiver independent exchange format

RMS : Root mean squared

RMSE : Root mean squared error

RTK : Real-time kinematic

SIF : Solar-induced chlorophyll fluorescence

SNR : Signal-to-noise ratio

SPAN : Synchronised position attitude navigation

SRP : Spectroradiometer reference point

SfM : Structure-from-motion

UAS : Unmanned aircraft system (UAS), also known as UAV, or drone.

UAV : Unmanned aerial vehicle (UAV), also known as UAS, or drone.

UTM : Universal transverse mercator

WGN : White Gaussian noise

List of Symbols

- $W = (n, e, h)$: - W represents the the geographic coordinate system. The constituent northing, easting and height axes are represented by (n, e, h).

- $G = (i_g, j_g, k_g)$: - G is the coordinate system of the Spatial Dual IMU. The constituent axes of the coordinate system are (i_g, j_g, k_g).

- $B = (i_b, j_b, k_b)$: - B is the coordinate system of the MicroStrain IMU placed in the antenna boom. The constituent axes of the coordinate system are (i_b, j_b, k_b).

- $C = (i_c, j_c, k_c)$: - C is the coordinate system of the Grasshopper camera placed in the Gimbal. The constituent axes of the coordinate system are (i_c, j_c, k_c).

- $S = (i_s, j_s, k_s)$: - S is the coordinate system of the NovAtel SPAN IMU. The constituent axes of the coordinate system are (i_s, j_s, k_s).

- $M = (i_m, j_m, k_m)$: - M is the coordinate system of the MTi-G-700 IMU. The constituent axes of the coordinate system are (i_m, j_m, k_m).

- C, S with subscript $_1$, $_2$, and $_3$: - C and S represents *cos* and *sin* function while subscript $_1$, $_2$, and $_3$ represent the *heading*, *pitch* and *roll* angles. For example, C_1 represents $cos(heading)$.

- $\mathbf{R}^S_{G/M}$: - The rotation matrix to transform from G or M coordinate frame to S coordinate frame.

- $\mathbf{R}_{G/M}$: - The attitude matrix parametrised using Euler angles of Spatial Dual or MTi-G-700 IMU

- $\mathbf{R}^{Rotated}_{G/M}$: - Attitude matrix after applying $\mathbf{R}^S_{G/M}$ rotation to the attitude matrix $\mathbf{R}_{G/M}$.

- $\mathbf{R}^{Mean}_{Static}$: - Attitude matrix containing a mean of orientation difference between the $\mathbf{R}^{Rotated}_{G/M}$ and S coordinate frame

- $\mathbf{R}^{Corrected}_{G/M}$: - Attitude matrix parametrised with the Euler angle of Spatial Dual or MTi-G-700 after applying rotation and correcting the mounting misalignment

- $(\sigma_{n^W}, \sigma_{e^W}, \sigma_{h^W})$: - The uncertainty in position measurement represented in W coordinate system

- $(\sigma_{r^B}, \sigma_{p^B}, \sigma_{h^B})$: - The white gaussian noise uncertainty in roll, pitch and heading of the IMU_boom

- $(\sigma_{r_b^B}, \sigma_{p_b^B}, \sigma_{h_b^B})$: - The uncertainty in boresight angle estimates between the IMU_boom and the dual antenna

- $(\sigma_{r_d^B}, \sigma_{p_d^B}, \sigma_{h_d^B})$: - Drifting bias uncertainty of the IMU_boom

- $(\sigma_{r_t^B}, \sigma_{p_t^B}, \sigma_{h_t^B})$: - The turn-on to turn-on bias uncertainty of the IMU_boom

- $(\sigma_{r^G}, \sigma_{p^G}, \sigma_{h^G})$: - The white gaussian noise uncertainty in roll, pitch and heading of the IMU_gimbal

- $(\sigma_{r_b^G}, \sigma_{p_b^G}, \sigma_{h_b^G})$: - The uncertainty in boresight angle estimates between the IMU_gimbal and the spectroradiometer

- $(\sigma_{r_d^G}, \sigma_{p_d^G}, \sigma_{h_d^G})$: - Drifting bias uncertainty of the IMU_gimbal

- $(\sigma_{r_t^G}, \sigma_{p_t^G}, \sigma_{h_t^G})$: - The turn-on to turn-on bias uncertainty of the IMU_gimbal

- $(\sigma_{L1_i^G}, \sigma_{L1_j^G}, \sigma_{L1_k^G})$: - Lever-arm offset uncertainty between the front antenna and gimbal centre

- $(\sigma_{L2_i^G}, \sigma_{L2_j^G}, \sigma_{L2_{kG}})$: - Lever-arm offset uncertainty between the gimbal centre and the spectroradiometer reference point

- $(\sigma_{v_i^G}, \sigma_{v_j^G}, \sigma_{v_k^G})$: - The uncertainty in determination of offset from spectroradiometer reference point to the nadir location on ground

- $b_d(t)$: - Value of the drifting bias at an epoch t

- s : - Autocorrelation factor between consecutive measurements

- $w(t)$: - Zero-mean white gaussian noise representing drifting bias with variance σ_{bd}^2

- (ϕ, θ, ψ) : - IMU roll, pitch, and heading angle

- FP^W : - The geolocation of the spectroradiometer footprint
- $A1^W$: - The position of the front antenna
- $\mathbf{R}_B^W$: - The attitude matrix of the MicroStrain IMU placed on the antenna boom
- $\mathbf{R}_G^W$: - The attitude matrix of the Spatial Dual IMU placed in the gimbal
- $\mathbf{R}_b^B$: - The boresight misalignment between the IMU_boom and the antenna system
- $\mathbf{R}_b^G$: - The boresight misalignment between the IMU_gimbal and the spectroradiometer Gershun tube
- $\mathbf{R}_d^B$: - The rotation matrix parametrised with the temporal drift component of the IMU_boom
- $\mathbf{R}_d^G$: - The rotation matrix parametrised with the temporal drift component of the IMU_gimbal
- $\mathbf{R}_t^B$: - The rotation matrix parametrised wit turn-on to turn-on bias of the IMU_boom
- $\mathbf{R}_t^G$: - The rotation matrix parametrised wit turn-on to turn-on bias of the IMU_gimbal
- $L1^G$: - The lever-arm offset from front antenna to the gimbal centre.
- $L2^G$: - The lever-arm offset from gimbal centre to the spectroradiometer reference point.
- v^G : - Vector representation of the offset vector from the spectroradiometer reference point to the ground at nadir
- C_{FP} : - (3×3) covariance matrix containing the variance of footprint estimation uncertainty
- J : - (3×36) Jacobian matrix containing partial differential equations of the aerial georeferencing equation
- C_{input} : - (36×36) diagonal covariance matrix containing the input variances of

each error source

- SRP^W : - The position of the spectroradiometer reference point
- $A1^W$: - The position of front antenna in W coordinate frame
- (ϕ,θ,ψ) : - The roll, pitch, and heading angle
- (x, y, h) : - The offset from the spectroradiometer reference point to the footprint location in W coordinate frame
- (x', y') : - The lateral offset from the spectroradiometer reference point to the footprint location in C coordinate frame
- R_T : - The reflectance of the target being measured
- DN_T : - The raw DN value measurement of the target being measured
- DN_O : - The raw DN value measurement of the dark current
- DN_R : - The raw DN value measurement of the white reference panel
- R_f : - The reflectance factor of the reference panel
- SRP^W : - The position of the spectroradiometer reference point
- $A1^W$: - The position of front antenna in W coordinate frame
- $\mathbf{R}^W_{Spec}$: - Orientation of the spectroradiometer
- $\hat{agl}$: - Unit vector pointing vertically down from the spectroradiometer reference point
- $\hat{iFP}$: - Unit vector which is aligned with the spectroradiometer optical axis

Table of Contents

List of Tables

List of Figures

1 | Background and introduction

1.1 Introduction

1.1.1 General motivation

Remote sensing serves as a non-invasive approach to identify and monitor biogeophysical and biogeochemical properties from the air or from space (Pajares 2015; Joseph 2005; Mulla 2013; Yang et al. 2018). Depending on observation platforms (such as satellite, airborne, or ground) and optical capabilities of sensors (such as visible, infrared, or thermal sensing), a wide range of spatial and spectral measurement scales is achievable. Swaths of satellite systems cover, in general, large areas (hundreds to thousands of square kilometres), but these images often lack a suitable spatial and spectral resolution for fine-scale observations (Belward and Skøien 2015). Field measurements, on the other hand, provide spatially and spectrally detailed observations, but cover only small areas (typically in quadrats or transects of several meters). Traditional airborne imagery is often prohibitively expensive and too coarse in spatial and spectral resolution for plant canopy level observation. Recent developments in remote sensing based on unmanned aircraft systems (UAS) have the potential to bridge the spatio-spectral scale gap between detailed field observations and relatively coarse airborne and satellite observation (Lucieer et al. 2014).

The upcoming Fluorescence Explorer (FLEX) satellite mission supported by the European Space Agency (ESA) has captured the attention of the remote sensing community, as it will for the first time measure the optical signal of photons directly produced by photosynthetic biochemical processes (Coppo et al. 2017; Moreno et al. 2016). The satellite mission will carry the fluorescence imaging spectrometer (FLORIS) sensor measuring the solar-induced chlorophyll fluorescence (SIF) of terrestrial vegetation and shallow coastal waters (Meroni et al. 2009; Rascher et al. 2015; Drusch et al. 2016; Cogliati et al. 2015a). SIF represents the amount of energy dissipated by green plants through regulated metabolic processes (Moreno et al. 2015). When interpreted together with the vegetation heat dissipation of non-photochemical protection, SIF can provide a direct indication of plant photosynthetic efficiency and actual plant stress (Ač et al. 2015; Panigada et al. 2014). The FLEX satellite is expected to monitor photosynthetic rates, which will reveal the extent of gross primary productivity at a global scale (Wieneke et al. 2016; Damm et al. 2015; Frankenberg et al. 2011; Porcar-Castell et al. 2014). With the impending launch of the satellite mission in 2022, UAS-mounted SIF solutions are

emerging to bridge the scale gap as well as contribute to interpretation and validation of satellite observations.

A non-imaging, i.e. spot measuring, spectroradiometer possess unprecedented spectral resolution and spectral sampling required for a successful SIF retrieval (Garzonio et al. 2017; Julitta et al. 2016). A UAS-based spectroradiometer offers a unique potential to investigate the influence of the spatial distribution and structural variability of vegetation on the SIF signal, for instance within a single FLEX FLORIS image pixel of 300 m $\times$ 300 m in size. To unravel the spatial contributions of the surfaces measured within a single pixel, a detailed spatial characterization of the UAS measurement spot becomes crucial. Understanding and characterising the observation location is, therefore, crucial to advance our understanding of the FLEX and other global and regional remote sensing imaging observation and to bridge the scale gap.

In addition, The UAS-based spectroradiometer with accurate knowledge of the observation location opens up a number of new opportunities. The spectral data with the accurate information of the measurement spot can be used to: 1) sample the ground reference reflectance for other airbone spectral sensor, such as a multispectral or hyperspectral, 2) understand the signals of narrow and subtle spectral features, such as SIF, and 3) upscale field-based and near proximity measurements to airborne/satellite spectroscopy observations. The spectral ground sampling is traditionally done with a handheld spectroradiometer, while GNSS coordinates and site-specific notes mark their geolocation (Thenkabail and Lyon 2016). With a UAS-mounted spectroradiometer covering a larger area, this whole process can be automated in an effective and non-invasive manner. Examples include the sampling of sensitive vegetation such as Antarctic moss (Lucieer et al. 2012; Turner et al. 2014b). The extra spectral detail of the modern field spectroradiometers opens opportunity for studying new signals, as for instance plant SIF and photoprotective xanthophyll transformation reflectance changed indicated by the photochemical reflectance index (PRI) (Malenovský et al. 2014). Accurate geolocation of the SIF and PRI measurements presents an opportunity to understand better the spatial distribution of photosynthetic efficiency, and stress level of terrestrial vegetation (Wyber et al. 2017; Verrelst et al. 2016; Pinto et al. 2016; Malenovský et al. 2009). Finally, with accurate geolocation determination, the UAS spectroradiometer technology can serve as a tool for interpreting and validating data of satellite missions such as ESA's FLEX Earth Explorer (Mohammed et al. 2016; Drusch et al. 2016).

The spectroradiometers were, due to their high weight and size, traditionally used as hand-held lab-based devices or outdoor as proximal spectral sensing instruments (e.g.

ASD FieldSpec and LabSpec spectroradiometers) (Julitta et al. 2016; Turner et al. 2014c; Liu and Cheng 2010). With recent advancement in UAS technology and miniaturisation of sensors, the spectroradiometers can be carried on-board a UAS (Burkart et al. 2014; Garzonio et al. 2017; Zeng et al. 2017). A measurement taken from a UAS, or an elevated platform (Rossini et al. 2015; Wyber 2018) or a tower (Guanter et al. 2014; Zhang et al. 2014; Lange et al. 2017), can provide data over a larger area within a shorter time span, if compared to the traditional discrete field surveys. A UAS-mounted spectroradiometer, in particular, offers spatially flexible and detailed observation at variable scale over a target. Yet, the key challenge in UAS spectroscopy is the determination of the location, extent and shape of a spectrometer footprint on the ground.

Footprint of the UAS-based spectroradiometer is in this study defined as the spatial extent of earth surface area from which radiance is received by the spectroradiometer. This footprint is complex in shape and size, given by dynamic movements of an UAS carrier, the complexity of terrain, and the integration time of spectroradiometer. Spatial location of the footprint centre, expressed in a geographic coordinate frame, is referred to as the geolocation of the footprint. The spectroradiometer footprint is guided by the field of view (FOV) of the Gershun tube, which is considered to be a circular solid angle. A circular FOV accepts radiance measurement from a geometrically circular area, which is the projection of the FOV from an above ground level (AGL) height to the ground. This study defines the instantaneous footprint as the footprint formed by the solid angle of FOV when the spectroradiometer is stationary or when the effect of sensor integration time is not considered for the spectroradiometer in motion (also known as support (Atkinson and Curran 1995; Mac Arthur et al. 2013; Mac Arthur et al. 2012)) (See Figure 1.1).

1.1.2 Challenges in the computation of the spectroradiometer footprint

For use of a spectroradiometer on a UAS at a realistic AGL flying height, the extent of the footprint is an important factor. Without a complete footprint characterisation over a local topography, it is difficult to deduce if the spectral measurement is originated purely from a single target (such as a vegetation canopy) or if it represents mixed spectra of more than one radiance source (e.g. vegetation with bare soil and concrete) (Khodadadzadeh et al. 2014). Thus, to make a correct and informed geospatial interpretation of the UAS spectral data, the footprint geolocation, shape, and size determination is crucial. Important factors required to accurately compute the footprint and its geometry are: a) spectroradiometer position and orientation, b) ground and canopy surface model of the test site, c) calibration of lever-arm and boresight of the on-board sensors,

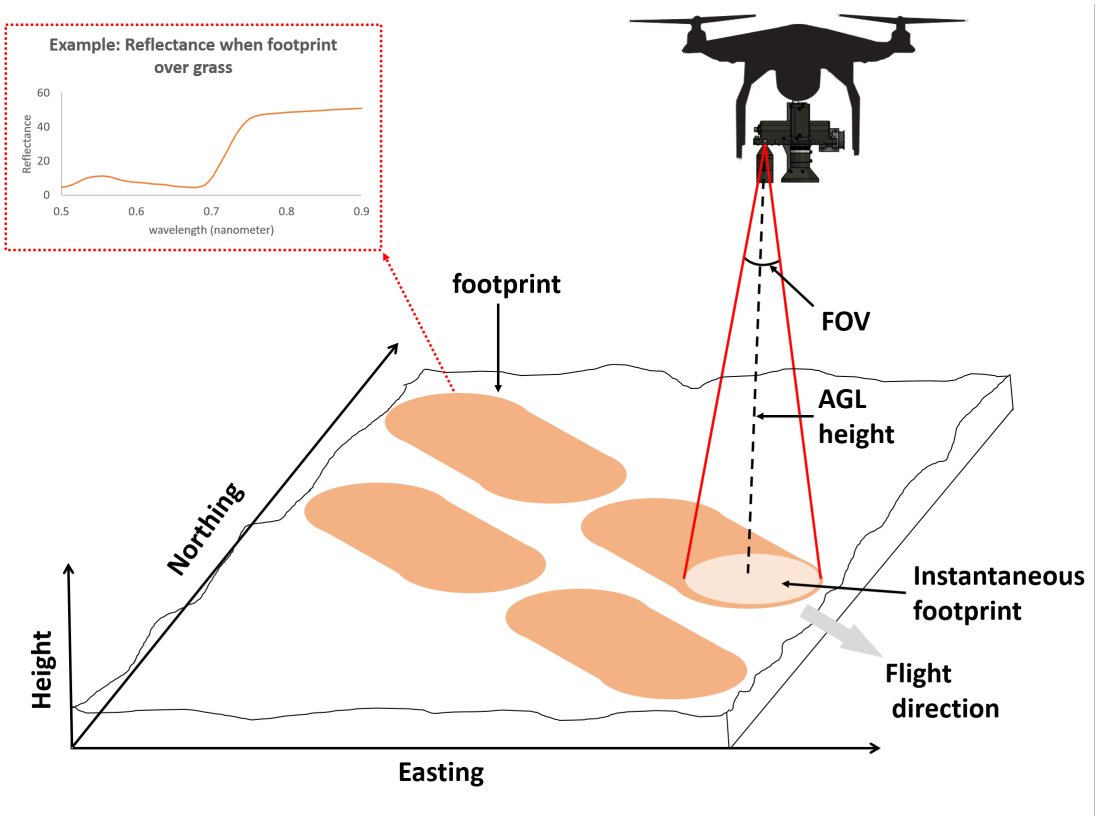

Figure 1.1: The footprint of a spectroradiometer mounted on a UAS. Note the spectroradiometer acquires ultra-high resolution spectral data, however, lacks spatially defining features.

d) spectroradiometer operational parameters (integration time and FOV), and e) UAS operational parameters (flying height and speed).

Position and orientation of the UAS sensor are required for computation of the spectroradiometer footprint. Position can be measured using a global navigation satellite system (GNSS) receiver and the orientation using an inertial measurement unit (IMU). The GNSS and IMU instruments need to be selected in accordance with a) the UAS payload restrictions, b) required performance accuracy, and c) a need for simple integration with the spectroradiometer (Gautam et al. 2017). Small GNSS/IMUs have, in general, a lower performance accuracy, however, the UAS payload size and weight restrict use of high-grade GNSS/IMUs with a better pose accuracy, which are too heavy (Colomina and Molina 2014). Thus, the use of GNSS/IMU must be a compromise between the UAS payload constrains and the achievable GNSS/IMU accuracy. It is important to note that the GNSS and IMU accuracies are the primary factor dictating the achievable geolocation accuracy (Wallace et al. 2011; Schaer et al. 2007).

Despite the performance accuracy of the selected GNSS and IMU, additional uncertainty

exists due to a lever-arm offset (offset from the GNSS receiver to the spectroradiometer) and boresight angles (angular misalignment between the IMU and the spectroradiometer). As a result of the offset and misalignment, the GNSS and IMU measurements do not represent the position and orientation of the spectroradiometer (Chiang et al. 2012a; Chiang et al. 2015; Daakir et al. 2016; Williams et al. 2013). Consequently, the lever-arm offsets and boresight misalignments must be corrected. Additionally, the spectroradiometer footprint determination requires a topography model. The topography can range from a simple flat terrain, such as grass carpets over a sports field, up to a complex canopy structures, such as a bush land or forest stands. The footprint, consequently, varies depending on the slope of the terrain and the pointing angle of the spectroradiometer. For a spectroradiometer pointing vertically down (nadir direction) to a flat terrain, the footprint is of a circular shape with the size being a function of the distance from the target and the FOV. However, the footprint becomes elliptical, if the spectroradiometer is pointing at an oblique angle. A further complexity in footprint extent and shape arises with the undulating slope of the terrain and with the fact that the spectroradiometer carrier is during an acquisition in motion.

The key parameters of the UAS spectroradiometer, directly influencing characterisation of the footprint, are integration time, FOV, flying height above ground/canopy, topography model, and flying speed. Size of footprint is directly proportional to the spectroradiometer FOV, and the flying height of the UAS. The footprint gets elongated due to the combined effect of the integration time and the flying speed. If the UAS flies north to south, the footprint gets elongated in the along-track direction, while keeping circular across-track in the east-west direction. The footprint shape becomes more complex due to the flight dynamics of the UAS carrier, particularly roll and pitch angles, during the signal integration, resulting in deformations in both along-track and across-track directions.

Footprint determination of a UAS-based spectroradiometer poses unique challenges as the sensor is passive and non-imaging. Common UAS-based imaging sensors (e.g. a camera (Harwin and Lucieer 2012; Turner et al. 2014a), pushbroom spectrometer (Suomalainen et al. 2014; Turner et al. 2017; Jaud et al. 2018) or a spectral 2D imager (Aasen et al. 2018; Aasen and Bolten 2018)) utilise visual information, such as tie points between multiple images and spatial relations between multiple pixels within an image for calibration and georeferencing. The aforementioned information is not available for a spectroradiometer observation where the entire footprint is a single sampled area analogous to a single image pixel. Similarly, active sensors on a UAS such as airborne laser (LiDAR) scanners (Wallace et al. 2012; Jozkow et al. 2016) use the range measurement

from the sensor to the target, which is not known for the spectroradiometer observation either. The lack of spatially coherent and contiguous data means that no control points inside a single footprint and common tie-points between successive footprints can be identified. Similarly, lack of the distance measurement to the target limits the ability to use the direct method of sensing the topography for the footprint determination. Consequently, these spectroradiometers cannot use commonly used techniques of georeferencing available for other aerial imaging (e.g. aerial triangulation, bundle adjustment, SfM) and LiDAR sensors. The geometric calibration and footprint computation requires a new approach, which utilises external sensors such as a GNSS, IMU, RGB sensor, and topographic surface model.

1.1.3 Contribution

The main contribution of this thesis is in the development of an optimal processing framework to achieve an accurate footprint geolocation, including a) selection of suitable sensors to determine position and orientation, b) understanding achievable accuracy using the selected sensors, c) calibration of the sensors with regards to the footprint geometry, and d) determination of the footprint size and shape. In the first step, the performance accuracy of GNSS and IMU for spectroradiometer pose determination is assessed. In the second step, an aerial georeferencing error budget model is developed to determine achievable footprint geolocation accuracy. Using the error budget model, the footprint geolocation sensitivity analysis of uncertainties associated with sensors, their calibration, and general flying parameters are conducted. In the third step, the calibration pertaining to the spectroradiometer pose (correction of the lever-arm offset and the boresight angle), and footprint size (determination of the FOV angle) are performed. The calibrated spectroradiometer pose along with the topography model of the ground is then used in a ray-casting algorithm to compute the footprint of the spectroradiometer. The combined effect of spectroradiometer integration time, platform flying speed, spectroradiometer pointing angle, and terrain slope is fully incorporated in the footprint calculation. Finally, spatial validation of the footprint geolocation, spectral validation of acquired reflectance and retrieved SIF signal of natural targets are presented.

1.2 Aims and objectives

The aim of this thesis is to develop and validate a framework for accurate footprint geolocation and delineation of a spectroradiometer mounted on a UAS. To achieve the aim of this study, the following specific objectives were defined:

1.2.1 Objective1: Selection and assessment of the GNSS and IMU sensors

- To assess performance and accuracy of lightweight GNSS/IMUs for pose determination of the spectroradiometer mounted on a UAS.

- To select a suitable GNSS/IMU taking into account its accuracy, form factor, and synchronisation capabilities with the spectroradiometer.

1.2.2 Objective2: Error budget modelling and assessment of the footprint spatial uncertainty

- To develop and execute a realistic error budget model of the spectroradiometer footprint geolocation.

- To assess the geometry and uncertainty associated with the footprint geolocation considering the key factors: IMU uncertainty, GNSS uncertainty, FOV, flying speed, lever-arm offset and boresight calibration, and signal integration time.

1.2.3 Objective3: Calibration of the on-board sensors for accurate footprint geometry

- To determine and calibrate the lever-arm offset between the GNSS receiver and the spectroradiometer, as well as the boresight angle between the IMU, the camera, and the spectroradiometer.

- To determine the size of the spectroradiometer footprint as a function of AGL flying height.

1.2.4 Objective4: Characterisation of the footprint geolocation and extent

- To compute footprint geolocation, shape and size of the spectroradiometer via a ray-casting algorithm.

- To incorporate the effect of UAS flying speed, the spectroradiometer integration time, terrain slope, and the spectroradiometer viewing angle on the footprint ex-

tent.

- To validate the footprint geolocation and spectral reflectance and demonstrate ability of SIF retrieval over natural targets using the UAS-based spectroradiometer.

1.3 Thesis Structure

This thesis is prepared based on peer-reviewed publication. The core chapters (Chapter 2–5) comprise of articles published in (Chapter 2, *ASCE Journal of Surveying Engineering* in Chapter 3 in *MDPI Sensors Journal*) submitted to (Chapter 4 in *ISPRS Journal of Photogrammetry and Remote Sensing*), and prepared for submission to (Chapter 5, *IEEE Transactions on Geoscience and Remote Sensing*) refereed journals. The research objectives addressed per chapter are illustrated in Figure 1.2. Each chapter presents the relevant literature, materials, methodology, results, discussion of results, and conclusions. The overall introduction is presented in the Chapter 1, while the concluding Chapter 6 reviews the outcomes in the context of the objectives, discusses the work limitations and a future outlook.

Research materials in this thesis was conducted as a part of a broader Australian Research Council Discovery Project (ARC DP 140101488) that focused on the retrieval and interpretation of chlorophyll fluorescence. This work provided an essential component for correct and informed interpretation of the UAS retrieved chlorophyll fluorescence signal.

To assert the required geolocation accuracy, the three GNSS and IMU sensors are assessed and compared in Chapter 2. Ground-based experimental data obtained in 2015 was used to investigate the pose accuracy of two MEMS-based IMUs. Based on the performance accuracy, form factor, and ease of synchronisation, Spatial Dual GNSS/IMU was determined as the most suitable sensor.

The selected Spatial Dual GNSS/IMU and other external sensors were used to investigate the resulting footprint geolocation spatial uncertainty in Chapter 3. This chapter focuses on the error budget of the footprint geolocation, where the main investigated sources of geolocation uncertainties were: i) the sensor height AGL, ii) the sensor orientation measured by the IMU, iii) the sensor position determined by the GNSS, iv) calibration of lever-arm offsets and boresight angles, and iv) errors in digital surface model (DSM) of the topography. Errors originating from aforementioned sources were propagated through an aerial data georeferencing model, taking into account a range of FOV and

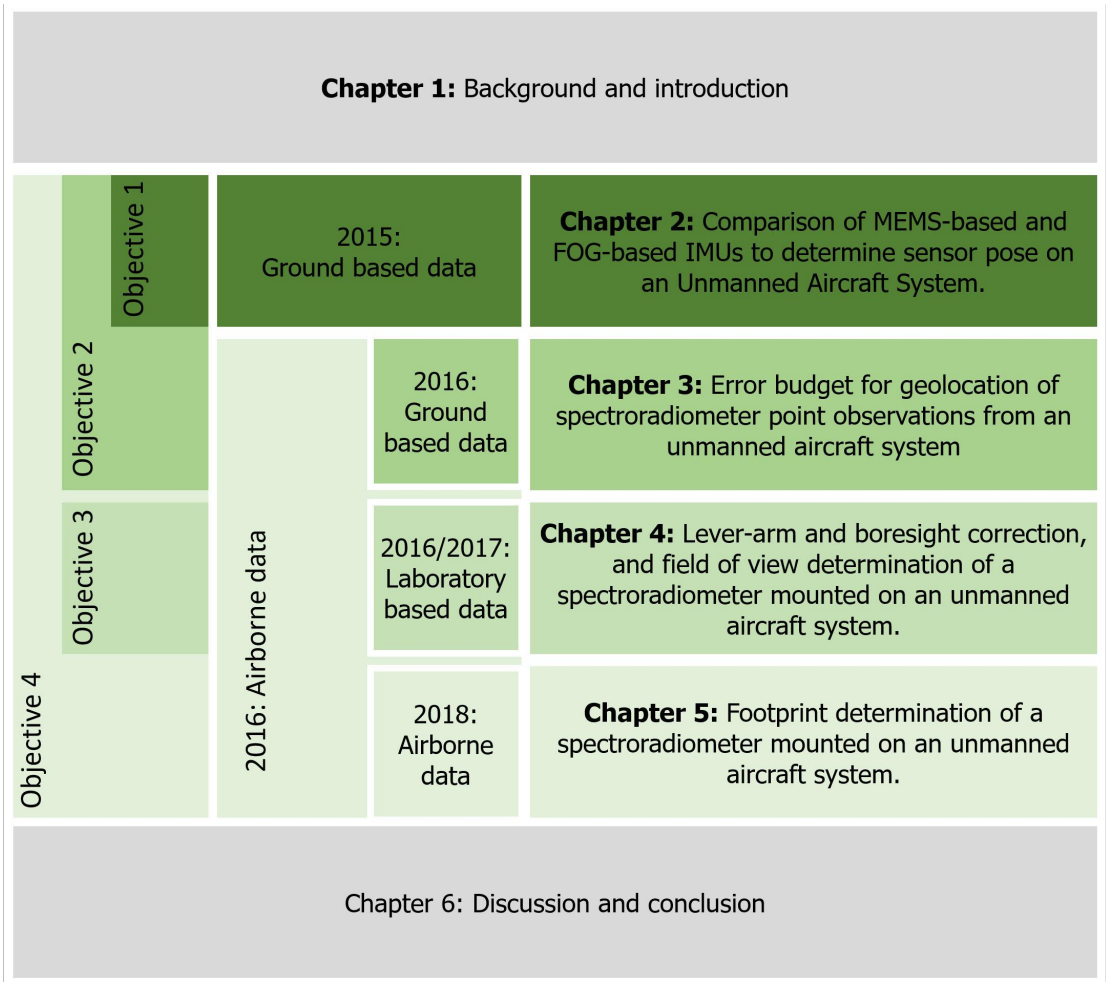

Figure 1.2: Structure of thesis, research objectives, experiments, and chapters

AGL height values, IMU grade, spectrometer integration time, and UAS flight speed. The input error sources were modelled and estimated using ground data (static and dynamic) from experiments performed in 2016. As a result, a detailed assessment of error sources and their contributions is provided and an expected footprint size to uncertainty ratio for a range of IMU grade, FOV and AGL height values is listed, which enables matching the ratio with an appropriate spatial scale.

In Chapter 4 the calibration of the lever-arm offsets and boresight angles necessary for a high accuracy footprint determination was carried out. The calibration was performed based on the laboratory and outdoor experiments were conducted in 2016 and 2017. The lever-arm offset was determined from a scaled 3D point cloud of the UAS, created using a photogrammetric technique. The boresight angles were estimated through stationary experiments computing differences between the absolute orientations of the individual sensors. Additionally, the FOV of the spectroradiometer was computed by estimating the footprint size for a known AGL height. This enabled footprint size to be computed

as a function of distance to the target. Inflight lever-arm offset and boresight angle calibration was verified with the camera pose derived from the structure from motion (SfM) algorithm as the reference.

Building upon the three previous chapters, Chapter 5 is devoted to estimation of the footprint (geolocation, shape, and size) of the UAS-mounted non-imaging spectroradiometer using airborne data acquired in 2018. The footprint location of the spectroradiometer was derived by a ray-casting algorithm combining the calibrated pose data with a DSM. The footprint size was defined as a function of distance to the target and the FOV of the spectroradiometer. The shape resulted from spectroradiometer integration time, UAS flight speed, the slope and exposition of terrain, and pointing angles of the spectroradiometer. Computed footprint geolocation was validated using the photographs from a co-mounted camera as the reference. The UAS acquired spectral reflectance was compared with ground-based measurement reflectance signatures of natural targets.

The final Chapter 6 addresses the overall aim of the thesis and provides answers to individual objectives. Overarching limitations of the study are discussed in depth, followed by the concluding remarks and suggestions of a future research direction.

2 | Comparison of MEMS-based and FOG-based IMUs to determine sensor pose on an Unmanned Aircraft System

Chapter 2 focuses on the comparison of different state-of-the-art position and orientation determination sensors with a small form factor suitable to fly on a small-sized UAS. The aim of this comparison is to enable position and orientation determination of a spectroradiometer mounted on an unmanned aircraft system. The work comprising this chapter is published in *Journal of Surveying Engineering, American Society of Civil Engineers* (Gautam et al. 2017) and presented at *The 9th International Symposium on Mobile Mapping Technology.*

Abstract

Small-sized Unmanned Aircraft Systems (UAS) are restricted to use only a light weight Micro-Electro-Mechanical Systems (MEMS) based Inertial Measurement Units (IMU) due to their limited payload capacity. Still, some UAS-based geospatial remote sensing applications, such as airborne spectroscopy or laser scanning, require high accuracy pose (position and orientation) determination of the on-board sensor payload. This study presents ground-based experiments investigating the pose accuracy of two MEMS-based IMUs: the single antenna Xsens MTi-G-700 and the dual antenna dual-frequency Advanced Navigation Spatial Dual IMU/Global Navigation Satellite System (GNSS). A tightly coupled and post-processed pose solution from a Fibre Optic Gyroscope (FOG) based NovAtel SPAN IMU served as a reference to evaluate the performance of the two IMUs under investigation. Results revealed a better position solution for the Spatial Dual, while the MTi-G-700 achieved a better roll/pitch accuracy. Most importantly, the heading solution from the dual antenna configuration of the Spatial Dual, was found to be more stable than the heading obtained with the reference SPAN IMU.

2.1 Introduction

A global navigation satellite system (GNSS) receiver computes the position using observed range measurements transmitted from space borne modules of the Global Positioning System (GPS), GLONASS, Galileo (not fully operational yet), and BeiDou to provide global positional coverage. GPS applications have been growing exponentially since the release of the GPS signal for public use in 1983. Now, after just over three decades, GNSS has become an essential part of our daily activities by adopting wide and varied application fields of telecommunication, robotics, mapping, remote sensing, surveying, environmental monitoring, precision agriculture and much more (Zhang and Kovacs 2012; Zecha et al. 2013; Colomina and Molina 2014; Pajares 2015). Many errors that influence GNSS positioning can be mitigated via a differencing approach with data obtained from other receivers in the vicinity, either in real-time (commonly referred to a real-time kinematic or RTK) or post-processed. Post-processing of GNSS carrier phase observations relative to data from a base station increases the positional solution accuracy substantially (2-5 cm accuracy readily achievable on a dynamic platform).

An inertial measurement unit (IMU) computes sensor orientation by combining raw data obtained from accelerometers (acceleration), gyroscopes (angular rates), and sometimes a magnetometer (magnetic flux density) (Woodman 2007). Marine, navigational, and tactical IMUs are among the highest grade IMUs providing, for an extended period of time, very accurate orientation estimates (in the order of 0.1 degree or better). Industrial, automotive and consumer-rated IMUs are, on the other hand, lower grade IMUs with a lower cost balanced out by a lower absolute accuracy (ranging from a sub-degree to several degrees) (Schwarz and El-Sheimy 2004; Kennedy et al. 2005; Petovello et al. 2007; Kennedy and Rossi 2008). Although Micro-Electro-Mechanical Systems (MEMS) technology has witnessed advancement in the overall performance of IMUs over the last two decades, sensor noise and drift are still an important concern of MEMS IMUs for application requiring a high accuracy in sensor orientation. Moreover, MEMS IMUs require more time for self-initialisation or self-alignment, especially when computing absolute heading. Any MEMS gyroscope normally requires a long period of averaging in order to obtain a desirable level of heading accuracy (El-Osery et al. 2013). Even when provided with user manual prescribed time for self-alignment, the absolute heading tends to incur more error as compared to roll and pitch due to the weak magnetic field of the Earth, which is also easily interfered by electromagnetic noise. This could be further confounded by magnetic field interference, when operating near magnetic poles (e.g. in Antarctica), or by a high vibration and rapid deviation in flight course of an Unmanned Aircraft Systems (UAS) platform. Dual antenna GNSS systems available

on market provide a promising technique for quick and robust initialisation of absolute heading. Instead of depending on the magnetic field, it utilises the relative position of two GNSS antennae to compute the heading. This reduces the heading initialisation time and makes the absolute heading system robust, reliable, fast and easy to deploy.

Recent improvements and miniaturisation of low-cost MEMS-based IMUs and lightweight GNSS receivers have led to proliferation in UAS technology. The UAS community has exploited the lightweight MEMS IMU and GNSS to fuse the observed data either in loosely/tightly coupled configuration on a small-sized UAS platform for navigational purposes or combined with imaging sensors for the purpose of image georeferencing. Regardless of lower accuracy, small-sized UAS, due to their limited payload capacity, are restricted to MEMS IMUs. A higher level of accuracy in orientation measurement can be obtained with a Fibre Optics Gyroscope (FOG) IMU, which is usually too heavy for a small-sized UAS. Some UAS-based geospatial applications, however, require very high accuracies in pose determination of the mounted sensor. For instance an airborne LiDAR (Wallace et al. 2012; Middleton et al. 2013; Ahokas et al. 2014), pushbroom spectrometer (Lucieer et al. 2014; Suomalainen et al. 2014), or a point-measuring spectrometer (Burkart et al. 2014; Bueren et al. 2015) payloads require an accurate pose of the sensor reference point in order to determine the sensor footprint and to georeference the acquired data. The main motivation of this study is the need for accurate pose determination of a point-based spectroradiometer on-board a UAS designed to measure plant chlorophyll fluorescence (CF) emissions to accurately georeference the CF signal at the moment of acquisition. Any error in orientation determination of the sensor during spectral reading gets amplified with the measuring distance and results in higher uncertainty in the geo-location of the sensor footprint (see Figure 2.1). Precise sensor pose measurement is, therefore, of a high importance.

Prompted by the Fluorescence Explorer (FLEX) satellite mission, proposed in 2005 and approved in November 2015 by the European Space Agency (ESA) as its 8^{th} Earth Explorer, research on remote measurement of CF has greatly intensified and resulted in many technological improvements e.g. (Maier 2002; Zarco-Tejada et al. 2003; Zarco-Tejada et al. 2009; Meroni et al. 2009; Zarco-Tejada et al. 2013a; Rossini et al. 2015). Consequently, monitoring of plant photosynthetic activity and primary productivity using quantitative remote sensing and CF became one of the major interests of the vegetation remote sensing community (Malenovský et al. 2009). Although some canopy structural and photosynthetic parameters, such as leaf area index or leaf chlorophyll content, are well established remote sensing products, CF retrieval techniques from vegetation reflectance (Wu et al. 2008; Malenovský et al. 2013) are still under development

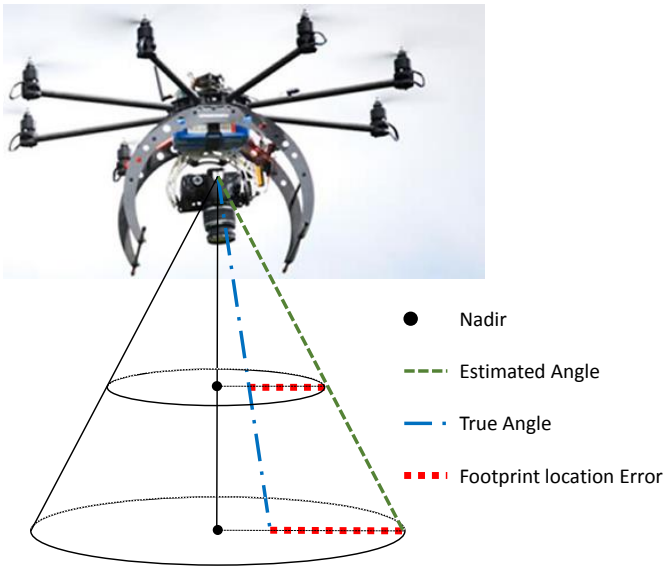

Figure 2.1: The amplifying effect of flight altitude and orientation error on identifying geo-location of a sensor footprint.

(Cogliati et al. 2015b). CF, however, has been shown to be directly linked to photosynthetic activity of plants (Meroni et al. 2009; Zarco-Tejada et al. 2013a; Tol et al. 2009; Rossini et al. 2015; Houborg et al. 2015) and their stress impact (Ač et al. 2015; Zarco-Tejada et al. 2009). In a recent experiment with photosynthetic rates of a grass carpet modulated by a herbicide, (Rossini et al. 2015) used an airborne experimental spectrometer HyPlant (Specim Inc., Oulu, Finland) to demonstrate that CF spectral peaks can be accurately mapped from an aerial platform and that CF can be causally linked to the actual vegetation photosynthetic efficiency.

Despite these advances, detailed spectral responses of plants from a lightweight UAS equipped with a non-imaging point-measuring spectrometer were studied only recently. (Burkart et al. 2014) proposed a novel UAS with a lightweight high-resolution Ocean Optics STS micro-spectrometer, which was used by (Bueren et al. 2015) to measure CF. The advancement of UAS sensor platforms (Pajares 2015), CF sensor technology, (Fernandez-Jaramillo et al. 2012; Rossini et al. 2015; Burkart et al. 2014) and CF retrieval methods (Meroni et al. 2009) together with advances in georeferencing techniques (Turner et al. 2012a; Harwin and Lucieer 2012) suggest that precise geocoding of lightweight UAS spectroscopy data is a timely topic.

The aim of this study is to identify a suitable GNSS/IMU unit for pose measurement of a UAS-mounted non-imaging spectroradiometer. Two MEMS- based GNSS/IMUs, the Advanced Navigation Spatial Dual and Xsens MTi-G-700, are assessed in terms of pose accuracy of a reference point. A tightly coupled and post-processed pose solution

from the FOG-based IMU, the NovAtel SPAN, is taken as the reference to evaluate pose performance of the two MEMS-based IMUs under investigation. In addition to the pose accuracy assessment of two MEMS-based IMUs, this paper discusses the merit of dual antenna GNSS for heading accuracy and discuss advantage of post-processing the data with reference to a GNSS base station.

2.2 Sensors

GNSS/IMU brings together two complementary systems for positioning and navigation. The inertial navigation system is very accurate over short periods and it has a high update rate whereas the GNSS is stable over a longer period of time, but it has low update rate. GNSS/IMU combines the best aspects of both the GNSS and IMU and provides a navigation solution that is more accurate and reliable. (Vali and Shorthill 1976) first proposed the FOG concept, which works on the principle that light travels at a constant speed within a given medium in an inertial frame and used the Sagnac effect to compute the angular rate. When two beams of light are sent in opposite direction on a long closed loop coil of optical fibre, the rotation of the IMU introduces a path delay for the beams to complete the same loop. The path delay leads to a phase shift of the two paths, which is measured through interferometry. This differential phase shift is used to compute the angular rate. A FOG-based IMU does not have moving parts and unlike MEMS-based IMUs, it does not rely on an inertial resistance to movement. This way it reduces a shock effect and, lowers vibration sensitivity, temperature sensitivity, random walk, and other biases including drifts. FOG are, therefore, a reliable alternative to mechanical gyroscopes to deliver precise angular rate information and are typically used for industrial and tactical-grade applications. MEMS gyroscopes, on the other hand, are based on a vibrating object that tends to continue to vibrate in the same plane. They are constructed from quartz or silicon, which makes them low in cost, small in size and low in weight. These factors have led to extensive use of MEMS-based IMUs in consumer-grade applications. Weaknesses of MEMS gyros and inertial systems lie in critical performance parameters, such as higher angle random walk/noise and, higher bias instability, which degrades the performance in stabilisation and positioning systems. Thermal sensitivity of MEMS gyros and inertial systems also impacts their bias and scale factor performance.

NovAtel's SPAN (Synchronised Position Attitude Navigation) is a tactical grade IMU equipped with FOG and MEMS-based accelerometers. It has 3 accelerometers, 3 gyroscopes and a NovAtel OEM6 GNSS receiver. This GNSS/IMU system consists of a SPAN and dual frequency GNSS antenna (Antcom G5Ant-53A4T1). The SPAN weighs

2280 g and provides very precise positioning and orientation measurements. The FOG-based IMU technology helps SPAN to achieve a roll/pitch accuracy of 0.02 degree root mean squared error (RMSE) and yaw accuracy of 0.08 degree RMSE (Kennedy et al. 2006). The single antenna SPAN utilises course over ground and inertial heading computed by its internal navigation filter as the source of precise heading. The Advanced Navigation Spatial Dual is a MEMS-based GNSS/IMU solution, which comes with a dual frequency/dual antenna (Antcom G5Ant-53A4T1) GNSS device. Weighing 285 g, it holds promising specifications with roll/pitch accuracy of 0.15 degree, heading accuracy of 0.1 degree, positional accuracy of 8 mm in horizontal plane and 15 mm on the vertical axis. The Spatial Dual utilises contemporaneous observations from two GNSS antennae and platform velocity to compute precise heading. Finally, the Xsens MTi-G-700 is a very popular lightweight MEMS-based GNSS/IMU solution suitable for small-sized UAS for its low weight of just 68 g and acceptable specifications. Its specifications suggest a roll/pitch accuracy of 0.3 degree, yaw accuracy of 1 degree, 2.5 m circular error probability (CEP) accuracy in horizontal plane and 5 m CEP accuracy on the vertical axis. It primarily relies on a magnetometer to provide the heading information. Technical details about SPAN, Spatial Dual and MTi-G-700 specifications are listed in Table 2.1.

Table 2.1: Specification of GNSS/IMUs under investigation.

	SPAN-CPT	Spatial Dual	MTi-G-700
Maker	NovAtel Inc.	Advanced Navigation	Xsens
Weight [g]	2280	285	58
Dimension [mm]	152×168×89	90×127×131	57×42×24
Gyroscope type	Fibre-Optic	MEMS	MEMS
Accelerometer type	MEMS	MEMS	MEMS
Grade	Tactical	Industrial	Industrial
Roll/Pitch Accuracy	0.02^0 RMS	0.15^0 RMS	0.3^0 RMS
Heading Accuracy	0.05^0 RMS	0.1^0 RMS	1^0 RMS (Yaw)
GNSS Update Rate	20 Hz	20 Hz	4 Hz
Horizontal Accuracy	2 cm RMS	0.8 cm RMS	2.0 m CEP
Vertical Accuracy	3 cm RMS	1.5 cm RMS	5.0 m CEP
GPS	L1/L2	L1/L2/L5	L1 C/A
GLONASS	L1/L2	L1/L2	N/A
Gallileo	N/A	E1/E2	N/A
BeiDou	N/A	B1/B2	N/A

Basic experimentation with the IMUs under investigation revealed that the FOG of SPAN had approximately 40 times lower noise in the measured angular rate as compared to the MEMS gyroscope. This evidently is the key behind the high performance characteristics of the SPAN. Moreover, the SPAN has been used in previous studies as a reference to assess the performance of lower grade GNSS/IMUs, to assess carrier phase positioning accuracy, and to demonstrate the efficiency of low cost MEMS GNSS/IMU

system (Li et al. 2008; Pinchin et al. 2008; Li et al. 2012).The specifications of the SPAN, the low noise levels, and findings from previous studies provide the justification for using the SPAN as the reference IMU/GNSS to assess the performance of Spatial Dual and MTi-G-700 IMUs (Kennedy et al. 2005).

2.3 Experimental Setup

2.3.1 The Coordinate System

Multiple coordinate reference frames are involved in our experimental setup and thus a careful transformation is required to express the pose in a single coordinate system and in a single reference point for accuracy assessment. Let $W = (n, e, h)$ be the North, East, Down (NED) coordinate system to measure the position of primary antenna (A1). Suppose $S = (i_s, j_s, k_s)$, $G = (i_g, j_g, k_g)$, and $M = (i_m, j_m, k_m)$ are the body fixed coordinate frame of SPAN, Spatial Dual, and MTi-G-700, respectively, with origin at their individual sensor's reference point. The mounting alignment of coordinate frames S, G, M and the antennae are as shown in Figure 2.2. Let the primary antenna A1 and secondary antenna (A2) be mounted at the front and rear end of j_s axis. The platform is hard-mounted on a long four-wheeled trolley ensuring that the direction of forward motion is aligned with the j_s axis. This configuration of mounting GNSS and IMU assures the best performance criterion of SPAN and Spatial Dual as prescribed in their user manuals. For instance SPAN requires the antenna to be mounted in j_s axis, which is pointed to direction of motion. Spatial Dual requires A1 to be mounted on the i_g axis which needs to be pointed to the direction of motion, and requires A2 to be at least 0.5 m behind A1 along the i_g axis. This experiment adopts the S coordinate frame and transforms the roll, pitch and heading of the Spatial Dual and the MTi-G-700 to the SPAN frame. Correspondingly, it adopts the Northing, Easting and ellipsoidal height of the NED coordinate system as per the Geocentric Datum of Australia 1994 (GDA94) reference datum and, Universal Transverse Mercator (UTM) mapping grid zone 55 to represent the position of antenna A1, commonly referred to as MGA55 (Map Grid of Australia zone 55).

2.3.2 The Sensor Platform

The sensor platform was constructed from custom-built aluminium plates, 12 connecting rods, one long carbon fibre rod, and two antenna mounts. Figure 3.1 shows the testing platform with mounted IMUs, antennae and on-board computer (Intel NUC i5). The aim of the sensor platform was to align the sensor body axes S, G, and M as per the coordinate system depicted in Figure 2.2, ensuring that all sensors are hard-mounted

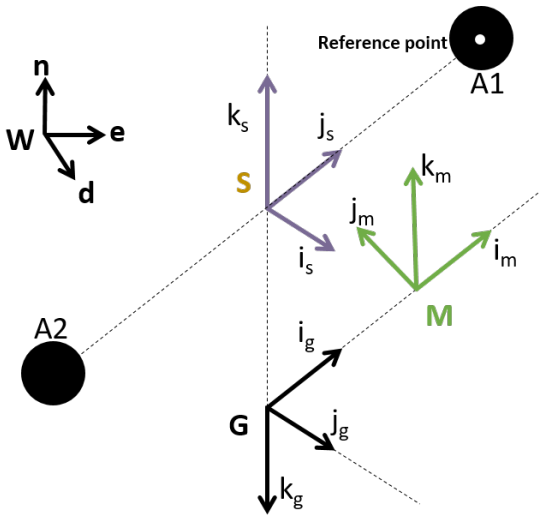

Figure 2.2: Sensor mounting configuration and coordinate system used in this study.

and no relative motion exists between the sensors at any time. The SPAN was mounted on the upper compartment of the platform, while the Spatial Dual and MTi-G-700 were mounted on the lower compartment along with the Intel NUC computer. Antenna A1 and A2 were mounted on the front end and the rear end of the platform such that j_s and i_g were pointing to the antenna A1 and that antenna A2 was 1.1 m behind the antenna A1 along the j_s axis. The observed signal from antenna A1 was shared between Spatial Dual and SPAN, whereas antenna A2 was used by the Spatial Dual alone to resolve the absolute heading. The physical offset between the antenna and IMU reference point was used to solve the lever arm effect. The on-board Intel NUC computer ran the native software of the IMUs (NovAtel Connect, Spatial Dual Manager, and Xsens MT Manager), configured the sensors and logged the on-board data.

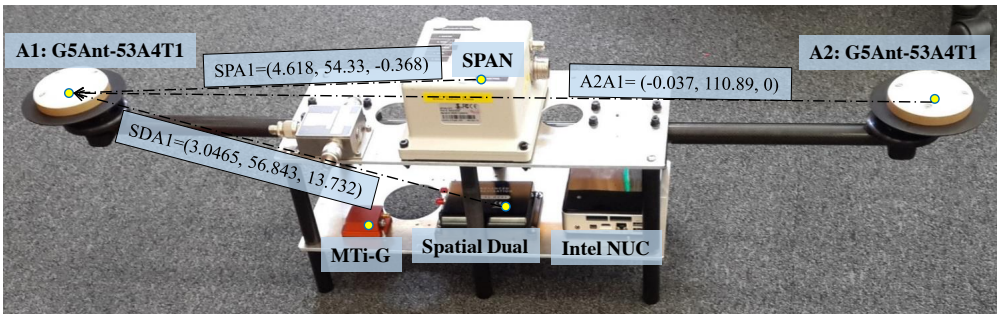

Figure 2.3: Sensors and on-board computer hard-mounted on a custom built platform.

2.3.3 The Experiment

The study was conducted in seven sets of independent experiments performed on a long four-wheeled trolley at the University of Tasmania oval sport field, Sandy bay, Australia on 22^{nd} of May and, 12^{th} and 13^{th} of July 2015. One out of the seven sets was a static

test taking 45 minutes, while the remaining six sets had static and kinematic stages as listed in Table 2.2. The base station, a Trimble GNSS Receiver (NetR9) and a Trimble Ti-Choke Ring GNSS Antenna (TRM59900), was setup at Geodetic Survey point $SS17$ (MGA55 Northing: 526787.9395, Easting: 5249942.8418, Ellipsoidal Height: 10.8898). Two stationary GPS positions were surveyed at 100 m distance apart using an RTK GNSS solution. A 100 m long measuring tape was laid out on the test field marking a straight line connection between two surveyed poles (Figure 2.4).

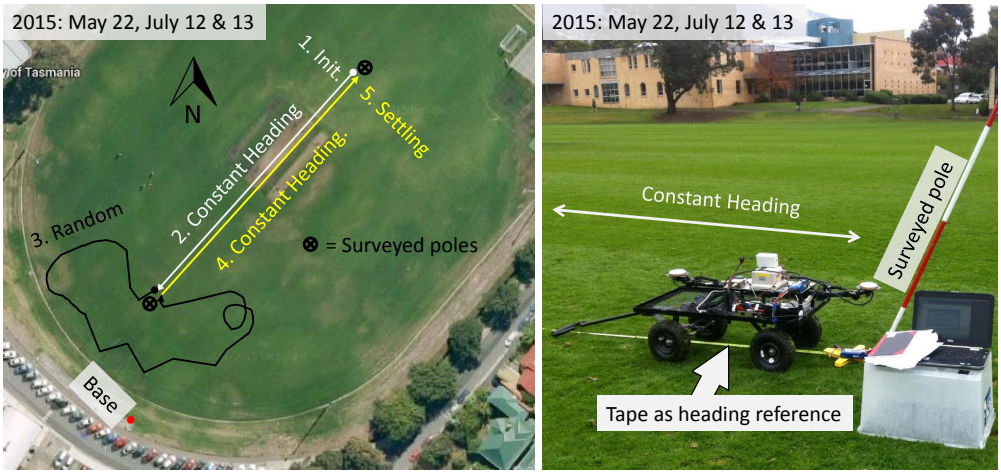

Figure 2.4: The experimental setup at the University of Tasmania oval sport field, (Sandy bay, Tasmania, Australia).

Six out of seven experiments consisted of five distinctive stages, aiming to facilitate GNSS/IMU initialisation, heading initialisation, and pose observation at a broader spectrum of measuring angles (see Figure 2.4). The initialisation and settling stages were used to stabilise the system in both forward and reverse solution of the observation and to assess the static performance of the GNSS/IMUs. During the entire initialisation and settling stage, the platform on the long four-wheeled trolley was placed stationary and aligned with the reference line connecting the position of the two surveyed poles. The constant heading walk stage was introduced right after the initialisation and before the settling stage in order to further facilitate the heading alignment and to compare the kinematic performance. This phase comprised of moving the four-wheeled trolley along the straight line connecting the two poles. The aim of the following random motion phase was to assess kinematic performance and observe pose performance at a broader range of the measuring angles, which was introduced by moving the trolley at varying speed in random directions, walking it along a gutter line around the oval field (see Figure 2.4) and climbing up and down the slope on the other side of the gutter line.

Table 2.2: Different stages of conducted experiments.

Stages	Duration	Aim	State
Initialisation	5-10 Min	Pose initialisation	S
Const. heading	2-4 Min	Heading alignment	K
Random	5-10 Min	Variation in pose	K
Const. heading	2-4 Min	Heading alignment	K
Settling	5-10 Min	Pose initialisation	S
$*$ S represents static and K represents kinematic stage			

2.4 Methodology

The GNSS data was acquired at 5 Hz by all the GNSS/IMU devices and the TRM59900 base station. Code and carrier phase observations from GPS and GLONASS were recorded by SPAN, Spatial Dual, and the base station for post processing, while MTi-G-700 used its internal filter to compute position solution based on GPS L1 C/A code observations (navigation solution) only. The orientation data was observed at a high frequency of 100 Hz, i.e. every 10 milliseconds. Figure 2.5 shows an overall workflow of this experimental setup. All configuration and data logging was performed on an on-board Intel NUC computer accessed from a control PC via virtual network. Two 4S LiPo batteries (5000 mAh capacity) and a power regulator were used to provide a stable power supply to the SPAN, Spatial Dual and Intel NUC, whereas the MTi-G-700 was powered via a USB port on the Intel NUC computer.

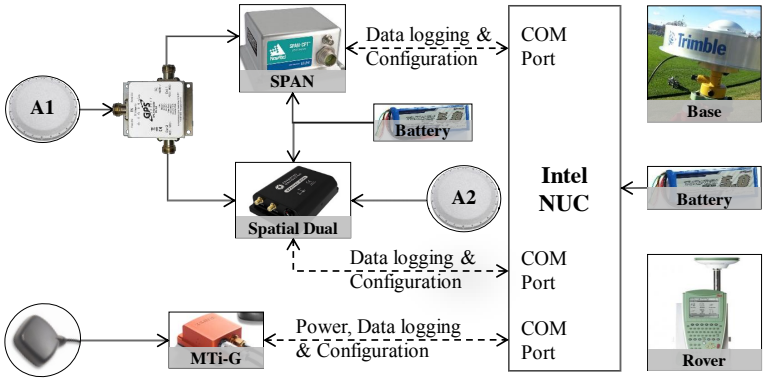

Figure 2.5: Workflow of the experimental setup.

The SPAN, Spatial Dual and MTi-G-700 used independent GPS/GNSS receivers that allowed independent synchronisation to GPS time. The timestamp of SPAN was in GPS time; Spatial Dual utilised UNIX system time in seconds, whereas the MTi-G-700 measures pose relative to UTC. Comparison of the Spatial Dual and MTi-G-700 timestamps with the SPAN timestamp revealed 1~2 milliseconds of time difference from nominal 100 HZ data sampling about an integral second. Thus, in order to synchronise

the exact moment of measuring pose to the milliseconds level of accuracy on all three devices, the pose data from Spatial Dual and MTi-G-700 had to be interpolated to the exact timestamp of SPAN (see Figure 2.6).

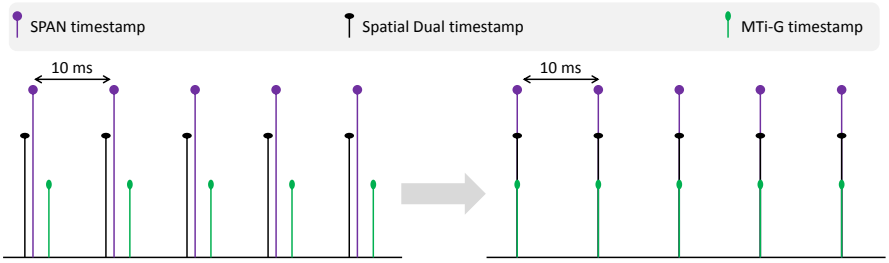

Figure 2.6: Linear interpolation (synchronisation) of the Spatial Dual and MTi-G-700 with SPAN timestamps.

The GNSS/IMU under investigation measured the position of A1 in latitude, longitude and height in reference to the WGS84 datum. The position was converted to MGA55 coordinate system. The IMUs measured orientation of their individual reference point at their respective body coordinate system. The orientation measurements of Spatial Dual and MTi-G-700 were thus rotated to correspond with the orientation frame of the SPAN using Equations 2.1 and 2.2 (Berner et al. 2008; Diebel 2006; Gautam and Ha 2013).

$$\mathbf{R}_{G/M}^{S} = \begin{bmatrix} C_1C_2 & C_1S_2S_3 - S_1C_3 & S_1S_3 + C_1S_2C_3 \\ S_1C_2 & C_1C_3 + S_1S_2S_3 & S_1S_2C_3 - C_1S_3 \\ -S_2 & C_2S_3 & C_2C_3 \end{bmatrix} \tag{2.1}$$

$$\mathbf{R}_{G/M}^{Rotated} = \mathbf{R}_{G/M}^{S}{}^{T} \times \mathbf{R}_{G/M} \tag{2.2}$$

where, $\mathbf{R}_{G/M}^{S}$ is the rotation matrix to transform from G/M frame to S frame. $\mathbf{R}_{G/M}$ is the attitude matrix parameterised using Euler angles of Spatial Dual or MTi-G-700. $\mathbf{R}_{G/M}^{Rotated}$ contains rotated Euler angles in matrix form. C and S represents *cos* and *sin* function while *heading*, *pitch* and *roll* angles are represented by subscript $_1$, $_2$, and $_3$ respectively.

A disagreement was observed in mean orientation value measured by the IMUs, during the static state of the mobile platform. This was caused by mounting misalignment between coordinate frames S, G, and M, which was corrected in the Spatial Dual and MTi-G-700 dataset based on static mean difference of the MEMS IMUs and the SPAN (see Equation 2.3). A misalignment correction in roll, pitch and heading was fed to the Spatial Dual and MTi-G-700 dataset, which eventually aligned their axes with the

axes of SPAN. This solved for sensor mounting errors, while preserving the inherent characteristics of noise, drift, and random walk of the MEMS IMUs.

$$\mathbf{R}_{G/M}^{Corrected} = \mathbf{R}_{Static}^{Mean^T} \times \mathbf{R}_{G/M}^{Rotated} \tag{2.3}$$

where, $\mathbf{R}_{Static}^{Mean}$ is the attitude matrix containing a mean of orientation difference between the rotated frame of Spatial Dual or MTi-G-700 and SPAN frame at static condition. Misalignment corrected roll, pitch and heading of the Spatial Dual and MTi-G-700 encoded in $\mathbf{R}_{G/M}^{Corrected}$ matrix can be derived using a specific set of equations (Berner et al. 2008).

2.5 The Software

We used commercial software packages provided by NovAtel Waypoint Products Group's (GrafNav 8.50 and Inertial Explorer 8.50) for post-processing the dual frequency carrier phase GNSS data and tightly coupled IMU data. The range observed by Spatial Dual and SPAN was post-processed with the data collected from a Trimble NetR9 GNSS receiver and Trimble TRM59900 choke ring GNSS antenna. The SPAN recorded the range observations and raw orientation measurement in *.GPS format, while the Spatial Dual recorded range observation in RINEX format (*.15O) and raw orientations in *.IMR format. The Trimble NetR9 used as the base station recorded the observation in RINEX format as well. Figure 2.7 shows the overall data collection and processing workflow. GrafNav resolved the carrier phase integer ambiguity using fixed static solution to reach a high level of positional accuracy (mm to cm level). Inertial Explorer software solved both position and orientation, based on the observed range and measured raw inertial data. With about 10 minutes of self-initialisation and settling period, the experiment was designed to facilitate the Inertial Explorer with static coarse and fine alignment of GNSS/IMU data, which theoretically assures the best possible solution. The software estimated pose by using two independent Kalman filters, which computed tightly-coupled pose in both forward and backward flow of time. These independent pose solutions were then combined to obtain the best result of both forward and backward solutions, by providing more weight to the solution with a lower estimation error. The combined solution was then smoothed using a Kalman smoother, which was particularly useful when GNSS slip or outages occurred.

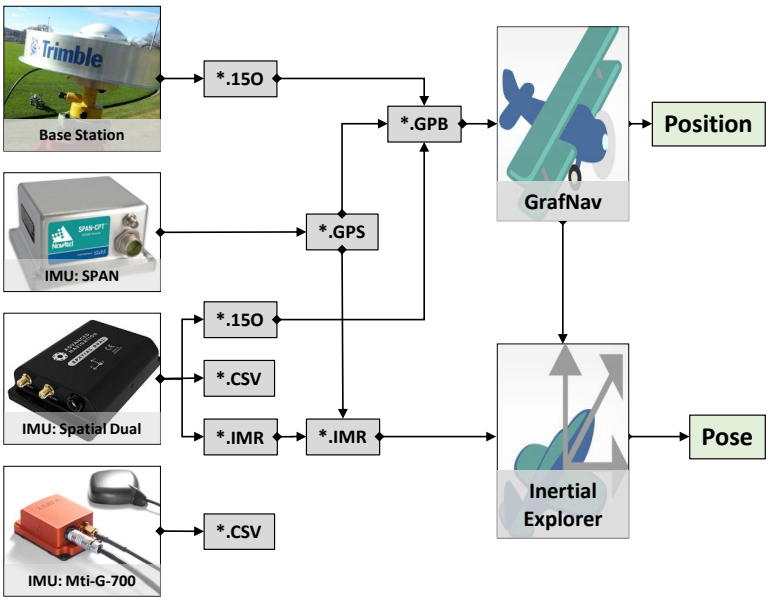

Figure 2.7: Workflow of the data collection and post-processing.

2.6 Results

The resulting position solutions of ground-based experiments are summarised in Figure 2.8. The Spatial Dual was able to achieve very precise positioning solution within 5 cm of agreement with SPAN for 95% of the sampling period. Few deviations occurred at times of satellite slip and blockage, which were especially evident for large roll and pitch angles (20~30 degree). MTi-G-700, using coarse/acquisition code of GPS L1 band, displayed poor positional solution, but commensurate with the expected accuracy of an L1(C/A) receiver.

Despite the superior technical specifications of the Spatial Dual, the experiments revealed a better agreement between MTi-G-700 and SPAN in terms of roll and pitch. Box plots in Figure 2.9 show that MTi-G-700's roll/pitch was within 0.51 degree error, whereas the Spatial Dual's orientation error was as high as 0.94 degree for 95 % of the observations.

Figure 2.10 shows that Spatial Dual provided the most stable absolute heading solution of all IMUs under investigation. Drift in the heading solution of SPAN during static condition of initial 5~10 minutes indicated the necessity of a heading reference other than SPAN. Hence, absolute heading assessment, for initialisation and settling stage (Table 2.2) , was performed in reference to the heading derived from the two surveyed GPS points as shown in Figure 2.4. The GPS points fixed at a 100 m distance ensured drift free heading reference with accuracy better than 0.05 degree on an unobstructed

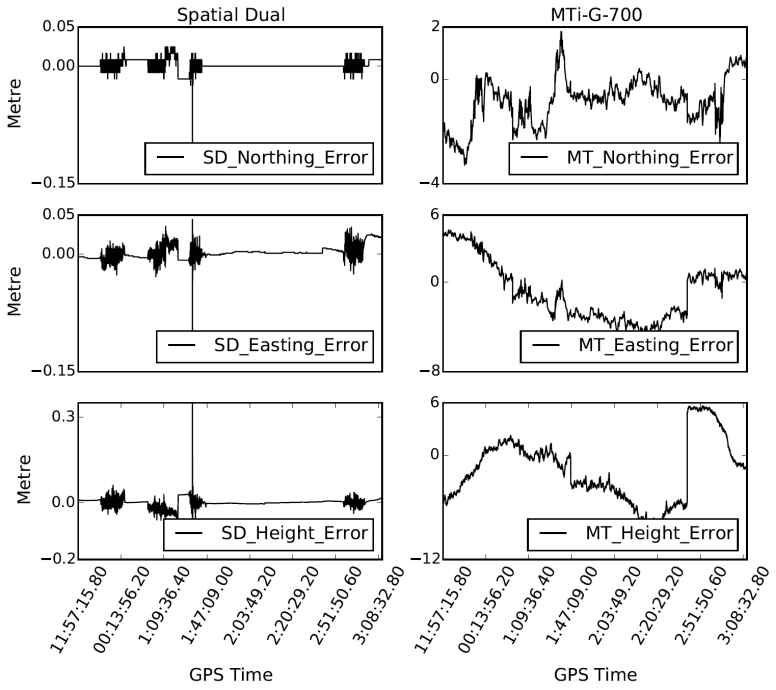

Figure 2.8: Position solutions of Spatial Dual and MTi-G-700 with respect to referencing SPAN observations.

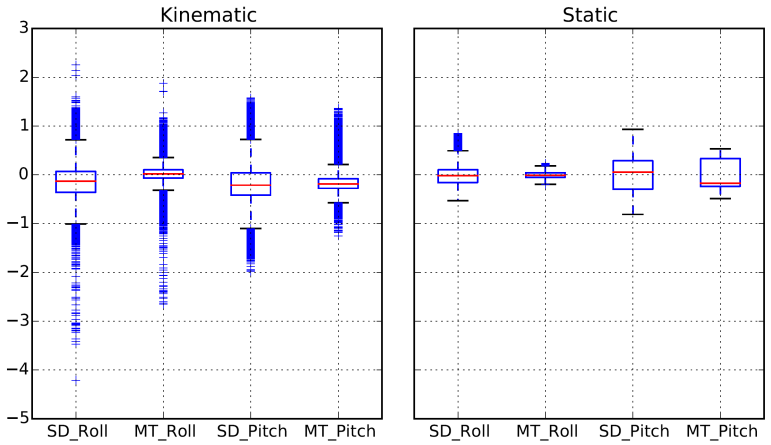

Figure 2.9: Roll/Pitch error of Spatial Dual and MTi-G-700 with respect to referencing SPAN observations.

view of GNSS signal. The dual antenna and the j_s axis were in alignment with the tape connecting the two GPS positions during the entire initialisation and settling period. Dual antenna heading solution from Spatial Dual showed a stable heading with an error within 0.60 degree as soon as an acceptable position solution was achieved. With more time provided for the heading computation, the error was further reduced to 0.12 degree for 95% of stationary epochs. Most importantly, this heading solution was even more stable and accurate than the heading measured by SPAN taking the heading derived from

two surveyed poles as reference. SPAN showed a continuous drift/correction in heading calculation during the initialisation period, which eventually stabilised to result in a heading accuracy within 1.2 degree for 95% of the epoch during settling stage. Despite its ability to track the yaw angle when the platform was in motion, MTi-G-700 suffered from a drift throughout the entire experiment. Additionally, the yaw measurement from MTi-G-700 required an external reference to compute the absolute heading.

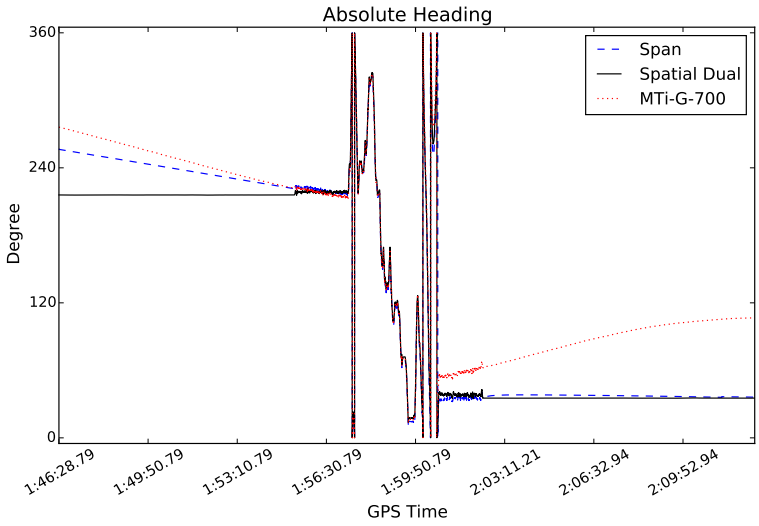

Figure 2.10: Absolute heading solution of MTi-G-700, Spatial Dual and SPAN

2.7 Discussion

Since performance of GNSS/IMU is critical for determination of a UAS-based spectrometer's footprint on the ground and for geolocation of the acquired spectral data, the aim of this experiment was to identify a suitable GNSS/IMU unit to measure accurately pose of a point-measuring spectrometer (e.g. an Ocean Optics QE Pro spectroradiometer) mounted on a small-sized UAS. Size and weight, orientation accuracy, position accuracy, and heading accuracy of the GNSS/IMU are the most important factors that need to be considered in order to determine the most suitable GNSS/IMU unit.

Both Spatial Dual and MTi-G-700 have suitable size and weight that meet the payload capacity of a small-sized UAS platform. Precise orientation measurement from MTi-G-700 is very encouraging, but its error in determining the actual position of spectrometer's reference point and hence the geo-location of the sensors footprint was too large (in the order of meters) This was further aggravated by the absolute heading error, which is critical in affine transformation of antenna position to the sensor position and ground projection of the sensor footprint. The Spatial Dual demonstrated a slightly lower performance in roll and pitch measurements, but provided promising position and

heading solutions. Although the lower roll/pitch performance increases uncertainty in geo-location of the footprint, this uncertainty increase is of a lower magnitude compared to the overall improvement in position and heading determinations. For example, when flying UAS at altitude of 20 m above ground, geo-location error of a spectrometer footprint would be more than 5 m when using MTi-G-700, while it could be limited to less than 35 cm with Spatial Dual for about 95% of observations. Additionally, the Spatial Dual allows easier as well as accurate timestamping of each observation to and from an external sensor, which is an essential functionality allowing to synchronise spectrometer spectral data with GNSS/IMU data. Hence, Spatial Dual was found to be more suitable solution for georeferencing footprint of a point-measuring spectrometer on-board a small-sized UAS. Moreover, the geo-location error in footprint could be further curbed by flying the UAS platform at lower altitudes and by combining IMU measurements with a photogrammetric approach using machine vision camera omnidirectional photographs to rectify pose of the on-board sensor (Wallace et al. 2012; Suomalainen et al. 2014).

Although this experiment performed a real-world comparison of two MEMS-based IMUs, the assessment of pose accuracy was limited to only a single reference device. This means that pose errors of the referencing SPAN unit could have contributed to some extent to the deviation in position errors observed with the other two investigated devices (e.g. Figure 2.8). Another important factor to keep in mind is need for precise quantification of misalignment on the sensor mounting axis. Although in our experiment sensors were mounted with high precision, a potential misalignment in the sensor mounting axis can impact the result. For instance, a misalignment in heading axis of the mounting sensors would cause a change in roll of SPAN to subsequently produce a change in both roll and pitch of the other IMUs. An accurate identification of mounting misalignment in UAS mounted sensor is, therefore, of a high importance.

2.8 Conclusion

Performance of two MEMS-based GNSS/IMUs, Spatial Dual and MTi-G-700, were assessed in reference to a FOG-based SPAN IMU within seven sets of ground experiments performed in three different days. We observed that the roll and pitch error of MTi-G-700 was within 0.51 degree for 95% of the observations, while Spatial Dual performed with an error of 0.94 degree. The Spatial Dual was, on the other hand, more accurate in measuring the position and absolute heading of carrier. The post-processed position solution of Spatial Dual was found to be for 95% of epochs within 5 cm of the reference solution achieved with the SPAN IMU. The dual antenna system provided a heading accuracy higher than 0.60 degree during the initialisation stage and around 0.12 degree

during the settling period. Interestingly, the absolute heading of the Spatial Dual system was found to be more stable than the heading solution obtained from the reference FOG-based SPAN IMU. The SPAN suffered from a major drift correction in heading during the initialisation stage. After a significant initialisation time, the SPAN reached a heading accuracy of about 1.12 degree. Finally, the MTi-G-700 showed continuous drift in yaw measurement during the entire experiment, which required use of an external reference to convert the observed relative yaw angle to the absolute heading. Based on these results we conclude, that the Spatial Dual unit is more suitable for the UAS sensor pose determination than the MTi-G-700 IMU unit.

2.9 Thesis Context

This Chapter provided the experimental evaluation of position and orientation measurement accuracy for small-sized sensors that are suitable for a UAS. Spatial Dual due to high accuracy in absolute heading, carrier phase accuracy in position, acceptable accuracy in roll/pitch and easy synchronisation capability was found suitable to determine position and orientation of a spectrometer on a UAS. The next chapter adopts these sensors for stochastic modelling of the footprint geolocation uncertainty.

3 | Error budget for geolocation of spectroradiometer point observations from an unmanned aircraft system

Chapter 3 uses the sensors selected in Chapter 2 to develops error budget model for the spectroradiometer mounted on a UAS. The aim of this study of error budget is to identify the parameters crucial for accurate georeferencing. The work comprising this chapter is published in *MDPI Sensors Journal* (Gautam et al. 2018) on 15 October 2018.

Abstract

We investigate footprint geolocation uncertainties of a spectroradiometer mounted on an unmanned aircraft system (UAS). Two microelectromechanical systems-based inertial measurement units (IMUs) and global navigation satellite system (GNSS) receivers were used to determine the footprint location and extent of the spectroradiometer. Errors originating from the on-board GNSS/IMU sensors were propagated through an aerial data georeferencing model, taking into account a range of values for the spectroradiometer field of view (FOV), integration time, UAS flight speed, above ground level (AGL) flying height, and IMU grade. The spectroradiometer under nominal operating conditions (8° FOV, 10 m AGL height, 0.6 s integration time, and 3 m/s flying speed) resulted in footprint extent of 140 cm across-track and 320 cm along-track, and a geolocation uncertainty of 11 cm. Flying height and orientation measurement accuracy had the largest influence on the geolocation uncertainty, whereas the FOV, integration time, and flying speed had the biggest impact on the size of the footprint. Furthermore, with an increase in flying height, the rate of increase in geolocation uncertainty was found highest for a low-grade IMU. To increase the footprint geolocation accuracy, we recommend reducing flying height while increasing the FOV which compensates the footprint area loss and increases the signal strength. Disadvantage of a lower flying height and a larger FOV is a higher sensitivity of the footprint size to changing distance from the target. To assist in matching the footprint size to uncertainty ratio with an appropriate spatial scale, we list the expected ratio for a range of IMU grades, FOVs and AGL heights.

3.1 Introduction

Airborne and space-borne spectroscopy have proven to be powerful techniques for vegetation status monitoring through estimation of biophysical and biochemical variables (Pajares 2015; Wieneke et al. 2016; Lucieer et al. 2014; Mulla 2013; Zarco-Tejada et al. 2013b) . Burkart *et al.* (Burkart et al. 2014) demonstrated the use of a small spot-measuring spectroradiometer mounted on a unmanned aircraft system (UAS) offering new potential across numerous applications including upscaling, calibration and validation of airborne and satellite sensors (e.g. airborne sensor HyPlant and/or the FLORIS sensor on-board of a future ESA FLEX mission (Moreno et al. 2016; Rascher et al. 2015; Drusch et al. 2016)), and near-range retrieval of photosynthetic chlorophyll fluorescence emissions (Wyber et al. 2017; Pinto et al. 2016; Verrelst et al. 2016; Rossini et al. 2015). To fully exploit this technology on a UAS platform (Garzonio et al. 2017; Zeng et al. 2017; Burkart et al. 2014; Burkart et al. 2015), accurate geolocation of the spectroradiometer measurements is required. This study aims to propagate the input uncertainties originated from position and orientation sensors to analyse the footprint geolocation accuracy of spectroradiometer observations as a function of the sensor field of view (FOV), above ground level (AGL) height, grades of the inertial measurement unit (IMU), spectroradiometer integration time, and UAS flight speed.

Although propagation of input uncertainties through georeferencing models for UAS mounted active sensors, such as an airborne LiDAR (Wallace et al. 2011; Schaer et al. 2007; Lichti et al. 2005), and passive imaging cameras or scanners (Gerke and Przybilla 2016; Ruiz et al. 2013; Harwin and Lucieer 2012; Turner et al. 2017) has been extensively studied, the UAS-based non-imaging spectroradiometer requires a variation to the existing georeferencing approach. The challenge arises from technical differences in georeferencing applicable to those sensors. The georeferencing technique for an imaging sensor (e.g. a camera, hyperspectral scanner or a spectral 2D imager) is guided by the acquired image and ground control points (GCPs), especially when using the tie points between multiple images, and the spatial relations between multiple pixels of an image. This information is, however, not available in case of a non-imaging spectroradiometer observation, which integrates the signal within a predefined FOV to produce a single radiance measurement. Similarly, georeferencing of laser measurements (e.g. a LiDAR) is guided by time-stamped range measurements from the sensor to the target, which is not available for a single spot measuring spectroradiometer observation. This lack of a pixel array within a footprint, tie points between subsequent measurement samples or, distance measurements to the target makes this geolocation task unique and worthy of investigation (Aasen et al. 2018).

We focus on geometrical aspects of the spectroradiometer footprint and do not address the FOV required to achieve the user-specific signal-to-noise ratio of spectral observations. The spatial extent of earth surface area from which the reflected radiance is received is defined as the footprint. Footprint results from projection of the FOV on the earth surface for the duration of integration time. Footprint geolocation can be estimated from position and orientation of the spectroradiometer using a modified direct georeferencing technique used for aerial laser scanning (Wallace et al. 2012; Wilkinson et al. 2010; Zhang and Shen 2013; Jozkow et al. 2016). Any uncertainty in geolocation has a potential to result in radiance interpretation error for the estimated geolocation. For instance, to measure spectral signatures of spatially heterogeneous landscapes (e.g. savanna or boreal forests) requires a high accuracy in geolocation of the spectrometer footprint to identify which landscape components were included in each measurement. On the other hand, footprint geolocation of a lower accuracy can be adequate for measurements over spatially homogeneous landscapes (e.g. crop monocultures), where the footprint positional error causes less the quality of acquired spectra.

The uncertainty in the footprint geolocation arises primarily from the uncertainty associated with the position (originated from global navigation satellite system (GNSS)) and attitude (originated from IMU) of the spectroradiometer at the moment of spectral acquisition. Additionally, there is also uncertainty associated with the calibration of device geometry, including the lever-arm offset and boresight angle (further complicated if using an independently orientated gimbal system often used to maintain a near-nadir view of the spectroradiometer's foreoptics). Some of the uncertainties associated with the different components of the acquisition system are assumed stationary (i.e. white noise), whereas others exhibit a temporal correlation that is best quantified using a coloured noise model. The determination of uncertainty in the footprint geolocation, therefore, requires appropriate consideration of each source of uncertainty (magnitude and stochastic behaviour), and subsequent propagation through the georeferencing model.

In this study, we use a simulation to investigate the spatial uncertainty of the footprint geolocation of a spectroradiometer mounted on a gimbal of a UAS. We focus on the assessment of a nominal lightweight sensor deployable on-board small UAS (<15 kg). Sensor noise characteristics (stationary and time correlated) are investigated using lab-based and in-flight experiments. All identifiable uncertainties were quantified and propagated through a georeferencing model to yield the overall footprint geolocation uncertainty. Finally, to provide operational recommendations for non-imaging UAS spectroscopy, we assess the relative contributions to the overall footprint uncertainty originating from independent error sources as well as from variation in flight parame-

ters (i.e. flying height, flight speed, FOV, grade of IMU/GNSS, and spectroradiometer integration time).

3.2 Materials and methods

3.2.1 Scientific sensors and platform

A typical sensor payload for UAS spectroscopy includes a spectroradiometer, GNSS (to measure the sensor position), an IMU, and a camera. For this study, we consider a remotely controlled heavy-lift multirotor DJI Matrice 600 (Dà-Jiāng Innovations Science and Technology Co., Ltd., China) equipped with custom-built antennae boom on the airframe and sensor package in the gimbal. The sensor package in the gimbal consisted of, a spectroradiometer (Ocean Optics QE Pro, Florida, USA) with spectral sampling (FWHM 0.7 nm) within 500–850 nm wavelength, a MEMS-based IMU (Advanced Navigation Spatial Dual, Sydney, Australia) referred to here as IMU_gimbal, and a machine vision camera (FLIR Grasshopper GS3-U3-23S6M-C, British Colombia, Canada). The antennae boom carried two dual frequency GNSS antennae connected to the IMU_gimbal (with Trimble BD982 GNSS receiver), a MEMS-based IMU (LORD MicroStrain 3DM-GX3-35, Vermont, USA) referred in this paper as IMU_boom to measure the orientation of the antennae boom, and an L1/CA GNSS antenna of the IMU_boom (see Figure 3.1).

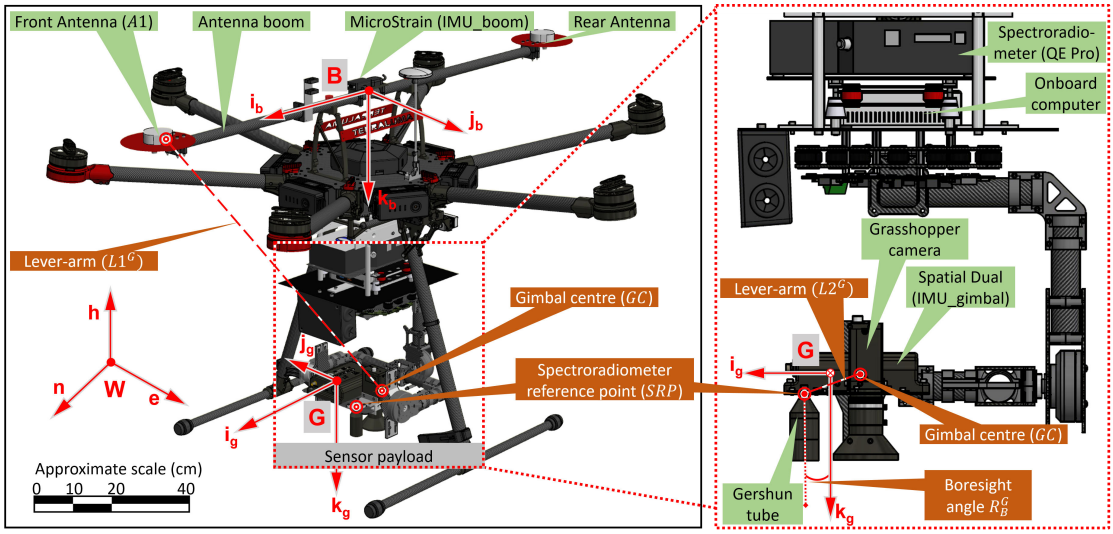

Figure 3.1: Detailed layout of the UAS spectroradiometer sensors (GNSS, IMUs, camera and spectroradiometer) mounted on a multirotor UAS.

The spectroradiometer's downward-looking fibre optic cable records radiance of a target from nadir via an FOV restrictor called a Gershun tube which is rigidly mounted close to the IMU_gimbal and camera. The gimbal attempts to dampen the effect of flight

dynamics and motor vibration on the Gershun tube. This is essential in UAS aerial spectroscopy in order to sustain a nadir pointing sensor configuration during spectral acquisitions enabling a longer signal integration time over a target.

3.2.2 Sensor geometry

The two GNSS antennae were mounted at a distance of 1.04 m (along the UAS flying direction), while the IMU_boom was positioned at the midpoint. This design was necessary to compute the lever-arm corrected position of the spectroradiometer reference point (SRP). Additionally, the antenna boom was approximately aligned with the IMU_gimbal by fixing the gimbal heading axis. The gimbal was therefore only used to attenuate the roll and pitch angle but not the heading such that the absolute heading computed using the dual antennae was a representative heading of the sensor payload (spectroradiometer, camera, IMU_boom, and IMU_gimbal). With the IMU mounted on the gimbal and the GNSS receiver mounted on the airframe, the data from the GNSS and IMU were acquired independent of each other (Li et al. 2012). This loosely-coupled configuration of the GNSS and IMU was adopted as the spectroradiometer required a stable platform (via the gimbal) for data acquisition, whereas, the GNSS antenna required a clear sky view (mounted on top of the airframe).

3.2.3 Input uncertainties

Small form-factor MEMS-based IMUs and dual frequency dual antennae GNSS employed to measure the pose of the UAS sensor payload are associated with multiple error sources such as: i) synchronisation between different sensors, ii) inherent noise in sensor measurements, and iii) uncertainties in sensor calibration. The synchronisation error is regarded as negligible, as both sensors (IMUs and spectroradiometer) are synchronised by sensor-triggered pulses (with delay negligible compared to other error sources) in accordance with GNSS timestamps.

The inherent sensor noise includes GNSS position uncertainty (related to the coordinate frame expressed in the Geocentric Datum of Australia 1994 and projected using the Universal Transverse Mercator projection, grid zone 55, epsg: 28355 (*Geoscience Australia*), $W = (n, e, h)$) and IMU orientation uncertainty (about IMU_boom and IMU_gimbal coordinate frame defined by $B = (i_b, j_b, k_b)$ and $G = (i_g, j_g, k_g)$, respectively) (Figure 3.1). IMU orientation uncertainty is divided into IMU White Gaussian noise (WGN), IMU constant bias, time correlated IMU drift, and IMU turn-on to turn-on bias (defined as the variation in the constant bias of the IMU angles for each power cycle). Similarly, the calibration error is broken down into lever-arm uncertainty (about

G coordinate frame) between the GNSS antenna and the spectroradiometer, and physical boresight uncertainty between the IMU and the spectroradiometer. The IMU constant bias and the constant physical boresight angle are, in this study, combined in a single constant boresight angle uncertainty. Similarly, the lever-arm uncertainty includes measurement uncertainties in multiple lever-arms, specifically from the front GNSS antenna (A1) to the gimbal centre (GC), and from GC to SRP (see Figure 3.1). The independent error sources used in this study to estimate the priori 3D uncertainty in footprint geolocation are outlined in Table 3.1.

Table 3.1: The input error components (originating from each sensor measurement and calibration) used for variance propagation to determine the footprint geolocation uncertainty of a UAS mounted gimballed spectroradiometer.

Sensor/Metric	Description	Symbolic representation
GNSS antenna	3 uncertainties in the position	$(\sigma_{n^W}, \sigma_{e^W}, \sigma_{h^W})$
IMU_boom	3 WGN uncertainties in orientation	$(\sigma_{r^B}, \sigma_{p^B}, \sigma_{h^B})$
	3 boresight uncertainties	$(\sigma_{r_b^B}, \sigma_{p_b^B}, \sigma_{h_b^B})$
	3 drift uncertainties in orientation	$(\sigma_{r_d^B}, \sigma_{p_d^B}, \sigma_{h_d^B})$
	3 turn-on to turn-on bias uncertainties	$(\sigma_{r_t^B}, \sigma_{p_t^B}, \sigma_{h_t^B})$
IMU_gimbal	3 WGN uncertainties in orientation	$(\sigma_{r^G}, \sigma_{p^G}, \sigma_{h^G})$
	3 boresight uncertainties	$(\sigma_{r_b^G}, \sigma_{p_b^G}, \sigma_{h_b^G})$
	3 drift uncertainties in orientation	$(\sigma_{r_d^G}, \sigma_{p_d^G}, \sigma_{h_d^G})$
	3 turn-on to turn-on bias uncertainties	$(\sigma_{r_t^G}, \sigma_{p_t^G}, \sigma_{h_t^G})$
Lever-arm	3 offset uncertainties from A1 to GC	$(\sigma_{v0_i^G}, \sigma_{v0_j^G}, \sigma_{v0_k^G})$
	3 offset uncertainties from GC to SRP	$(\sigma_{v1_i^G}, \sigma_{v1_j^G}, \sigma_{v1_{kG}})$
AGL	3 offset uncertainties from SRP to nadir	$(\sigma_{v2_i^G}, \sigma_{v2_j^G}, \sigma_{v2_k^G})$

*Note on symbolic representation: Term $\sigma_{x_y^Z}$ represents uncertainty of the term x_y in Z coordinate frame

We derived the standalone sensor measurement uncertainties and geometric calibration uncertainties based on the information provided by the sensor-specific technical specification in addition to custom experiments, and analysis of sensor data. Initially, seven sets of ground-based experiments were used to assess the achievable accuracy in position and orientation determination by comparing the IMU_gimbal with respect to a tactical-grade fibre optic gyroscope based GNSS/IMU. The MEMS-based GNSS/IMU, for a dynamic platform, was found to measure absolute position, and roll/pitch with accuracies better than 5 cm and 0.94° respectively, for 95% of epochs (Gautam et al. 2017). While the position uncertainty derived from the experiment was used in this analysis, the orientation uncertainty required a further breakdown to contributing noise components including constant bias, turn-on to turn-on bias, WGN noise, and temporal drift. Thus, further experiments and analysis were performed on the IMU data to isolate these components.

The turn-on to turn-on bias uncertainty was modelled as a random process with zero mean and a variance derived from multiple power-cycle observations. Six sets of power cycle experiments were performed each with a length of 5–10 minutes and provision of sufficient cool-down time between each data collection. The IMU was kept in a fixed position during and in between the data collection stages by hard mounting it on a custom-built tribrach adaptor on a survey tripod. For each of the 6 stationary epochs, variation in averaged IMU orientation was used to estimate the turn-on to turn-on bias uncertainty. The effect of temporal drift on turn-on to turn-on bias was assumed to be negligible due to relatively short averaging time (1–2 mins). Moreover, the WGN in the IMU is assumed to have an insignificant effect on the turn-on to turn-on bias determination due to averaging of high-frequency data (100 HZ) over the experiment duration. Turn-on to turn-on bias uncertainty by its nature is not feasible to account for as it is impractical to calibrate the IMU after each power cycle; however, the experiment was designed to quantify its magnitude.

The bias of an IMU is known to drift slowly over time. This drifting bias may be described as a stochastic process that incorporates temporal correlation (i.e. coloured noise) driven by a random component. To identify and model the drifting bias present on the IMU, static data was collected for an extended period of time (2–13 hours) at a 100 Hz frequency. During the entire experiment, the IMU was fixed on a custom-built tribrach adaptor on a survey tripod. The behaviour of the drift was assessed by performing Allan variance analysis. A first-order Markov recursive sequence was used to model the drift following Equation 3.1 (Jiang et al. 2012; Bhatt et al. 2012; Zhao et al. 2011).

$$b_d(t) = s b_d(t-1) + w(t) \tag{3.1}$$

where $b_d(t)$ is the value of the drifting bias at an epoch t, s is an autocorrelation factor and $w(t)$ is a zero-mean WGN with unknown variance σ^2_{bd}. During each iteration of the equation, the current value of the drifting bias ($b_d(t)$) is correlated with the previous value of the bias ($b_d(t-1)$) through the autocorrelation factor s and a sample from the WGN $w(t)$ is added in to simulate the random component of the drifting bias. The autocorrelation parameter of the drift model was estimated by the temporal autocorrelation of the IMU measured attitude at a lag of a single epoch. The variance of the drifting bias was computed using the scale parameter and the variance of the IMU roll, pitch and heading angles ($\sigma^2_{\phi\theta\psi}$) as presented in Equation 3.2.

$$\sigma^2_{bd} = (1 - s^2)\sigma^2_{\phi\theta\psi} \tag{3.2}$$

As defined in Equation 3.1, drifting bias is time correlated. Traditional approaches to variance and covariance propagation are built under the assumption of stationary noise characteristics with a Gaussian distribution. Here, in order to proceed with error propagation for our purpose, we use a Gaussian noise magnitude defined by the 90% exceedance probability derived from simulations of the time correlated noise. The 90% exceedance was found to be higher (about 0.45°) in flying conditions as compared to the ground based or stationary case (about 0.25°) and were subsequently adopted for this study. To achieve this, the lab-based experiments contributed in defining the temporal drift parameters used to reconstruct the IMU temporal drift. The temporal drift parameters were then scaled to closely match the in-flight condition before determining the 90% exceedance temporal drift.

Similarly, the WGN noise present in the IMU was isolated by performing a moving average over the observed IMU orientation. This uncertainty was determined based on a static ground-based experiment and flight experiments. The WGN noise extracted from the IMU data in the static ground-based experiment also had a lower level of noise as compared to the flight experiment. The IMU WGN during flight was extracted by taking the orientation of the co-mounted camera (derived from bundle adjustment) as a reference.

The AGL height determination requires a digital surface model (DSM) of the study site, in addition to the spectroradiometer position The DSM can be derived from a series of overlapping aerial images and surveyed GCPs. The achievable DSM accuracy depends on a number of variables including, but not limited to, the accuracy of GCPs, flying height, and spatial resolution of the image pixel. In this study, using literature as a guide (Uysal et al. 2015; Ruiz et al. 2013; Harwin and Lucieer 2012; Harwin et al. 2015), we assume the DSM uncertainty to be about twice larger than the uncertainty associated with a typical real-time kinematic GNSS surveying of the GCPs. Summing in quadrature, the uncertainty in the spectroradiometer position and DSM creation yields the total uncertainty in AGL height determination.

Additionally, there exists uncertainties associated with the sensor geometric calibration (lever-arm and boresight). The GNSS antenna was mounted at an offset to the SRP which created a lever-arm effect in measuring the position of the SRP. Similarly, the hard mounted IMU_gimbal and the spectroradiometer foreoptics have angular misalignment in their mounting axes creating a boresight angle. Thus, *in situ* measurements were required to determine the lever-arm offset and boresight angle. The boresight angle was estimated using a set of indoor controlled experiments by identifying and surveying

the independent pointing angles of the hard-mounted sensors. To determine the lever-arm offset, measurement was required between the points SRP, A1, and GC. These points were, however, located inside the sensor housing body which made a mechanical measurement of the offsets impractical. Furthermore, before the measurement of the offset, any misalignment between the gimbal payload and the antenna boom needed to be resolved. Thus, we used a structure-from-motion (SfM) method which allowed both the estimation of the points (SRP, GC, and A1) as well as rotation to correct for misalignment, which collectively enabled a higher accuracy in offset measurement. For this, a 3D pointcloud of the UAS platform was generated using the photos of the airframe processed with SfM algorithm (McCoull 2016). Surveyed control points were used to scale the 3D pointcloud. The offsets were measured within the scaled 3D pointcloud, after estimating the reference points and applying rotations, using AutoCAD software (Autodesk AutoCAD 2016) (*Autodesk AutoCAD*). The surveying accuracy of the indoor experiments was used to estimate the uncertainty associated with the determination of the lever-arm offset and boresight angles.

IMU error modelling

The IMU_gimbal was assessed and modelled to estimate the drifting bias and WGN uncertainties associated with it (Figure 3.2). The static data of the IMU_gimbal (Figure 3.2a) constituted of WGN and drifting bias (Figure 3.2b), which were isolated by performing a moving average. The isolated WGN component of the noise had a Gaussian distribution (Figure 3.2c). Allan deviation analysis was performed on the isolated drifting bias for a range of averaging time. With the increase in averaging time, the effect of slow moving drift was seen to be more prevalent as marked by the rise in the Allan deviation (Figure 3.2d). The isolated drifting bias and WGN noise components were used to simulate the stationary IMU data, referred to hereon as reconstructed IMU data. The close match of the reconstructed IMU data with the actual data collected by the IMU provided verification of the IMU error estimates (Figure 3.2a).

The isolated standalone IMU uncertainties along with GNSS uncertainties, calibration and measurement uncertainties are summarised in Table 2.1. The calibration uncertainties (boresight and lever-arm) in Table 2.1 are estimated from a custom indoor calibration experiment.

3.2.4 Error propagation

The effect of error sources listed in Table 3.1 on the geolocation of the spectroradiometer footprint was determined by variance propagation of the input uncertainties through the

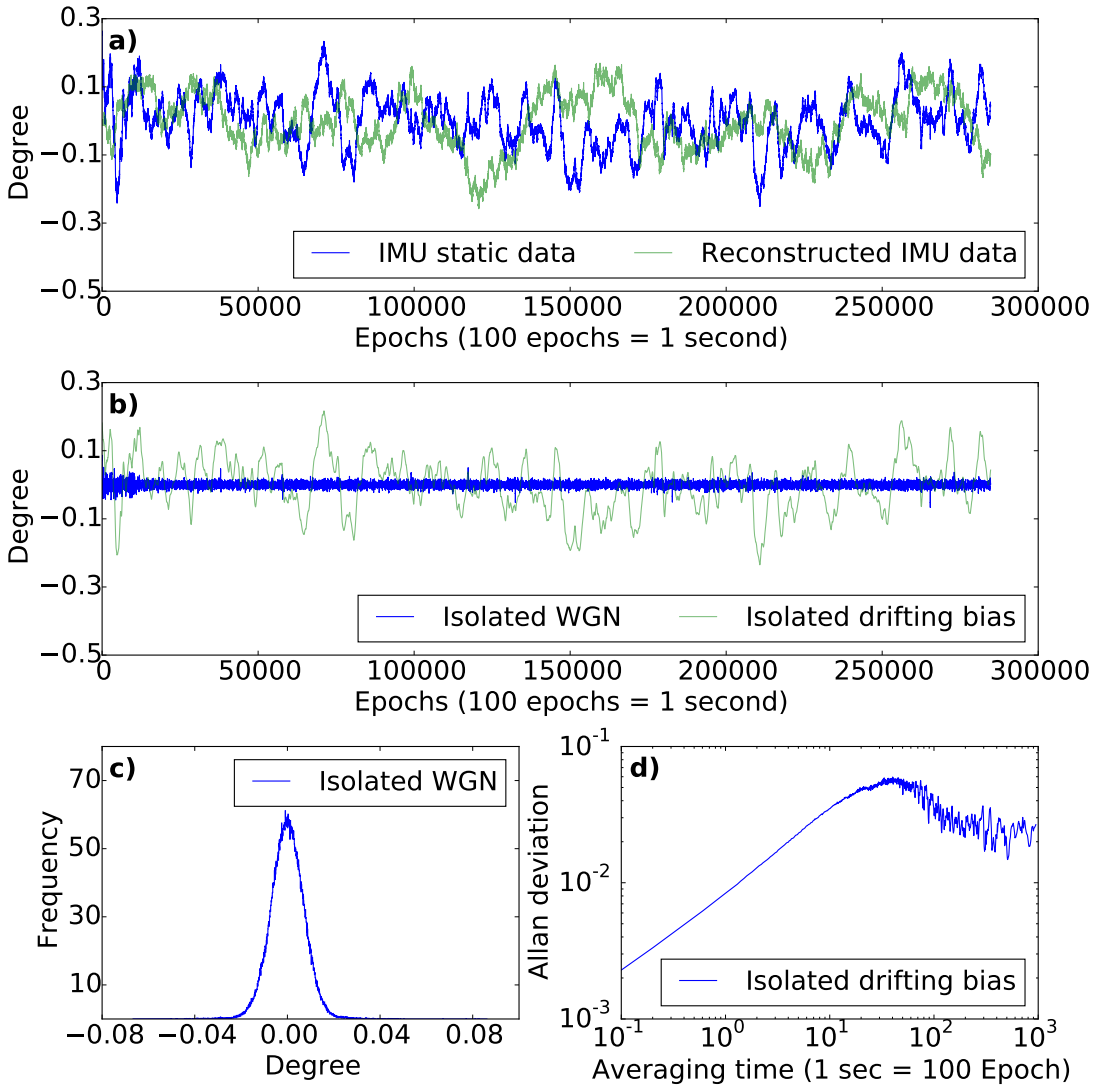

Figure 3.2: The IMU noise stochastic behaviour based on a static indoor experiment. a) The static IMU data compared to the reconstructed modelled IMU data. b) Decomposition of the static IMU data into drifting bias and WGN components. c) The Gaussian distribution of the isolated WGN component. d) The Allan deviation plot of the isolated drifting bias component.

Table 3.2: The estimated standalone uncertainties in sensor measurement and calibration.

Sensor/ Metric	Uncertainties	Nominal value ($\pm 1\sigma$) [cm or deg]	Method of Determination
GNSS antenna	$(\sigma_{n^W}, \sigma_{e^W}, \sigma_{h^W})$	(3.0, 3.0, 4.0)	Ground based experiments
IMU_boom	$(\sigma_{r^B}, \sigma_{p^B}, \sigma_{h^B})$	(0.4, 0.4, 0.9)	User manual and static data
	$(\sigma_{r_b^B}, \sigma_{p_b^B}, \sigma_{h_b^B})$	(0.2, 0.2, 0.2)	Assumed (value is not critical)
	$(\sigma_{r_d^B}, \sigma_{p_d^B}, \sigma_{h_d^B})$	(0.45, 0.45, 0.9)	Projected for flight condition.
	$(\sigma_{r_t^B}, \sigma_{p_t^B}, \sigma_{h_t^B})$	(0.10, 0.12, 0.58)	Power cycle experiments
IMU_gimbal	$(\sigma_{r^G}, \sigma_{p^G}, \sigma_{h^G})$	(0.2, 0.2, 0.1)	User manual, dynamic and static data
	$(\sigma_{r_b^G}, \sigma_{p_b^G}, \sigma_{h_b^G})$	(0.2, 0.2 0.2)	Approximated from calibration Experiments
	$(\sigma_{r_d^G}, \sigma_{p_d^G}, \sigma_{h_d^G})$	(0.25, 0.25, 0.55)	90% exceedance of reconstructed temporal drift
	$(\sigma_{r_t^G}, \sigma_{p_t^G}, \sigma_{h_t^G})$	(0.08, 0.08, 0.45)	Power cycle experiments
Lever-arm	$(\sigma_{v0_i^G}, \sigma_{v0_j^G}, \sigma_{v0_k^G})$	(0.5, 0.5, 0.5)	Measured from 3D point cloud
	$(\sigma_{v1_i^G}, \sigma_{v1_j^G}, \sigma_{v1_{kG}})$	(0.5, 0.5, 0.5)	Measured from 3D point cloud
AGL	$(\sigma_{v2_i^G}, \sigma_{v2_j^G}, \sigma_{v2_k^G})$	(5.0, 5.0, 7.0)	Approximated from σ_{hw}

direct georeferencing equation (Equation 3.3). Geolocation of spectral measurements acquired with a spectroradiometer can be achieved photogrammetrically (using a camera as an additional sensor) or via a direct georeferencing approach using GNSS/IMU to measure position and orientation of the spectroradiometer. Given the extensive post-processing required for the photogrammetric approach of georeferencing (Turner et al. 2014a), we focus here on the direct georeferencing approach. A spectroradiometer cannot measure the distance from its reference to the ground, therefore the range is derived as the height offset between the DSM to the location of the spectroradiometer (or AGL for the nadir pointing case). A modified direct georeferencing equation applicable for a UAS mounted spectroradiometer on a levelling gimbal is given by Equation 3.3 (Gabrlik et al. 2016; Wallace et al. 2012; Chiang et al. 2012b).

$$FP^W = A1^W + R_B^W R_d^B R_b^B R_t^B v0^G + R_G^W R_d^G R_t^G (v1^G + R_b^G v2^G) \tag{3.3}$$

where FP^W is the geolocation of the spectroradiometer footprint and $A1^W$ is the position of A1 both expressed in W coordinate frame. R_B^W and R_G^W are the attitude matrix as measured by the IMU_boom and IMU_gimbal (defining roll, pitch and heading from W to B and G coordinate system) respectively. The boresight misalignment between the IMU_boom and the antenna system is given by R_b^B and similarly R_b^G represents the boresight misalignment between the IMU_gimbal and the spectroradiometer. R_d^B and R_d^G represent the rotation matrix parametrised with the temporal drift component of the IMU_boom and IMU_gimbal , and R_t^B and R_t^G the respective turn-on to turn-on bias. The offset vector from A1 to the GC is given by $v0^G$. $v1^G$ represents the offset vector from the GC to the SRP, and $v2^G$ represents the offset vector from the SRP to the ground for the spectroradiometer pointing at nadir from a nominal AGL height. The input uncertainties variance and were propagated through the georeferencing equation (Equation 3.3) to compute geolocation footprint uncertainty using Equation 3.4.

$$C_{FP} = JC_{input}J^T \tag{3.4}$$

where J (3×36) is the Jacobian matrix containing partial differential equations of the functional model (Equation 3.3) with respect to each of the summarised 36 independent error sources in Table 3.1. C_{input} (36×36) is the diagonal covariance matrix containing the input variances of each error source.

3.3 Results

The shape and size of the spectroradiometer footprint were analysed for a range of FOVs, AGL heights, spectroradiometer integration times, and UAS flight speeds (Figure 3.3). The selection of FOV only influenced the size of the footprint, but had no impact on the accuracy of the footprint geolocation (Figure 3.3a). AGL height was found to be the prominent factor of both the size and geolocation uncertainty associated with the footprint (Figure 3.3a). For instance, for a constant FOV, a low flying height results in a smaller footprint and lower uncertainty compared to the footprint from a greater flying height. Thus in order to limit the uncertainty in footprint geolocation, it is optimal to fly lower and compensate the decrease in the size of the footprint by selecting a larger FOV. However, flying low requires a better ability to control the AGL distance in order to maintain a certain footprint size. In comparison, footprint size of a spectroradiometer at low AGL height is more susceptible to even smaller change in AGL distance.

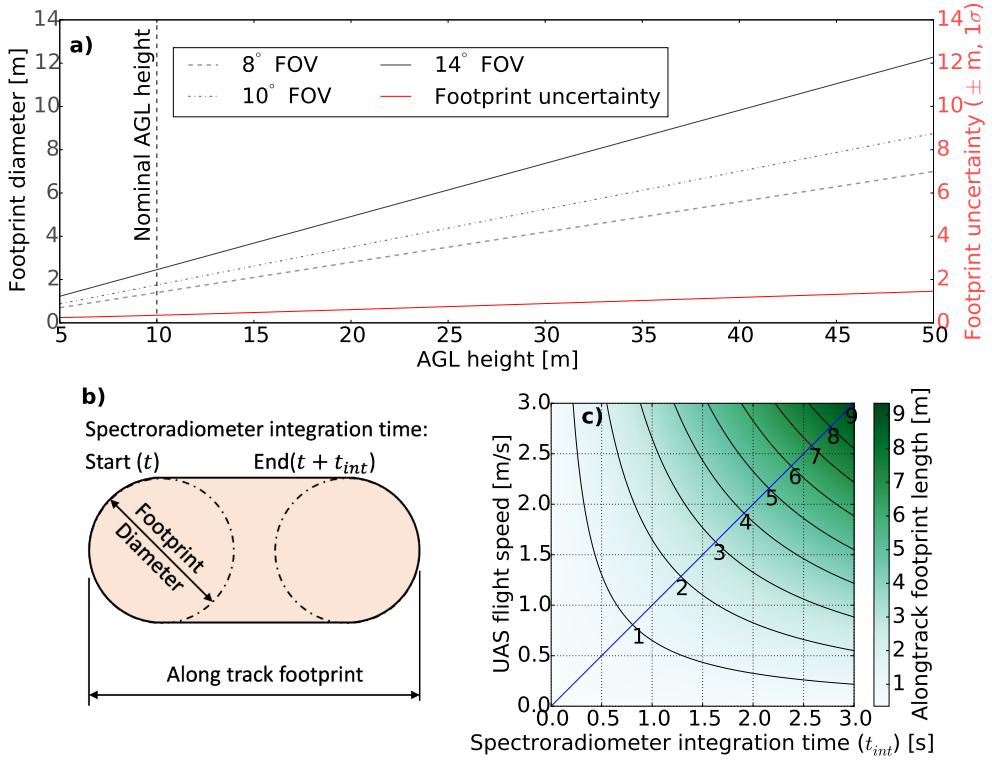

Figure 3.3: The shape and size of the UAS-mounted spectroradiometer footprint for a combination of: a) AGL height and FOV, b) spectroradiometer integration time t_{int}, and c) UAS flight speed for a nominal AGL height of 10 m and FOV of 8°.

Moreover, the combination of flight speed of the UAS and longer integration time of the spectroradiometer (typically 0.6 s to 0.9 s) results in elongation of the spectroradiometer footprint (Figure 3.3b). The diameter of the elongated circle is a function of FOV and

AGL height whereas the along-track elongation of the footprint is a function of UAS flight speed and spectroradiometer integration time (Figure 3.3c). The UAS spectroradiometer system under investigation required an integration time of 0.6 s on a clear summer day in Hobart, Australia (-42.9° S, 147.3° E). This integration time combined with a flight speed of 3 m/s at a nominal AGL height of 10 m and FOV of 8° resulted in a footprint diameter of 1.40 m and along-track footprint length of 3.20 m.

Among the listed input uncertainties in Table 2.1, the uncertainty associated with the IMU_gimbal was the second most sensitive parameter with the greatest impact on the total footprint error (Figure 3.4a). Other input uncertainties associated with the lever-arm offset, the boresight misalignment, the orientation of the IMU_boom, the AGL height, and the GNSS position had a smaller influence on the ground footprint uncertainty under the nominal condition. Furthermore, the drift present on the IMU_gimbal introduces temporally correlated uncertainty in the footprint geolocation estimation accounting for up to 5 cm additional uncertainty at a nominal AGL height (Figure 3.4b). The most likely effect of drift on footprint uncertainty (between exceedance probability 0.25 and 0.75) is presented by the non-shaded region in Figure 3.4b.

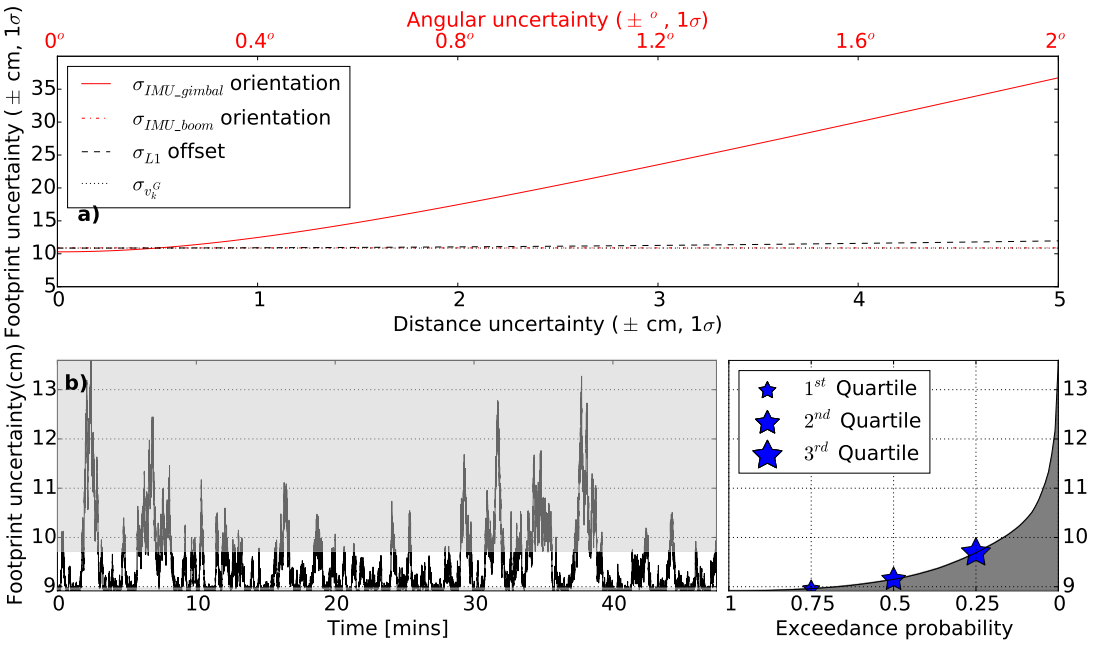

Figure 3.4: The footprint geolocation uncertainty for a range of: a) dominant input uncertainties listed in Table 3.1 and b) temporal drift. Most likely effect of the temporal drift (between exceedance probability 0.25 and 0.75) presented by the non-shaded region.

Simulations were performed to assess the implication of a higher accuracy IMU (equivalent to NovAtel's SPAN CPT IMU: see (*NovAtel SPAN-CPT*) for specification) used in the gimbal. Figure 3.5 shows a significant improvement in footprint geolocation accuracy,

which nevertheless degraded with the increase in AGL height as expected. For example, for a much lower AGL height, a medium-grade (equivalent to Spatial Dual IMU: see (*Advanced Navigation Spatial Dual*) for specification) or lower-grade IMU (equivalent to MicroStrain IMU: see (*Lord Sensing MicroStrain*) for specification) achieved an accuracy comparable to that of a high-grade IMU operating at a much greater AGL height (Figure 3.5). However, using a lower grade IMU, the footprint uncertainty is expected to increase rapidly with increase in AGL height. Moreover, with the increased flying height, the contribution of IMU_gimbal towards the overall footprint error exceeded the contribution of other sensors and measurement errors. As expected, the rate of increase in footprint uncertainty with the AGL height was found highest using a low-grade IMU and lowest using a high-grade IMU (Figure 3.5). A low-grade IMU basically limits the ability to fly at a higher altitude and/or narrow down the FOV of the spectroradiometer.

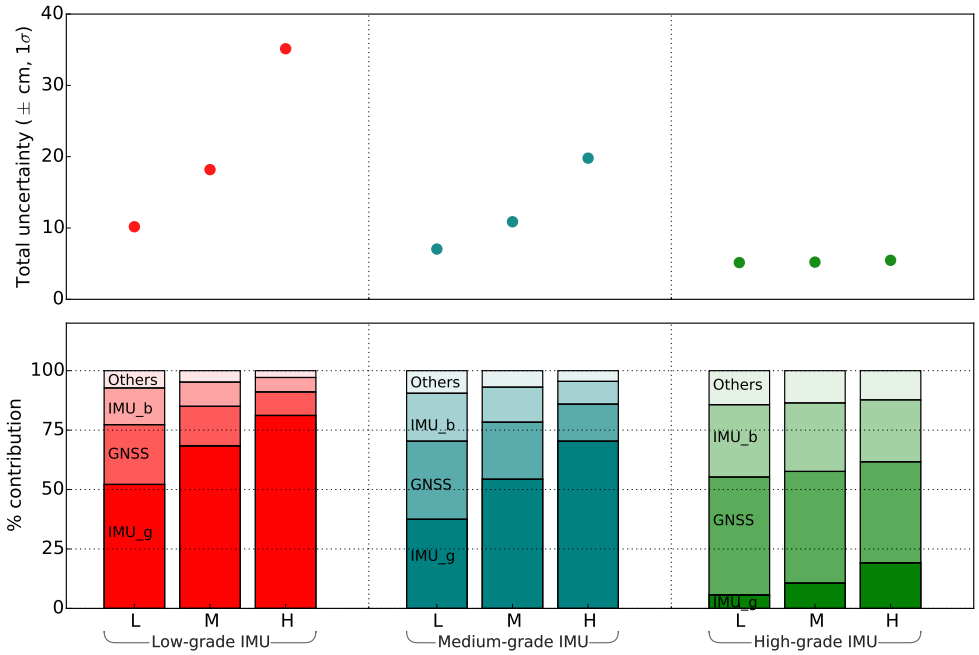

Figure 3.5: Comparative simulation of different grade IMUs (Low (equivalent to MicroStrain IMU), Nominal (equivalent to Spatial Dual IMU) and High (equivalent to a NovAtel's SPAN CPT IMU)) at different AGL flying height (L=Low (5 m), M=Nominal (10 m), H=High (20 m)) to the footprint geolocation uncertainty. *NOTE: IMU_g and IMU_b represents IMU_gimbal and IMU_boom respectively.

For the UAS platform presented here, as per specifications (Table 2.1) flying at a nominal flying height (10 m), with nominal FOV (8°) the footprint positional uncertainty was computed to be approximately 11 cm, with a footprint uncertainty to size ratio of 0.08. A lower uncertainty to size ratio (see Table 3.3) indicates a better estimate of footprint geolocation in relation to the footprint size - this is particularly important when considering any post processing to account for spectral mixing over highly heterogeneous

targets. A low-grade IMU limits our ability to reduce the FOV size without inflating the footprint to uncertainty ratio. For example, taking 0.1 as a desired ratio, a low grade IMU (at 10 m AGL height) cannot afford to utilise FOV lower than 14°, a high-grade IMU can employ all FOVs higher larger than 3° whereas a nominal grade IMU cannot go lower than 8° (Table 3.3). Incidentally, narrowing the FOV of our spectroradiometer to 8° using a Gershun tube restrictor limited the amount of energy entering the spectroradiometer and decreased the signal-to-noise ratio specifically for retrieval of solar induced chlorophyll fluorescence.

Table 3.3: The ratio of footprint diameter and footprint geolocation uncertainty using nominal grade sensors (Table 2.1) at a nominal AGL height of 10 m (and 5 m) for a range of FOV achievable using Ocean Optics Gershun tube kit.

FOV	Footprint diameter (cm)	Ratio of footprint uncertainty ($\pm 1\sigma$) to size		
		L-G IMU	M-G IMU	H-G IMU
1°	17.5 (8.7)	1.04 (1.17)	0.62 (0.81)	0.30 (0.59)
2°	34.9 (17.5)	0.52 (0.58)	0.31 (0.40)	*0.15* (0.29)
3°	52.4 (26.2)	0.35 (0.39)	0.21 (0.27)	*0.10* (0.20)
6°	104.8 (52.4)	*0.17 (0.19)*	*0.10 (0.13)*	**0.05** *(0.10)*
8°	139.9 (70.0)	*0.13 (0.15)*	**0.08** *(0.10)*	**0.04 (0.07)**
10°	175.0 (87.5)	*0.10 (0.12)*	**0.06 (0.08)**	**0.03 (0.06)**
14°	245.6 (122.8)	**0.07 (0.08)**	**0.04 (0.06)**	**0.02 (0.04)**
16°	281.1 (140.5)	**0.06 (0.07)**	**0.04 (0.05)**	**0.02 (0.04)**
20°	352.7 (176.3)	**0.05 (0.06)**	**0.03 (0.04)**	**0.01 (0.03)**
28°	498.7 (249.3)	**0.04 (0.04)**	**0.02 (0.02)**	**0.01 (0.02)**

*L-G = Low-grade, M-G = Medium-grade, H-G = High-grade

*Nominal category of footprint uncertainty to size ratio (Large, *Medium*, and **Small**)

*Numerical values in parentheses are computed for 5 m AGL height

3.4 Discussion

We investigated the accuracy of spectroradiometer footprint geolocation for a range of sensor uncertainties (Table 2.1), flying parameters (spectroradiometer integration time, FOV, AGL height, and flight speed), and IMU grades (low, medium, and high-grade IMU). Our results indicate a footprint of approximately 1.4 m wide and 3.2 m long with an associated geolocation uncertainty of approximately 11 cm based on a medium-grade IMU, integration time of 0.6 s, flying height of 10 m, FOV of 8°, flight speed of 3 m/s, and taking into account the uncertainty sources as defined in Table 2.1. The estimated geolocation uncertainty can be considered as acceptable for homogeneous ground targets.

Flying height and orientation uncertainty of the IMU_gimbal were the primary factors influencing the spectroradiometer footprint geolocation uncertainty. Compared to

medium and high-grade IMUs, the rate of increase in footprint uncertainty with the AGL height was found highest for a low-grade IMU. Our analysis under nominal flying height of 10 m and FOV of 8° suggests that it is better to maintain or reduce the flying height and simultaneously increase the FOV in order to compensate the footprint area loss and increase signal strength. However, lowering the flying height is limited by the ability of the UAS to sustain a constant flying height above the terrain. Due to the low flying height and large FOV, the size of the footprint is more sensitive to subtle changes in the height above the terrain.

Considering a fixed flying height and FOV, the IMU orientation uncertainties were the main source of the footprint geolocation uncertainty, leading to a higher uncertainty to footprint size ratio. Using a high-grade IMU is particularly important if the objects under investigation are small and sparsely distributed. For example, when capturing spectral data of individual grape vine plants with individual plant canopy diameter of about 40–60 cm, a 3° FOV spectroradiometer using a high-grade IMU at 5 m AGL height will result in a ratio of uncertainty to footprint size of 0.20. On the other hand, canopy level spectroscopy of medium-size trees (crown diameter over 3 m) can be performed using a low-grade IMU at 10 m AGL height and with 6° FOV, which provides a ratio of uncertainty to footprint size of 0.17. In general, a lower grade IMU limits our ability to narrow down the sensor FOV and fly at a higher AGL height. Consequently, lower grade IMUs are better suited for spectral sampling over a homogenous and large spatial area (e.g. grasslands), whereas, higher grade IMUs could enable sampling over a spatially heterogeneous areas (e.g. row crops or orchards).

Apart from AGL height and IMU grade, also the optimal size selection of FOV requires careful consideration. To ensure low footprint uncertainty, with respect to the footprint size, it is recommended to set the FOV at least three times larger than the total possible uncertainty of the IMU, which is given by a combination of IMU WGN, boresight angle, drift, and turn-on to turn-on bias. This consideration, despite the uncertainty in the footprint geolocation estimation, will ensure majority (about 1σ, 68%) of the spectral signature originates from the expected location. For instance, if using an IMU with errors reaching as high as $\pm 1°$, then the spectroradiometer FOV is recommended to be no less than 3°. While a large FOV suits better to applications over homogenous targets where spatial resolution of the spectroradiometer is not that crucial, spatially heterogeneous or a small-size targets require a smaller FOV. As a general guide, the FOV is recommended to be as small as possible (depending on the application), however, not less than: 1) three times the total uncertainty from the IMU_gimbal, 2) the minimum required to achieve a certain application-specific ratio of footprint uncertainty to size, and 3) the minimum

required to achieve a certain signal-to-noise ratio of acquired spectral observations.

A high footprint uncertainty to size ratio (Table 3.3) for heterogeneous or small-sized targets, can results in spectral contamination (due to misplacement of footprint), whose tolerance can vary per application. Computation of some robust broad-band vegetation indices, such as for instance NDVI, can tolerate more spectral contamination, whereas a weak vegetation signal such as chlorophyll fluorescence demands low contamination by non-vegetated surfaces as its retrieval requires narrow spectral bands and oxygen absorption features. Despite several attempts to use a spectroradiometer on a UAS to study vegetation spectral properties (Garzonio et al. 2017; Zeng et al. 2017; Burkart et al. 2014; Burkart et al. 2015; Bueren et al. 2015), the level of acceptable spectral contamination resulting from footprint uncertainty to size ratio is still not very well understood.

The signal recorded by the spectroradiometer in digital numbers is proportional to the amount of reflected light acquired within the footprint and the length spectroradiometer integration time. A smaller footprint, resulting from the combination of low AGL and small FOV, typically requires a longer integration time as compared to a larger footprint, which results from the combination of high AGL and large FOV. Increasing the integration time can produce a required signal-to-noise ratio despite a low FOV, however, it will be achieved at the expense of footprint shape elongation.

Compared to the static indoor experiment, we observed an increase of IMU WGN and drifting bias when computing the error budget with in-flight input uncertainties. This increase was likely due to a range of factors associated with flight dynamics, for example, increased platform vibration, small amounts of flexure within each lever arm, and uncertainty associated with the photogrammetric processing chain used as the reference. We conclude that in addition to a suitable sensor selection, the use of a gimbal to dampen the effect of vibrations is essential.

A methodological limitation of this study lies in utilization of a linear error propagation model. The georeferencing Equation 3.3 was linearised using first order Taylor expansion under the nominal conditions of 10 m AGL height, nadir pointing sensor configuration, and sensor specifications presented in Table 2.1. Consequently, the approach can only guarantee accurate computation for conditions similar to the defined nominal acquisition conditions. Nonetheless, the actual flight data of our UAS showed that the attitude of the IMU_gimbal was well within the linear range of trigonometric functions ($\pm 5°$: thus holding our assumption $\sin(angle) \approx angle$, and $cos(angle) \approx 1$).

Another limitation is the treatment of temporally correlated drifting bias. When propagating the variances, the 90% exceedance values of the temporally correlated drifting bias were used as Gaussian noise in the error propagation. We consider this value to be conservative for the purpose of footprint uncertainty assessment, but more rigorous determination of the temporal correlation of the footprint uncertainty was not considered of practical benefit for the UAS spectroradiometer system. Similarly, the input uncertainties were considered to be independent (i.e. covariance in Equation 3.4 was considered to be zero). However, there is a possibility of some correlation among the input error sources.

The proposed method for accurate footprint geolocation determination does not differentiate between spectrally unique or spectrally mixed responses within any given footprint. Accurate geolocation of the footprint aids interpretation of the spectral response depending on the relative size of the target and the sensor footprint. Understanding the accuracy of the footprint geolocation becomes increasingly critical for the appropriate interpretation over highly spatially heterogeneous targets. For example, with regards to the remote sensing retrieval of solar-induced chlorophyll fluorescence of vegetation canopies, the proposed methodology provides information on the geolocation of the retrieved fluorescence spectral emissions. This geolocation information, when combined with ancillary information (e.g. chlorophyll content of plants at the same location), can provide insight in the actual photosynthetic activity and fractional cover of vegetation within the footprint envelope. This can additionally help to spectrally isolate the vegetation chlorophyll fluorescence signal from the abiotic surrounding.

Figure 3.5 and Table 3.3 can serve as a guide for the uncertainty associated with a different combination of sensors. However, for an accurate replication of this error assessment, it is important to test the input uncertainty associated with each sensor device. The proposed approach could be in future extended by incorporation of errors associated with the payload vibration, and their implication on geolocation uncertainty. Furthermore, advanced algorithms, such as simultaneous localization and mapping or Kalman filtering, could be incorporated to reduce the uncertainty associated with the on-board GNSS/IMU.

UAS-based spectroscopy represents a new technology that can facilitate new remote sensing applications, such as vegetation biomass estimation and stress assessments in precision agriculture (Wyber et al. 2017), as well as upscaling and performance validation of optical signals and products recorded by high-altitude air- and space-borne optical sensors, e.g. the airborne hyperspectral spectroradiometer HyPlant (Rascher et

al. 2015) or the high spatial resolution multispectral sensors of the WorldView satellite series (Malenovský et al. 2017). Nevertheless, the UAS technology has still limitations when studying spatially heterogeneous targets composed of small objects. To overcome this shortcoming, it requires to yield a strong spectral SNR from a small footprint on the Earth surface, which assumes use of a spectroradiometer with a smaller FOV and a short signal integration time coupled with a high-grade IMU. Unfortunately, current high-grade IMU modules are too heavy to satisfy the weight limits of UAS payloads. Smaller FOV and shorter integration times are still producing insufficient spectral SNR and slowing down the flying speed for the reduction of footprint elongation, is constrained by achievable duration of a flight mission. To fulfil the above-mentioned application requirements, we need UAS technology of a higher payload capacity that can carry spectroradiometers with a foreoptic capable to produce sufficiently large SNR, even when using narrow FOV and short integration times, and MEMS-based IMU technology providing sufficiently accurate sensor orientation data. This progression would collectively allow the UAS-based point spectrometry to work with small-size footprints collected from greater flying heights with acceptably low geolocation uncertainty, which opens new capabilities in observing even single plants over relatively large study areas.

3.5 Conclusion

We investigated the uncertainty in geolocation of the footprint for a spectroradiometer on-board a small unmanned aircraft system. The direct georeferencing technique applied in this study uses a global navigation satellite system receiver for sensor positioning and an inertial measurement unit for its orientation determination. We demonstrated how the variance of individual errors, originating from independent sources, can be estimated and propagated to estimate the overall accuracy of the spectroradiometer footprint geolocation. We assessed the relative error contribution of several input parameters such as the above ground level flying height, grade of IMU, spectroradiometer integration time, spectroradiometer field of view, and UAS flight speed in relation to the shape, size, and geolocation uncertainty of the footprint. The spectroradiometer footprint typically has the shape of an elongated circle, where the across-track width is determined by the FOV and AGL height, and the along-track length was the function of spectroradiometer integration time and UAS flight speed. The investigated UAS spectroradiometer footprint was 140 cm wide across-track and the 320 cm long along-track for the FOV of 8°, AGL height of 10 m, spectroradiometer integration time of 0.6 s, and UAS flight speed of 3 m/s. The geolocation uncertainty of this particular footprint was found to be ≈11 cm (footprint uncertainty to diameter ratio equal to 0.08).

The AGL flying height was found to be one of the major determinants of footprint accuracy for a given accuracy of the used IMU. When the flying height was fixed, the uncertainty in IMU measured orientation of the spectroradiometer had the second largest influence on the overall geolocation accuracy. With the increase in flying height, the rate of increase in footprint uncertainty was found to be higher for the lower grade IMU. Other factors, such as lever-arm offset uncertainty and orientation of the IMU on the airframe, had a relatively low impact. From a footprint error budget perspective, it is recommended to reduce the flying height and to increase the sensor FOV. A larger FOV will keep the footprint size comparable to those for higher AGL altitudes and simultaneously strengthens the signal recorded by a spectroradiometer. However, a lower AGL and larger FOV require accurate control of the AGL distance during flight operations. With the current pace of technological progress, we foresee development of new more sensitive spectroradiometers that will allow for reduction of integration time, facilitating a narrower FOV, and resulting in small-size footprints. This will require a deep understanding of the spatial uncertainty in footprint location and extent as outlined and demonstrated in this work.

3.6 Thesis Context

This chapter built foundations for this thesis by developing an aerial georeferencing error budget model to estimate the footprint uncertainty of the spectroradiometer mounted on a UAS. This chapter identified the crucial parameters as well as drew operational recommendations to reduce the footprint uncertainty. A finding of this chapter that shapes the next chapter is the importance of lower IMU errors and lever-arm correction for footprint uncertainty. Consequently, the next chapter calibrates the lever-arm offset and boresight angle to achieve better spatial estimates of the footprint.

4 | Lever-arm and boresight correction, and field of view determination of a spectroradiometer mounted on an unmanned aircraft system

Chapter 4 calibrates the lever-arm offset and boresight angle, and determines the field of view for the UAS-spectroradiometer system. The aim of this calibration is to enable accurate computation of the spectroradiometer footprint geolocation and determination of the footprint extent. The work comprising this chapter was submitted for publication in *ISPRS Journal of Photogrammetry and Remote Sensing* (21 March 2018).

Abstract

This study addresses the correction of lever-arm offset and boresight angle, and field of view (FOV) determination to enable accurate footprint determination of a spectroradiometer mounted on an unmanned aircraft system (UAS). To characterise the footprint, an accurate determination of the spectroradiometer position and orientation (pose) must be acquired with a global navigation satellite system (GNSS) and an inertial measurement unit (IMU). Accurate pose estimation requires an accurate lever-arm and boresight correction between the pose measuring sensors and the spectroradiometer. Similarly, the spectroradiometer FOV is required to determine the footprint size as a function of above ground level (AGL) flying height. The system used in this study consists of an IMU with dual-frequency and dual-antenna GNSS receiver, a machine vision camera, and a point-measuring spectroradiometer (Ocean Optics QE Pro). The lever-arm offset was determined from a scaled 3D point cloud of the system, created using photos of the airframe and processed with the structure-from-motion (SfM) algorithm. The boresight angles were estimated with stationary experiments by computing the difference between the orientations of the IMU, the spectroradiometer, and the camera. The orientation of the spectroradiometer was determined by moving a spectrally distinct target into the FOV. The orientation of IMU was measured by averaging its readings during the stationary epoch, while SfM was employed as an independent technique to estimate the orientation of the camera. The footprint of the spectroradiometer for a known AGL height was determined experimentally resulting in a FOV of $7.12°(\pm 0.40°)$. In-flight validation of the lever-arm and boresight correction was performed by comparing the corrected pose of the co-mounted camera with the pose derived from SfM as the

reference. Our experimental results demonstrate that controlled determination and correction of lever-arm and boresight increases the pose estimation accuracy and thereby supports the direct geolocation of a UAS-mounted spectroradiometer point observation.

4.1 Introduction

The use of spectrometers mounted on unmanned aircraft systems (UAS) to study biophysical and biochemical properties of terrestrial vegetation has increased in recent years (Pajares 2015; Colomina and Molina 2014; Zarco-Tejada et al. 2016; Aasen et al. 2015; Lucieer et al. 2014). It has been shown that point-measuring spectroradiometers has a strong potential in accurate retrieval of sun-induced chlorophyll fluorescence (Cogliati et al. 2015a; Rascher et al. 2015; Meroni et al. 2009), and photochemical reflectance index (PRI) (Panigada et al. 2014). Both of which are crucial in monitoring vegetation stress (Ač et al. 2015), photosynthetic activity (Rossini et al. 2015; Pinto et al. 2016; Wyber et al. 2017), and modelling gross primary productivity (Damm et al. 2015; Wieneke et al. 2016). When mounted on a small-sized UAS (Burkart et al. 2014; Garzonio et al. 2017), the spectroradiometer offers sampling at a high spectral and spatial resolution. Accurate determination of the location and extent of the sampled area, also known as footprint, therefore becomes essential to make a correct interpretation of the spectroradiometer measurements. Computation of the footprint requires position measurements from an on-board global navigation satellite system (GNSS) and orientation measurement from an on-board inertial measurement unit (IMU).

Despite careful manufacturing of the UAS sensor payload, minor boresight (angular misalignment between the mounting axes of the IMU and on-board sensor) and lever-arm (physical offset from the GNSS antenna to the on-board sensor) can occur. The correction of boresight (typically $\pm 2^{\circ}$) is necessary for accurate orientation determination, and the lever-arm (typically 0.1–1.0 m for a small-sized UAS) is required for accurate position measurement. The lever-arm offset is constant in the local coordinate frame of the IMU, but changes dynamically in the geographic coordinate frame as the platform orientation changes during flight (Chiang et al. 2015). If not accounted for, the lever-arm and boresight misalignment results in systematic pose error of the spectroradiometer and the subsequent error in footprint geolocation. For instance, for a UAS flying at 10 m height, 2° boresight angle results to total footprint geolocation error of about 35 cm which amplifies with flying height. Similarly, a 50 cm lever-arm offset between the GNSS and the spectroradiometer results in a footprint geolocation error of about 50 cm if not corrected. Given the above, correction of boresight and lever-arm are required especially for high accuracy geospatial applications of UAS (Gautam et al.

2017).

Geolocating the footprint of a UAS-mounted spectroradiometer directly without the use of GCPs and a photogrammetric bundle adjustment, requires an accurate measurement of pose at the moment of spectral acquisition. The accuracy of the pose estimation is directly related to the accuracy of the footprint geolocation determination. While geolocation of an airborne imaging sensor such as a camera (Harwin and Lucieer 2012) can use techniques such as bundle adjustment for high accuracy geolocation without being dependent on correction of lever-arm and boresight alignment, most of the UAS-mounted pointing and non-imaging sensors (e.g. LIDAR, spectroradiometer, pushbroom spectrometer (Lin et al. 2011; Hruska et al. 2012)) require these corrections for accurate footprint estimation.

Algorithms to compensate for predetermined lever-arm offset and boresight angle are well-explored (Chiang et al. 2012a; Chiang et al. 2015; Daakir et al. 2016), yet techniques to determine these parameters are less frequently presented within the literature. The most common technique to determine the lever-arm offset is manual measurement (Wallace et al. 2012; Rehak et al. 2013; Turner et al. 2012b; Turner et al. 2017; Suomalainen et al. 2014), whereas boresight angles are sometimes neglected (Wallace et al. 2012), or determined iteratively by adjustment in photogrammetric software (Suomalainen et al. 2014). Other techniques involve parameterisation of the lever-arm offset and boresight angle by adjustments that involve airborne data via multiple passes of the airborne sensor over the same target and surveyed ground control points (GCPs)(Williams et al. 2013; Chiang et al. 2012a; Glennie 2007; Rieger et al. 2010). However, the lever-arm and boresight correction for a UAS-mounted spectroradiometer mounted on a gimbal presents unique challenges. First, the inclusion of gimbal meant the split of lever-arm offset at the gimbal centre resulting in two offsets. Second, unlike LiDAR, a spectroradiometer lacks range measurement to the point being measured, thus, cannot utilise the geometric shape of the target surface to determine the boresight angle. Third, unlike an imaging sensor, the non-imaging spectroradiometer measurement comprises of a single spectral measurement without spatially defining features, thus, cannot utilise visible features (such as a GCPs) to help with boresight angle determination. Thus, the most common methods of using GCPs and topography (such as for a camera or a LiDAR (Skaloud and Lichti 2006; Mitishita et al. 2016; Yastikli and Jacobsen 2005; Habib et al. 2010)) for in-flight boresight correction of UAS-mounted sensors (Williams et al. 2013; Chiang et al. 2012a) are not as feasible for a spectroradiometer (Aasen et al. 2018).

The aim of this paper is to enable accurate footprint determination of a spectrora-

diometer mounted on a UAS. We focus on estimation and correction of lever-arm and boresight, and determination of the spectroradiometer FOV, which are essential to characterise the footprint. A photogrammetric technique is adopted to create a scaled 3D model of the UAS spectroradiometer system, and using the 3D model, the lever-arm offset from the GNSS antenna phase centre to the spectroradiometer reference point is measured. A series of indoor and outdoor experiments are proposed to estimate the inter-sensor boresight angles by observing the difference in pointing angle of each sensor under static conditions. The spectroradiometer FOV is estimated by determining the size of the spectroradiometer footprint for a known height above ground level (AGL). We apply the correction of the lever-arm and boresight on a flight dataset to demonstrate the improvement in pose estimation and subsequent footprint geolocation determination.

4.2 Material and methods

4.2.1 Sensor Payload

The UAS spectroradiometer system used in this study employed an off-the-shelf heavy-lift multirotor, a DJI Matrice 600 (Dà-Jiāng Innovations Science and Technology Co., Ltd., China). The custom-built sensor payload contains a spectroradiometer (Ocean Optics QE Pro, Florida, USA) along with supporting electronics and pose sensors. A gimbal (Foxtech Eagle Eye DSLR aerial gimbal) was used to provide a stabilised mount for the spectroradiometer to sustain its nadir pointing configuration. Also installed on the gimbal was a microelectromechanical system (MEMS) based IMU (Advanced Navigation Spatial Dual, Sydney, Australia) and a machine vision camera (FLIR Grasshopper GS3-U3-23S6M-C, British Colombia, Canada). The Spatial Dual is a coupled GNSS/IMU sensor with a multi-frequency and multi-constellation GNSS receiver. Supporting sensors outside the gimbal (attached to airframe) included a MEMS-based IMU/GNSS (Lord MicroStrain 3DM-GX3-35, Vermont, USA) and a dual antenna GNSS system (Antcom G5Ant-1.9A4-XTB-1, Torrance, California) for the Spatial Dual. An on-board computer (NUC i5, Intel, Santa Clara, California) was used for sensor configuration and data logging (Figure 4.1). The QE Pro spectroradiometer has a spectral range of 500–877 nm, a spectral sampling interval of 0.33 nm, full width at half maximum of 0.8 nm, and 18-bit digital range. Its downward facing foreoptics (FOV of approximately 25°) was equipped with a Gershun tube restricting FOV of the spectroradiometer to 8°.

The two GNSS antennae were rigidly mounted on the airframe above the propellers, at 1.04 m separation, thereby providing a clear and unobstructed view of the sky. The MicroStrain IMU was rigidly mounted midway between the two antennae. The yaw axis of the Spatial Dual (i_g axis in Spatial Dual coordinate frame G) was aligned and

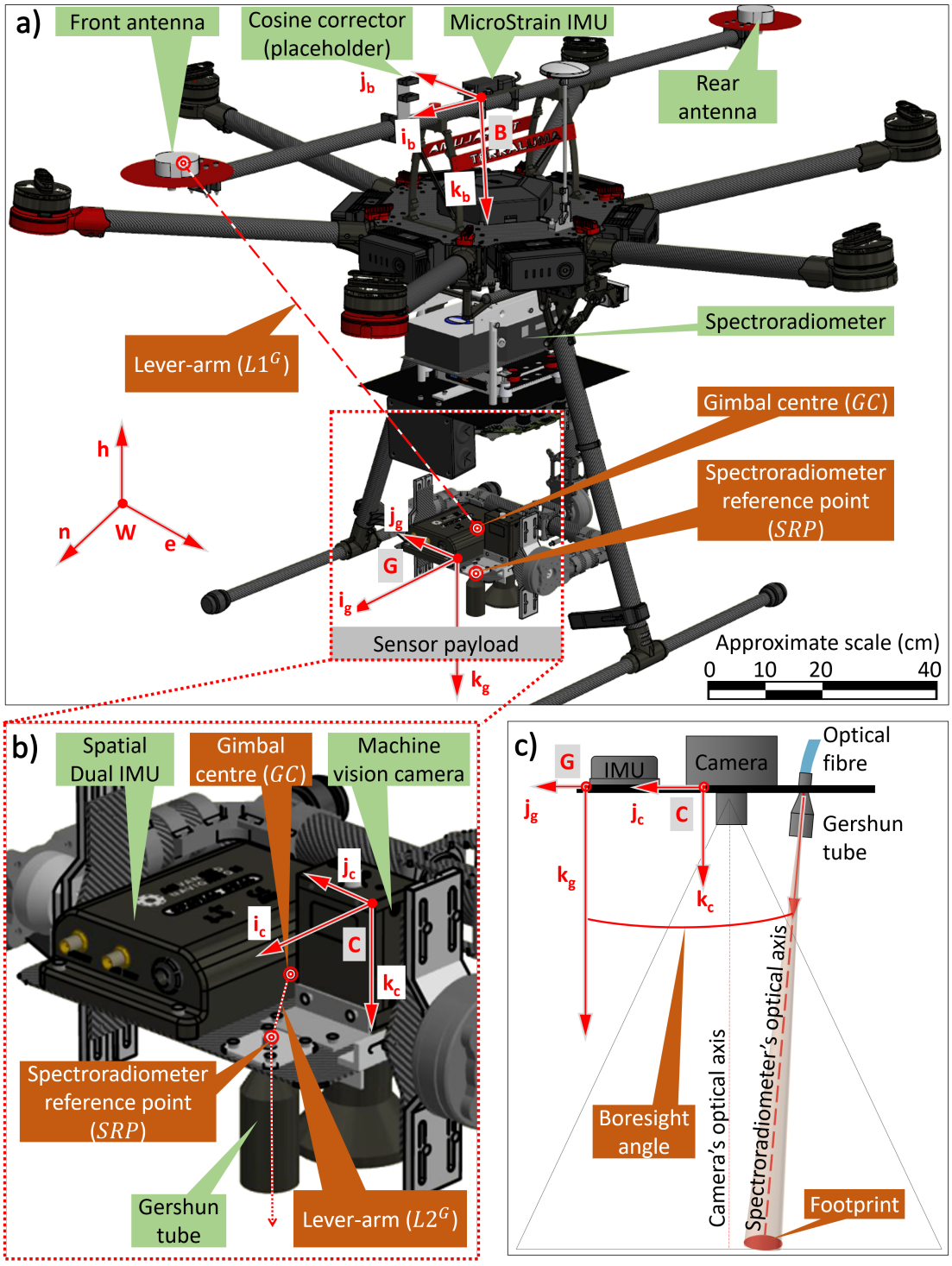

Figure 4.1: TerraLuma UAS spectroradiometer system: a) with its components and lever-arm offset between front antenna and gimbal centre (GC). b) A detailed view of the sensor payload in the gimbal with lever-arm offset between GC and spectroradiometer reference point (SRP). c) A schematic representation of the boresight angle between IMU and spectroradiometer.

fixed with the dual antenna pointing direction, and the yaw axis of the MicroStrain IMU (i_b axis in MicroStrain IMU coordinate frame B) (see Figure 4.1). This mounting configuration allowed the use of the dual antennae system to estimate the absolute heading for the Spatial Dual IMU, MicroStrain IMU, camera, and the spectroradiometer. The spectroradiometer had a bifurcated fibre optic cable allowing measurement of the upwelling radiance via a Gershun tube (Parr et al. 2005) and downwelling solar irradiance via a cosine corrector. The downward facing Gershun tube was rigidly mounted on the gimbal along with the Spatial Dual IMU and camera (Figure 4.1).

4.2.2 GNSS antenna to spectroradiometer lever-arm offset

Let the spectroradiometer reference point (SRP) be defined by the point where the upwelling radiance from the ground enters the downward-looking spectroradiometer's Gershun tube (i.e., the origin of the spectroradiometer's FOV). To estimate the SRP position in the gimbal, using the position measurements of the front GNSS antenna, the identification of the lever-arm offset is required. The lever-arm from the front GNSS antenna phase centre (A1) to SRP, due to the inclusion of the gimbal, was composed of two offsets with differing orientations: the lever-arm from A1 to the gimbal centre (GC) referred to as $L1^G$ and the lever-arm from GC to SRP referred to as $L2^G$ (Figure 4.1). The two offsets necessitated the use of a second IMU (MicroStrain) to determine the orientation of the $L1^G$ lever-arm offset, while the primary IMU (Spatial Dual) measures the orientation of the $L2^G$ lever-arm offset.

The UAS spectroradiometer system was placed on a flat board with 10 surveyed GCPs (3 mm radius pins) located at varying heights (Figure 4.2). The GCPs were surveyed, using a 30 cm long stainless steel ruler, in a local coordinate frame defined on the flat board, and approximately aligned with the G coordinate frame. The smooth and reflective exterior body surface of the sensor was highlighted with coloured tapes to facilitate identification in photogrammetric software (Agisoft PhotoScan Professional version 1.3.0) for feature extraction and matching around important surfaces (surfaces that are necessary to determine the reference point of sensors). The UAS spectroradiometer system was then photographed using a Nikon D5100 to acquire a series of 273 overlapping images from multiple directions at varying heights and angles.

The overlapping images were then processed using Agisoft PhotoScan to derive a dense 3D point cloud of the UAS (Figure 4.3). Images were aligned with settings of highest accuracy, and limits of 100,000 key points and 10,000 tie points. High-quality settings and mild filtering mode were used to create the dense point cloud. The dense point cloud was scaled using surveyed GCPs to produce an absolute size model of the UAS

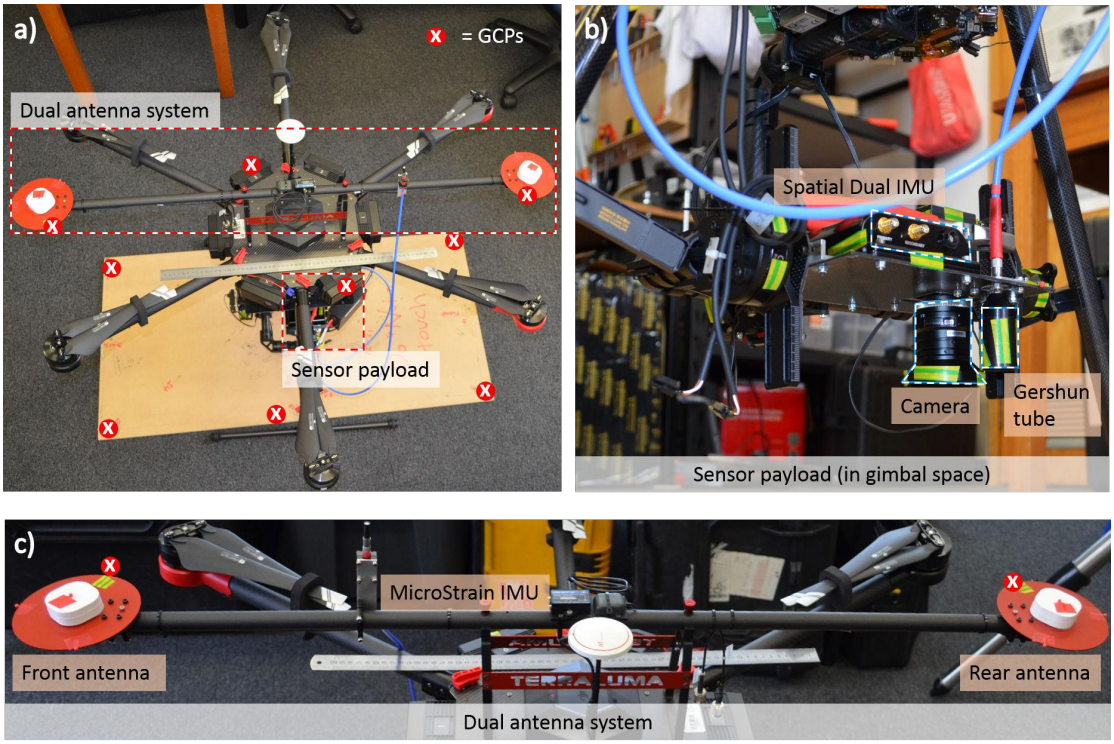

Figure 4.2: The UAS spectroradiometer system: a) with experimental setup prepared to produce a scaled 3D point cloud of the system that b) included the sensor payload and c) the dual antennae system. Note the surveyed GCPs used for 3D reconstruction indicated with an 'x'.

spectroradiometer system. This scaled point cloud was then imported into AutoCAD (Autodesk AutoCAD 2016) where the offsets between the SRP and A1 were measured (McCoull 2016).

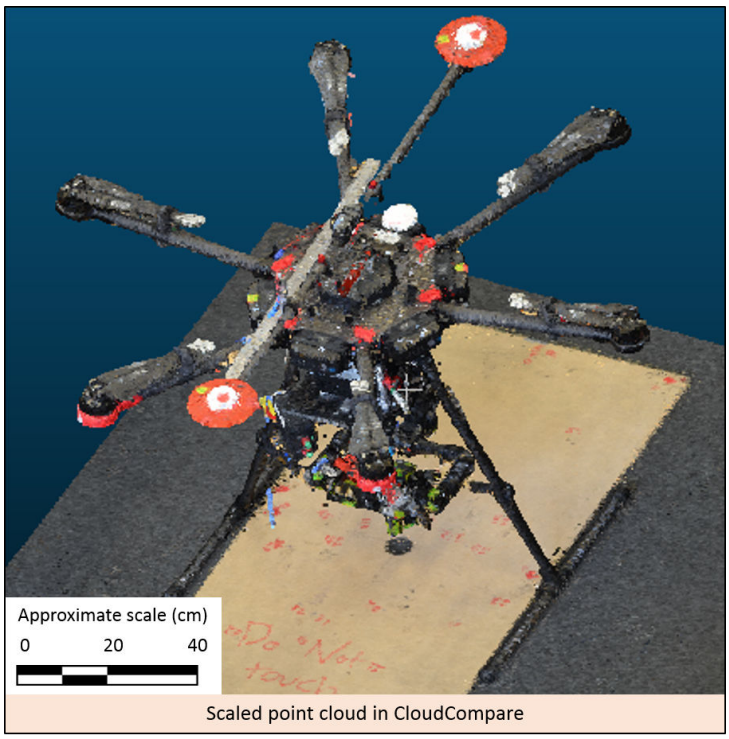

Figure 4.3: High density point cloud of the TerraLumma UAS spectroradiometer system used to measure the lever-arm offset between the sensors.

To correct for the lever-arm after measurement, the local offsets were converted to global lever-arm (expressed in geographic coordinate frame W) by applying rotation as per the attitude matrix of the IMUs. These global offsets were applied in sequence to compensate for the total lever-arm and hence compute the position of the SRP in the geographic coordinate frame (MGA 55 for our applications) as presented in Equation 4.1 and Figure 4.4.

$$SRP^W = A1^W + \mathbf{R}_B^W \times L1^G + \mathbf{R}_G^W \times L2^G \tag{4.1}$$

where, $A1^W$ is the position of A1 in W coordinate frame, the attitude matrix $\mathbf{R}_B^W$ represents the orientation of the MicroStrain IMU, and $\mathbf{R}_G^W$ is the attitude matrix parameterized using the orientation of the Spatial Dual IMU. $L1^G$ is the offset from A1 to GC, $L2^G$ is the offset from GC to the SRP in the local Spatial Dual coordinate frame.

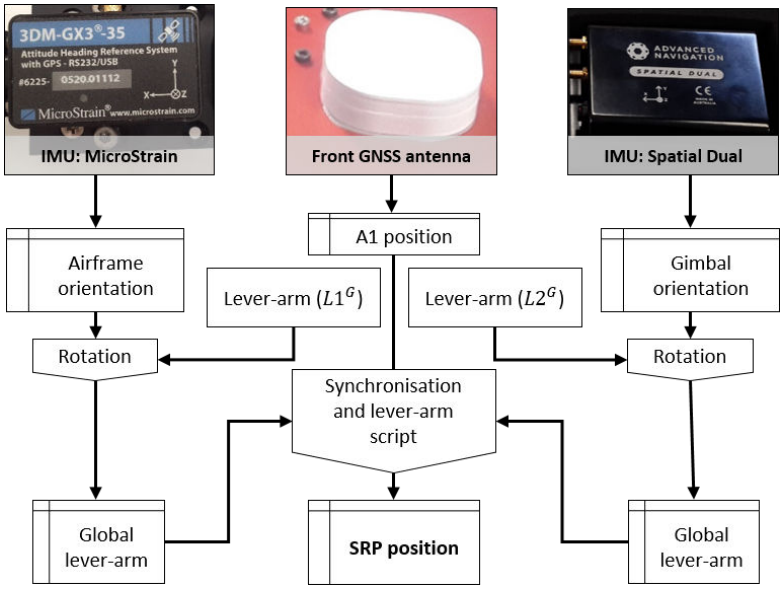

Figure 4.4: Lever-arm correction workflow to estimate the position of spectroradiometer's reference point taking A1 position, orientation from two IMUs, and the lever-arm offset as input.

4.2.3 Inter-sensor boresight correction

The proposed experimental method for boresight calibration requires controlled and even lighting conditions (such as indoor laboratory conditions) for the spectroradiometer, however, the GNSS/IMU requires unobstructed satellite view (i.e. outdoors). To solve this issue, we split the boresight correction between spectroradiometer and IMU to a) between the spectroradiometer and the camera and b) between the camera and the IMU. Camera and IMU boresight angles are determined outdoors whereas the camera and the spectroradiometer boresight angles are determined indoors. The camera offers the ability to combine the indoor and outdoor experiments and thus compute the boresight between the IMU and spectroradiometer.

Boresight angle between the spectroradiometer and the camera

The boresight angle between the spectroradiometer and the camera enables estimation of the spectroradiometer orientation using the orientation of the co-mounted camera. The mounting plate in the gimbal, which contained the Spatial Dual IMU, camera, and the Gershun tube, was moved onto a tall survey tripod for static indoor experiments. The mounting plate was placed at a working distance of 310 cm height above the floor with the Gershun tube and the camera pointing vertically down. Twenty-five GCPs, on top of the black panel (corflute sized 2 x 2 m), within the FOV of the camera were surveyed, in geographic coordinate frame, using a total station (Leica Geosystems Leica Nova MS50). The experiment was performed indoors with a halogen light used as the

only source of illumination.

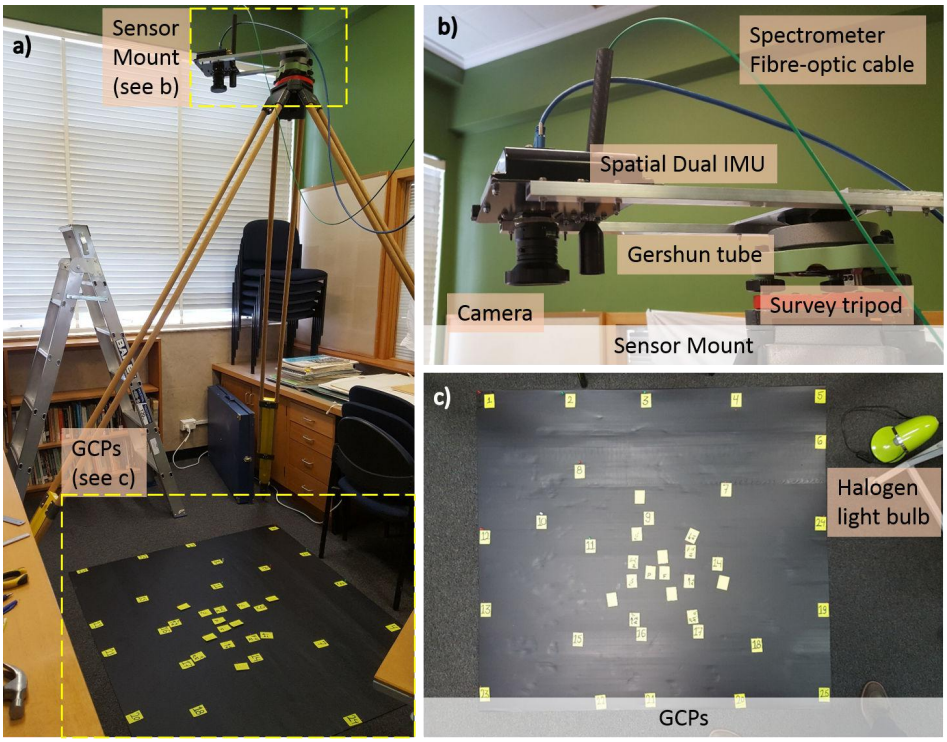

Figure 4.5: a) The experimental setup prepared to determine the boresight angle between the camera and the spectroradiometer. b) The *in situ* sensors were removed from the UAS and placed level on a survey tripod c) at 3.10 m height above the GCPs.

To determine the footprint centre location for the stationary setup (Figure 4.5), a rectangular white panel (corflute) was placed parallel to the image frame of the camera by aligning the edges of the panel to the vertical and horizontal array of image pixels. A black panel (corflute sized (1.2 x 1.2) was then moved, along the positive i_c axis (of the camera coordinate frame, C), on top of the white panel until a DN value change of predefined tolerance was noticed in the spectroradiometer's live data display. The DN tolerance was set to a minimum difference in radiance required to confirm a change in spectroradiometer footprint. For instance, for a DN value peak of 45,000 (complete footprint in the white panel) and noise bandwidth in the live data display of about 1,000 DN, the DN tolerance was set to 1,000. Whenever a change in DN value reached the threshold, the footprint edge was considered to be next to the edge of the black panel. Using this technique, four locations were marked on the white panel: 1) the point where the black panel starts entering the footprint, 2) the point where the black panel is completely inside the footprint, 3) the point where the black panel starts exiting the footprint, and 4) the point where the black panel completely exits the footprint. This experiment was conducted along forward and reverse direction of the camera roll axis i_c and pitch axis j_c. Again the entire experiment was repeated with repositioning of the

light source to tackle the potential for minor bias on footprint location estimation, which was found to be biased towards the light source as observed during the experiments.

Using the marked locations of the 16 footprint edges, the footprint centre was estimated. The location of the footprint centre and the SRP were surveyed using the total station. This enabled computation of the offset from the SRP to the footprint centre in a geographic coordinate frame. The offset was then transformed to the camera coordinate frame (C) by applying a rotation (equal to camera heading) about the vertical axis as presented in equation 4.2.

$$\begin{bmatrix} x' \\ y' \end{bmatrix} = \begin{bmatrix} cos\psi & sin\psi \\ -sin\psi & cos\psi \end{bmatrix} \begin{bmatrix} x \\ y \end{bmatrix} \tag{4.2}$$

where $(x, y)^T$ is the offset from the SRP to the location of the footprint in the geographic coordinate frame, $(x', y')^T$ is the offset in camera coordinate frame after applying the rotation of ψ heading angle. The offset in the camera frame for a given AGL height h (3.10 m) was then used to compute the roll and pitch pointing angle of the spectroradiometer about the camera axis (See Equation 4.3).

$$\begin{bmatrix} \phi_{spec} \\ \theta_{spec} \end{bmatrix} = \begin{bmatrix} \arctan(\frac{x'}{h}) \\ \arctan(\frac{y'}{h}) \end{bmatrix} \tag{4.3}$$

Boresight angle between the camera and the IMU

The boresight angle between the camera and the IMU is a constant angle that incorporates the physical sensor mounting misalignment, constant sensor bias, internal gyroscope/accelerometer mounting misalignment, camera CCD mounting misalignment, and other constant errors. In-flight correction of boresight between IMU and camera has been extensively explored for navigation and mapping purposes (Mirzaei and Roumeliotis 2008; Weiss et al. 2012). However, the in-flight method is influenced by white Gaussian noise (WGN) and temporal drift typically present in low-cost MEMS-based IMUs. This noise and drift are difficult to isolate in flight, without the ability to carry a high-grade IMU as a reference (further complicated by UAS flight dynamics and vibrations). Thus, we propose a stationary experiment, which has minimal influence from the IMU temporal drift and IMU WGN, and is not impacted by the flight dynamics and vibrations of the UAS platform.

The UAS spectroradiometer system (including the UAS and all the sensors) was placed on top of 4 survey tripods with a downward facing configuration of mounted sensors (see

Figure 4.6). This working distance of 210 cm resulted in an image footprint of approximately 280 cm × 210 cm. A flat board with 10 GCPs was placed in the field of view of the camera. The total station was used to survey the GCPs in a geographic coordinate frame. The experiment consisted of 14 epochs of 2–5 minutes in duration with all setup held stationary. For each epoch, the camera captured 3–4 images while the IMU recorded orientation at 100 Hz. Images from each epoch were then processed in Agisoft PhotoScan (to compute the camera orientation) with the highest accuracy setting, 100,000 key points and 10,000 tie points limit, and fixed camera calibration. Camera orientation and the averaged IMU orientation were used to compute the boresight angle between the two sensors.

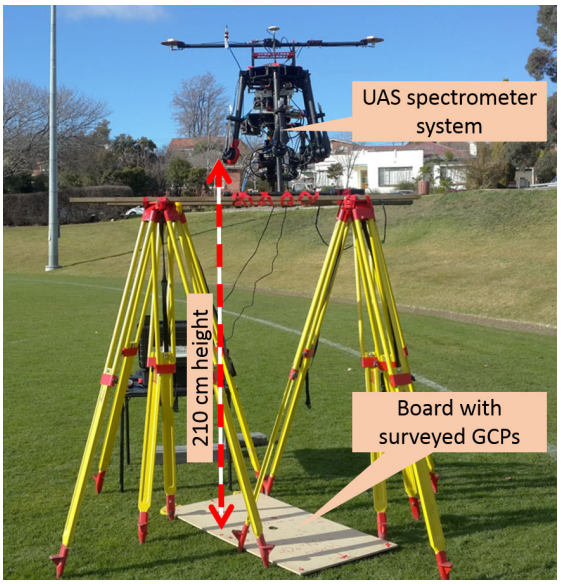

Figure 4.6: Outdoor stationary experimental setup to determine the boresight angle between the IMU and the camera. The UAS is 2.10 m above the ground.

4.2.4 Footprint size of the spectroradiometer

The spectroradiometer bare optical fibre had an approximate FOV of 25°, which is known to be non-circular in shape (Mac Arthur et al. 2012). A Gershun tube was used in front of the optical fibre to restrict the acceptance angle of photons into the spectroradiometer using interchangeable apertures made from machined aluminium aperture rings. The apertures were circular in shape and only allowed photons from the central region of the foreoptics FOV to enter the spectroradiometer. This restricted the photons that are towards the periphery of the foreoptics 25° FOV, which is predominantly where the irregularity in FOV shape lied (Mac Arthur et al. 2012). For example, an 8° FOV restrictor on a 25° foreoptics, left only the central 10% of original sampling area and blocked approximately 90% of area towards the extremities (see Figure 4.8).

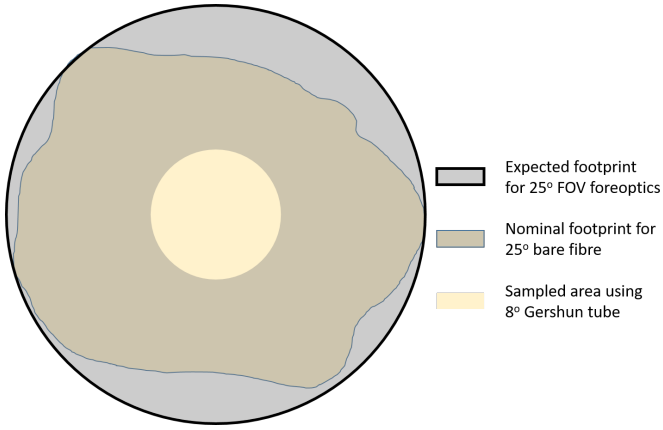

Figure 4.7: The circularity of the FOV and footprint defined by the aperture ring of Gershun tube.

Even though the apertures rings of the Gershun tube were machined from a solid aluminium material (standard FOV: 1°, 3°, 8°, 10° and 14°), any error in the ring diameter and placement of the aperture ring impacts on the FOV value and the size of the footprint. As an example, a 1 mm discrepancy in diameter of the 8° FOV aperture at the 10 m AGL height results in about 21 cm alteration in footprint diameter. Similarly, a 1 mm discrepancy in the vertical distance between the aperture ring and the fibre optic entrance leads to about 3 cm change in footprint size. For this reason, the FOV values of each aperture ring had to be experimentally determined.

Methods such as reverse illumination is found in literature to compute the size of the FOV, which requires a specific spectral calibration equipment unavailable for this study (Caras et al. 2011; Mac Arthur et al. 2012; Schaepman 1998). Therefore, FOV, in this study, is experimentally determined from the footprint size produced by each FOV aperture ring at a known acquisition distance. This allows computation of an accurate FOV angle and the size of the footprint as a function of AGL height (10—20 m for typical UAS application). To determine the size of the footprint for a known height, a survey tripod was used to fix the Gershun tube pointing approximately nadir. We placed a white panel (60 × 120 cm) directly underneath the Gershun tube. A black panel, placed over the white panel, was moved away from the approximate footprint location and rise in DN value was monitored in the spectroradiometer live data display (see Figure 4.8). The estimated locations of the footprint were marked whenever a rise in DN value reached the threshold value (defined in Section 4.2.3). The marked tangential locations of the footprint were used to estimate the size of the footprint.

The footprint size was tested for several combinations of aperture rings and AGL heights. The estimated footprint size had higher errors for low incoming light levels, such as for

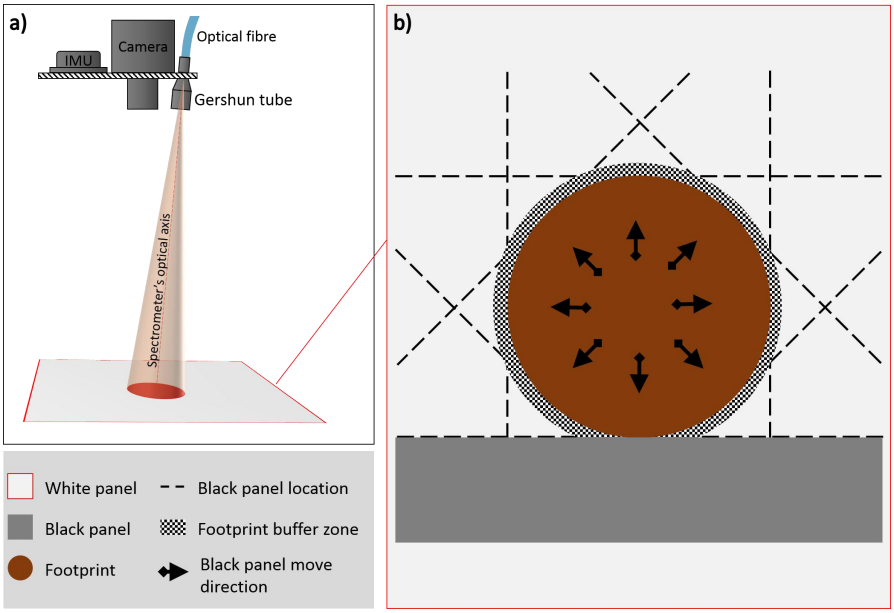

Figure 4.8: Experiment to estimate the spectroradiometer footprint size. a) A schematic of sensor mount and footprint of the spectroradiometer. b) Proposed method to estimating footprint size by radially moving black panel away from the approximate footprint location.

a combination of a small aperture ring opening, short integration time, and low AGL height. However, a longer integration time and higher AGL height enabled working with larger DN values, which in return increased the estimation accuracy. Subsequently, experiments were performed at the highest AGL height feasible (238 cm) in the laboratory. The footprint size measurements were repeated nine times where the aperture rings and Gershun tube were removed and replaced each time. Thus computed footprint size, for each aperture ring enabled computation of the spectroradiometer FOV.

4.2.5 Validation of lever-arm and boresight correction

The co-mounted camera was used to validate the correction of lever-arm and boresight under flight conditions. The flight was a cross-grid pattern over relatively flat terrain consisting of surveyed GCPs. The high frame rate (25 Hz) images captured from the machine vision camera were sub-sampled (to produce 90% forward overlap) and processed in Agisoft PhotoScan (aligned with the highest accuracy, 100,000 key point and 10,000 tie point settings) to compute the reference camera position and orientation of the image frames. The GNSS antenna position and IMU orientation were corrected for the lever-arm between the A1 and camera reference point and boresight between the IMU and the camera respectively. To validate the correction, the lever-arm corrected camera position and boresight corrected camera orientation were compared with the reference camera pose derived from Agisoft PhotoScan.

4.3 Results

4.3.1 Lever-arm correction

The lever-arm offsets between A1, the SRP, and the camera reference point determined using the scaled 3D point cloud of the UAS spectroradiometer system are listed in Table 4.1. The lever-arm offset estimation accuracy depends on the accuracy of GCP measurements, the SfM modelling inherent errors, and the sensor reference point estimation accuracy within the pointcloud. The GCPs were measured using a stainless-steel ruler as well as a plumb bob. The uncertainty in ruler measurement was about ±0.1 cm, whereas the plumb bob measurement was more uncertain. Thus, the maximum uncertainty of GCP measurements is considered to be ±0.3 cm. This uncertainty, combined with the uncertainty in SfM inherent modelling, translates to the uncertainty in the 3D model. The SfM inherent uncertainty, since the images were captured from very short distance of less than 1.5 m, is considered to be within the measurement precision of the GCPs. The uncertainty with the 3D model of the UAS is, therefore, considered to be about ±0.4 cm. If the uncertainty associated with identifying reference point within the pointcloud is considered to be ±0.3 cm (at the worst), the total uncertainty associated with the lever-arm offset estimation computed by summing in quadrature the above two uncertainties is equal to ±0.5 cm.

Table 4.1: The lever-arm offset measured from a scaled point cloud of the UAS spectroradiometer system in Spatial Dual IMU coordinate frame axes (i_g, j_g, k_g).

Lever-arm	Offset [cm] in G coordinate frame
From A1 to GC	(-50.6, 0.2, 63.9)
From GC to SRP	(4.6, -4.4, 1.8)
From GC to camera reference point	(-0.7, -4.5, -0.8)

These offset measurements can be used to compute the position of the SRP (Equation 4.1) and the position of camera reference point. For the validation purpose, the lever-arm correction (from A1 to camera reference point) is applied for a cross-grid pattern flight and compared with the Agisoft PhotoScan derived camera positon taken as reference. The comparison with the reference camera position yields errors in the order of 80 cm before and 3-8 cm (mean 6.3 cm, standard deviation 2.5 cm) after the lever-arm correction (see Figure 4.9). Similar error is expected in the estimated position of the SRP after lever-arm correction.

The northing error in Figure 4.9a) is about 40 cm throughout the cross-grid pattern flight whereas the easting error changes from about 40 cm to about -40 cm for the second half of the flight. This is due to the two different heading angles for the two

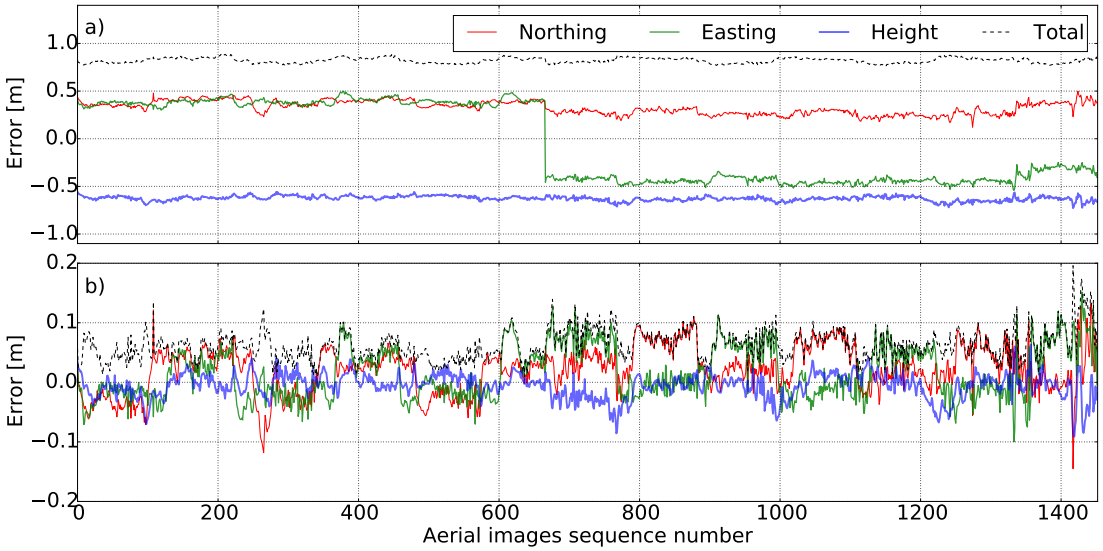

Figure 4.9: Error marked by the difference in GNSS receiver recorded position and reference camera position (derived through Agisoft PhotoScan) for a section of flight: a) before lever-arm correction and b) after lever-arm correction.

parts of the cross-grid pattern flight. For the first part of the cross-grid flight, the heading was fixed at approximately 225° i.e. offset from A1 to camera was aligned with north-east direction. Thus the total lever-arm offset about the horizontal plane was almost equally distributed as northing error and easting error. However, for the second part of the flight, the heading angle was fixed at approximately 315° i.e. offset from A1 to camera was aligned with north-west direction leading to distribution of the lever-arm offset as northing error and negative easting error.

4.3.2 Boresight correction

The boresight angles between the spectroradiometer, camera and IMU are summarised in Table 4.2. The boresight from the IMU to the spectroradiometer was -1.25°, -1.18°, and -1.27° about the roll, pitch, and heading axis respectively. The correction of these boresight angles between the spectroradiometer and IMU is equivalent to an improvement in the footprint geolocation estimation by about 30 cm for a flying height of 10 m AGL.

Table 4.2: The boresight angle between the IMU, camera and the spectroradiometer determined from the proposed indoor and outdoor experiments.

From	To	boresight (roll, pitch, heading)
IMU	Camera	(0.35°, -0.63°, -1.27°)
Camera	spectroradiometer	(-1.59°, -0.55°, 0.00°)
IMU	spectroradiometer	(-1.25°, -1.18°, -1.27°)

The boresight uncertainty between the IMU and the spectroradiometer depends on the errors associated with the independent orientation of 1) the IMU, 2) the spectroradiometer, and 3) the camera. First, the IMU orientation uncertainty was approximately $\pm 0.08^\circ$ after averaging the 100 Hz data over 1 minute. This includes contributions from WGN uncertainty (negligible), and drift uncertainty as determined by 90% exceedance probability of the IMU drift over the averaging duration. Second, the spectroradiometer footprint location was within ± 1 cm for each repetition of the experiment, implying that the orientation of the spectroradiometer was within $\pm 0.18^\circ$. Third, the pointing angle of the camera was determined using images and surveyed GCPs through the SfM workflow. Propagation of the uncertainty in multiple GCPs through the PhotoScan process is non-trivial. Variance and covariance propagation of the uncertainty in a single GCP ($\pm$ 0.5 cm) observed from a distance of 3.1 m resulted in an uncertainty in camera orientation of $\pm 0.09^\circ$. This uncertainty is an upper limit as in reality, the use of multiple GCPs will reduce the final uncertainty. Finally, we compute the boresight uncertainty between the IMU and the spectroradiometer by propagating the errors associated with each of three components. For the propagation of error, we take the conservative approach and consider the above-computed uncertainties of the components as a 1σ estimates. summing in quadrature the uncertainties of each component above yields the total uncertainty in the boresight angle between the IMU and the spectroradiometer $\pm 0.22^\circ$, 1σ

To demonstrate the improvement in orientation estimation due to the boresight, correction from IMU to the camera was applied to the IMU data over the cross-grid pattern flight. The correction showed increased agreement when compared with the reference camera orientation. The comparison yields reduced mean orientation error after boresight correction (mean roll, pitch, heading error reduced from 0.54°, 0.38°, 1.45° to 0.18°, 0.17°, 0.16° respectively). The boresight correction essentially reduces the IMU uncertainties by a constant value. For example, a clear offset of the mean angular error towards zero is seen, however, the WGN and drifting bias remain unchanged (see Figure 4.10).

4.3.3 Correction in spectroradiometer footprint geolocation due to the lever-arm and boresight

For negligible lever-arm offsets and boresight angles, and the spectroradiometer pointing vertically down, the spectroradiometer footprint is expected directly at nadir below the GNSS antenna. However, in reality, the lever-arm offset, boresight angle, and the orientation of the IMU have a cumulative effect which, shifts the footprint geolocation of the spectroradiometer point observation away from nadir. For example, for our cross-

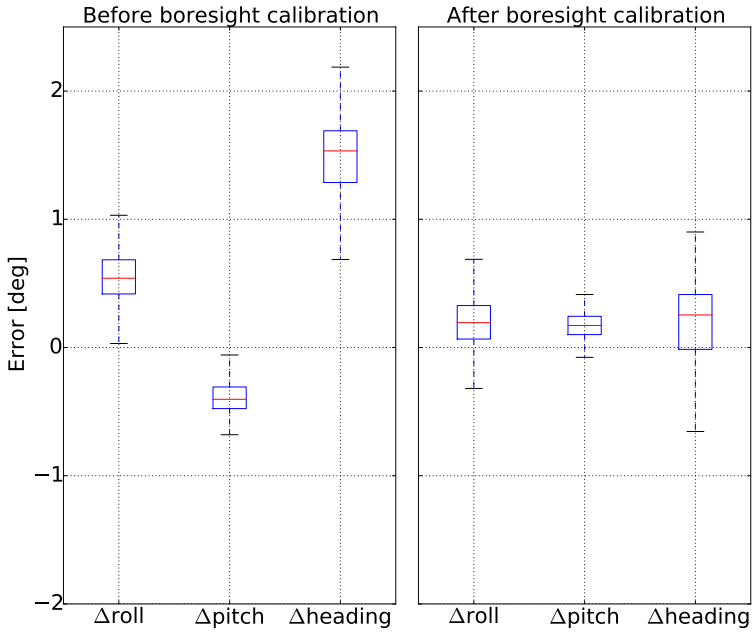

Figure 4.10: Error in IMU orientation before and after boresight correction, taking camera orientation (derived from Agisoft PhotoScan) as a reference.

grid pattern flight at 6.5–9.5 m AGL height, the shift in footprint due to the lever-arm offset was about 50 cm, the boresight angle had further shifted the footprint by about 25 cm, and the orientation of the spectroradiometer foreoptics resulted in a highest mean shift of about 80 cm (See Figure 4.11). Given the lever-arm offset, boresight angle, and the orientation of the spectroradiometer, these shifts can be accounted when determining the accurate footprint geolocation.

It should be remembered that, as the lever-arm offset and boresight angle are constant parameters, the shift in footprint due to these parameters is approximately constant in magnitude, while the direction of the shift is dependent on the orientation of the UAS spectroradiometer system at that moment. However, the shift in footprint due to the orientation of the IMU is more irregular in magnitude (see Figure 4.11 and Figure 4.12). This is due to the ever-changing orientation of the gimbal mounted IMU, which at times was found to be as high as 15°. Thus, the total spatial shift of the footprint on the ground from nadir for a typical flight, can easily reach to over 2 m.

4.3.4 Spectroradiometer footprint size

The size of spectroradiometer footprint was determined experimentally for each aperture (3°, 8°, 10°, 14°) at a working distance of 238 cm. This enabled computation of the FOV (see Table 4.3), which in turn allowed computation of footprint size as a function of AGL height. For instance, using an 8° aperture ring (7.16° FOV), the spectroradiometer

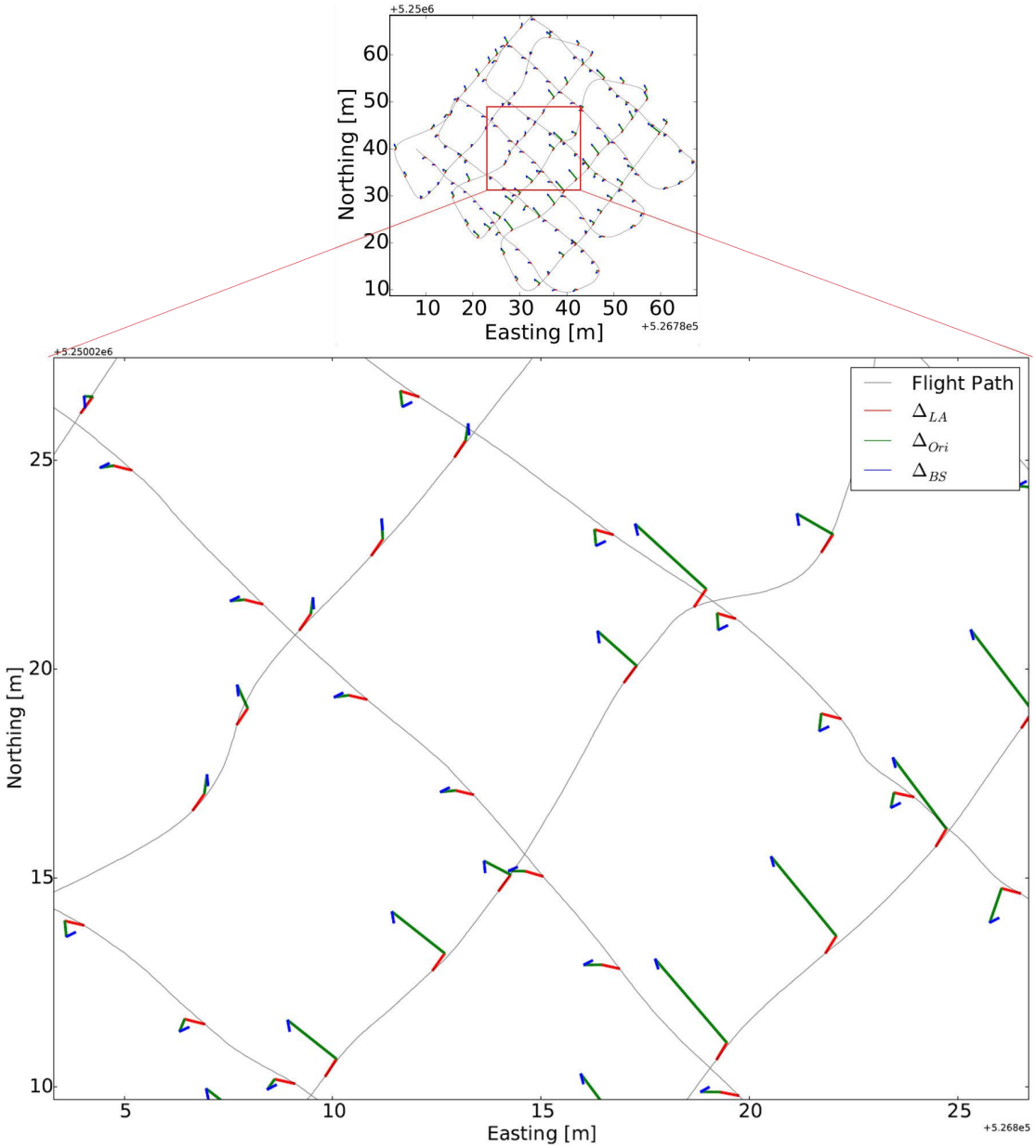

Figure 4.11: The cross-grid pattern flight of a UAS spectroradiometer system over a flat terrain at about 6.5–9.5 m AGL height. The shift in spectroradiometer footprint from nadir due to the lever-arm, boresight, and orientation of the spectroradiometer are represented by Δ_{LA}, Δ_{BS}, and Δ_{Ori} respectively.

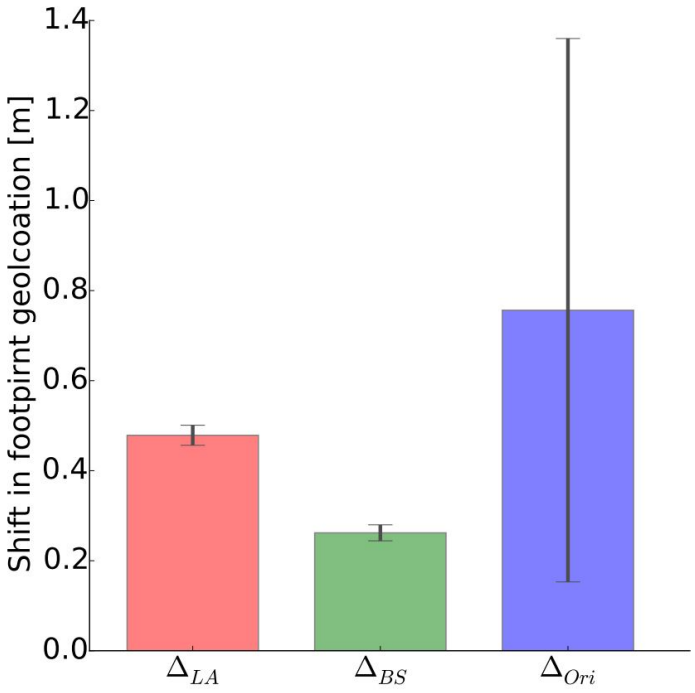

Figure 4.12: The magnitude of the shift in spectroradiometer footprint from nadir due to the lever-arm offset, boresight angle, and orientation of the spectroradiometer represented by the Δ_{LA}, Δ_{BS}, and Δ_{Ori} respectively with one standard deviation error bars.

Table 4.3: Spectroradiometer footprint size and FOV derived for different aperture rings at 238 cm working distance based on indoor experiments.

Aperture printed FOV	Footprint diameter (cm)	FOV
3°	11.4 ±2.1 cm	2.73° ±0.51°
8°	29.9 ±1.7 cm	7.16° ±0.40°
10°	36.9 ±1.0 cm	8.85° ±0.24°
14°	51.3 ±1.4 cm	12.16°±0.34°

footprint at an AGL height of 20 m is 250.4 cm diameter with ±8 cm uncertainty. The uncertainties related to the footprint size and the size of the FOV correspond to the DN tolerance described in section 4.2.4. A larger DN tolerance in proportion to the total signal triggers a larger buffer zone and a smaller footprint.

4.4 Discussion

The aim of this study was to correct the lever-arm offset and boresight angle, and determine the field of view of a point-measuring spectroradiometer mounted on a UAS. The primary motivation for this work was the necessity to know the footprint geolocation with high accuracy, which in turn requires a high accuracy estimation of the spectroradiometer's pose at the moment of spectral acquisition. We detailed experi-

mental methods and data processing workflow to perform the lever-arm and boresight correction, and FOV size determination for the UAS-mounted spectroradiometer used in this study. This correction in lever-arm and boresight and determination of FOV offers the ability of high accuracy footprint determination.

Our platform required two IMUs (one on the airframe and another on the gimbal) due to the inclusion of a levelling gimbal that stabilised the motion of the spectroradiometer's Gershun tube and primary IMU. The IMU mounted on the airframe and the lever-arm $L1^G$ were used to compute the corrected gimbal centre position. Furthermore, the gimbal-mounted IMU and the lever-arm $L2^G$ were used to compute the corrected position of the SRP. For applications that do not use a gimbal, only one IMU is required to account for both sensor orientation determination and lever-arm correction. Although not ideal, if a gimballed UAS does not have a frame mounted IMU (e.g. similar to our setup but without IMU on the airframe), it is best to correct the lever-arm using the heading angle alone, which in our study estimated the camera position with an accuracy of 4–9 cm. The use of two IMUs improved camera position accuracy to 3–8 cm, which is a relatively minor improvement given the increased sensor integration and processing requirements. This is due to the fact that the IMU in the gimbal only accounted for a smaller length of the lever-arm (length $L2^G$ 6.5 cm) in comparison to the IMU on the airframe (length $L1^G$ 81.5 cm). The benefit of the IMU on the gimbal is not so evident in lever-arm correction (due to smaller offset e.g. length $L2^G$ 6.5 cm) but on footprint geolocation determination with larger distances (e.g 10 m AGL height). So, it is beneficial to use the superior option of two IMUs in the gimbal.

The coordinate frame of the IMU on the gimbal (G) and the IMU on the airframe (B) were visually aligned and any further misalignment between them was neglected in this study. Consequently, lever-arm $L1^G$ and orientation of the IMU on the airframe were measured in a different coordinate frame (G, and B respectively). Any misalignment between the two coordinate frames, therefore, potentially introduces error in the lever-arm correction of the $L1^G$ component. In our study, we do not see the advantage in pursuing this misalignment for two reasons. Firstly, the IMU on the airframe was much noisier ($\pm 1.5^\circ$ 90% exceedance error) in comparison to the achievable boresight angle determination accuracy. Thus, a high accuracy misalignment determination does not offer similar benefit in the position accuracy of the SRP. Secondly, in the determination of the spectroradiometer footprint, the minor misalignment of the IMU on the airframe has a trivial effect on the total footprint uncertainty (see Chapter 3). However, for an application that is focused more on sensor pose rather than the footprint, this misalignment between two IMUs may be important.

The proposed stationary boresight experiments have two key advantages as compared to the in-flight or dynamic experiments. First, the influence of UAS dynamics and rotor vibration on the determined boresight angles value is avoided. Second, the effect of WGN and slow-moving drift on the boresight value is mitigated by averaging the orientations for a period of 1 min. This averaging period (6000 epoch at 100 Hz) is long enough to mitigate the WGN and at the same time is a sufficiently short period for the IMU not to be influenced by temporal drift. Additionally, since the pointing angle estimate is determined using the data retrieved directly from each sensor, the constant bias or internal misalignment in the sensor is incorporated within the estimated boresight angle. However, the additional boresight angle and lever-arm offset induced from the dynamic effect associated with the vibration and rigidity of the sensor mount are not captured in the proposed static experiments.

The error in the size of the spectroradiometer footprint is highly dependent on the error in the FOVs for each aperture, which further depends on the opening of the aperture rings and the distance of the aperture rings from the fibre optic end. Even very small discrepancies in placement and opening size of the aperture leads to a large change in FOV, which can further lead to larger variations in footprint size. For example, when operating sensors at a working distance of 10 m, a 1 mm discrepancy in placement and size of aperture leads to footprint variation of approximately 3 cm, and 21 cm respectively. Thus, it is recommended to experimentally determine the FOV for each aperture to compute the footprint as a function of AGL height as opposed to computation using the provided FOV value.

For a 10 m AGL height, the combination of lever-arm offset and boresight angle contribution to a footprint uncertainty was approximately 60–80 cm. After the correction of the lever-arm and boresight, their contribution in total footprint uncertainty (about 10–15 cm) reduced to 5–9 cm (Gautam et al. 2018). This level of accuracy is crucial for specific applications of a point-measuring spectroradiometer when operating at realistic flying heights on a UAS. For example, to determine the footprint geolocation to study chlorophyll fluorescence of an avocado orchard (canopy diameter of a single tree crown is about 2–3 m), it is important to be confident that the footprint of the spectroradiometer is within the envelope of a crown, otherwise spectral mixing with the background signal will occur.

The constructed UAS spectroradiometer system included a machine vision camera in the gimbal payload along with the IMU and the spectroradiometer Gershun tube. The camera was initially included to improve the in-flight sensor pose estimates and enable

image-based geolocation determination of the spectroradiometer observation. However, it was realised during boresight experiments that inclusion of the camera was crucial. The proposed spectroradiometer boresight experiments could not be performed outdoors due to the influence of ambient light. The experiments rely on the DN value recorded by the spectroradiometer to define the footprint boundary, thus, it is crucial to have a constant ambient light such as laboratory conditions for the duration of the experiment. However, the GNSS/IMU performed best outdoors in an unobstructed view of the GNSS constellation. The camera was thus used to connect the boresight angle estimate between the IMU and the spectroradiometer.

Although the spectroradiometer boresight experiments were performed indoors with a constant source of light, the sensitivity of the spectroradiometer makes it vulnerable to changes in lighting conditions. Such changes may be caused by fluctuation in voltage of the light source, and ambient light among others. Furthermore, we found that for an AGL height of 305 cm, the footprint location was biased by 2–4 cm towards the light source. We tackled the light field homogeneity issue by repetition of the experiment and repositioning of the light source at four equidistant locations radially away from the panel. For an unbiased estimate of the boresight angle, it is recommended to use a large diffuse illumination or multiple light sources radially distributed around the target panel to closely replicate Lambertian reflectance from the panel surface.

The experimentally computed FOV was found to be smaller than the FOV printed on the aperture rings (Table 4.3). Reasons for this could be a combination of a) smaller size of the aperture opening (in sub-millimetre range), b) a larger distance from the SRP to the aperture ring position (in mm range) c) the tolerance in spectroradiometer DN value set to estimate the boundary of the footprint, d) centre weighted response of the spectroradiometer FOV (analogues to satellite sensor point spread function), and/or e) low radiance from the footprint during experiments. It should be noted that even negligible discrepancy in size of the machined aperture and its relative vertical placement can result in a significant difference in footprint size. The measured FOV was found circular in our case, potentially due to the use of Gershun tube. However, this may not be the case for other applications where the FOV may be non-uniform in shape and affected by the orientation of the input slit as well (Mac Arthur et al. 2012).

Attitude and position are both crucial and complementary parameters for spectroradiometer footprint geolocation and thus corrections for the lever-arm and boresight are essential in the application of this technology on a UAS. After lever-arm and boresight correction, the dominant error source of the footprint geolocation is the uncertainty as-

sociated with the IMU placed on the gimbal. With boresight and lever-arm accounted for, the footprint is expected to be geolocated with an accuracy of 10–15 cm for 10 m AGL height (In review: Error propagation manuscript). This can further be improved, if necessary, by adopting machine vision and/or data fusion technique to better estimate the pose of the SRP. Future work will involve applying the lever-arm and boresight correction over a test field to determine in-flight footprint geolocation of the spectroradiometer.

4.5 Conclusions

In this study, we presented an experimental workflow for the correction of the lever-arm and boresight, and field of view determination of a spectroradiometer mounted on a UAS. Lever-arm correction required measurement of the lever-arm offset from the GNSS antenna phase centre to the spectroradiometer reference point. This was achieved by creating a scaled 3D point cloud of the UAS spectroradiometer setup using photogrammetric techniques. Boresight misalignment between the spectroradiometer, the IMU and the camera were determined by computing the pointing angle of each sensor when stationary. The FOV value of the spectroradiometer was estimated from a series of experiments designed to measure the footprint size yield from a known AGL height. This enabled, for a fixed FOV, computation of spectroradiometer footprint size as a function of AGL height. The lever-arm and boresight correction parameters were applied on a flight dataset for validation purposes. Correction of lever-arm enabled high accuracy position (3–8 cm with mean 6.3 cm and σ 2.5 cm) and orientation (error due to boresight contribution lower than $\pm 0.22^{\circ}$) estimation of the spectroradiometer reference point. With lever-arm and boresight corrected, the dominant error source of the spectroradiometer footprint geolocation is now the uncertainty associated with the IMU on the gimbal. With the increasing accuracy of small form factor IMUs and miniaturisation of spectroradiometers, we anticipate a growth in demand for UAS-mounted point-measuring spectroradiometers for geospatial applications. This is where the lever-arm and boresight correction is going to be crucial for high-accuracy geospatial positioning and subsequent interpretation of the spectral signal.

4.6 Thesis Context

This chapter calibrated the lever-arm offset and boresight angle, and determined the FOV of the spectroradiometer nadir channel. The lever-arm offset and boresight angle calibration helped to determine the footprint geolocation with increased accuracy. Similarly, the FOV angle enabled accurate characterisation of the footprint shape and

extent. Inflight lever-arm and boresight calibration were verified with the camera pose derived from SfM algorithm as a reference. This chapter systematically prepares the UAS-spectroradiometer system for scientific data collection and testing of the footprint. The next chapter uses the lever-arm and boresight calibrated pose along with the DSM to compute the footprint.

5 | Footprint determination of a spectroradiometer mounted on an unmanned aircraft system

Chapter 5 characterises in detail the footprint of the spectroradiometer mounted on a UAS. The work comprising this chapter is prepared for submission to *IEEE Transactions on Geoscience and Remote Sensing*. Section 5.5.4 is part of co-author Juliane Bendig's work under preperation for publication in *IEEE Transactions on Geoscience and Remote Sensing*.

Abstract

Non-imaging spectroradiometers on unmanned aircraft systems (UAS) are gaining interest for remote sensing applications that require high resolution spectral data over relatively large areas. In addition, UAS-mounted spectroradiometers offer a unique opportunity to retrieve solar-induced chlorophyll fluorescence (SIF), which in the context of the European Space Agency's upcoming Fluorescence Explorer (FLEX) satellite mission allows for upscaling and validation of the FLEX SIF signal. However, accurate georeferencing and determination of the footprint extent of the UAS sensor is essential to unravel the origin and spatial distribution of acquired SIF within the satellite pixel. In this study, we characterise the footprint of a non-imaging spectroradiometer (Ocean Optics QE Pro) mounted on a UAS with a novel algorithm based on a ray-casting technique. The algorithm takes the spectroradiometer's positon and orientation, and a topography model as an input to determine the footprint. Orientation is measured using an inertial measurement unit (IMU) after correction of boresight misalignments. The position is determined using an on-board global navigation satellite system (GNSS) receiver, after post-processing and correction of lever-arm offsets. The combined effect of position and orientation is incorporated in the footprint calculation together with actual spectroradiometer integration time and terrain configuration, i.e. slope and aspect. Footprint geolocation is validated by applying the georeferencing algorithm on isolated pixels of the machine vision images. The geolocation of the pixels are taken as a proxy for the spectroradiometer footprint and compared with surveyed ground control points. Quality of spectral signatures acquired with the UAS-based spectroradiometer was verified by comparing UAS and ground-measured reflectance responses for various natural targets. Finally, a SIF map with accurate georeferencing of the SIF signal is presented.

This study made progress towards interpretation and validation of the UAS-based SIF signal by accurate georeferencing of the SIF measurements.

5.1 Introduction

In recent years, a growing number of studies have developed, evaluated, and applied non-imaging spectroradiometers on-board unmanned aircraft systems (UAS) for earth observation (Pajares 2015; Aasen et al. 2018). A spectroradiometer samples observations at very high spectral resolution. This spectral signal measured from a UAS has the potential to replace traditional on-ground collection of spectral signatures as well as efficiently sample a relatively large area (e.g. 1 m^2–10 Km^2). Moreover, narrow-band spectral observations (<1 nm band width) present the ability to retrieve crucial vegetation quantitative products such as solar induced chlorophyll fluorescence (SIF) (Rossini et al. 2016; Wieneke et al. 2016), to directly monitor the photosynthetic activity of plants (Wyber et al. 2017; Verrelst et al. 2016; Pinto et al. 2016). This ability, combined with the spatial flexibility offered by a UAS platform, makes a UAS-mounted spectroradiometer a tool for spectral upscaling to (Liu et al. 2017), and validation of, airborne- and satellite-based observations. Examples include validation of the future European Space Agency's Fluorescence Explorer (FLEX) satellite mission (Moreno et al. 2015; Moreno et al. 2016; Drusch et al. 2016; Kraft et al. 2017), and the airborne HyPlant sensor (Rascher et al. 2015). However, there has been no research into accurate georeferencing and characterisation of the spectral footprint on the ground. There is a strong need for footprint characterisation of UAS-based spectroradiometers to know how the objects on the ground contribute to the spectral signal.

The ground/vegetation extent measured by the spectroradiometer for the duration of the integration time is here referred to as footprint. The geographic coordinate of the footprint centre location is referred to as geolocation. The geolocation and the extent are required for a complete characterisation of the footprint in a geographic coordinate frame. In this study, the footprint computed for an epoch of global navigation satellite system (GNSS)/inertial measurement unit (IMU) time is defined as an instantaneous footprint. It is a circular projection of the spectroradiometer's FOV from the flying height onto the topography (Zeng et al. 2017; Natesan et al. 2018; Garzonio et al. 2017). The footprint, thus, is an integration of instantaneous footprints computed throughout the spectroradiometer integration time.

Computing the footprint of the UAS-mounted spectroradiometer is a challenging task for the sensor is passive and non-imaging. Hence, the existing georeferencing meth-

ods typically used for imaging and/or active UAS-based sensors (e.g. cameras, LiDAR, imaging spectrometer (Wallace et al. 2012; Turner et al. 2014a; Chiang et al. 2012a; Lucieer et al. 2014)) are not directly applicable for following reasons. Firstly, the array of spatially contiguous pixels such as in camera images and imaging spectrometer strips is not available. Secondly, the distance to the target (such as in a LiDAR) is not known. As a result, the footprint computation, unlike for other UAS-mounted sensors, cannot be based on a) tie-point relation between subsequent footprints, b) inter-pixel spatial relation within a single footprint, and c) distance measurement from the sensor to the target being measured. Thus the UAS-mounted spectroradiometer requires a unique workflow to georeference its observations. The footprint georeferencing problem is analogous to the footprint yield from an isolated pixel of a camera or a single strike of a LiDAR but without range measurement. Consequently, for the spectroradiometer we rely on the position and orientation (pose) and the topography of the ground/vegetation for footprint computation (Aasen et al. 2018).

Thus, the prerequisites for footprint computation are the spectroradiometer position and orientation, the ground/canopy model, the FOV, and the integration time. In this study, a global navigation satellite system (GNSS) receiver records the position, while the IMU records the orientation for each spectral acquisition. The GNSS position requires correction of the offset, from the receiver to the spectroradiometer, called lever-arm offset. The orientation requires the correction of angular misalignment, between the IMU and the spectroradiometer, called the boresight angle. The ground/canopy model, in the form of digital surface model (DSM), can be derived using overlapping aerial photos and surveyed ground control points (GCPs) (Mancini et al. 2013; Remondino et al. 2011). The spectroradiometer FOV, can be estimated by computing the size of the footprint in a controlled experiment for a known height. The spectroradiometer integration time depends on irradiance levels and dictates the achievable signal-to-noise ratio (SNR) of the acquired radiance measurement.

With the spectroradiometer pose and topography model, techniques from computer graphics and computational geometry, such as ray-casting can be adapted to compute the footprint. Ray-casting technique uses ray-surface information to solve the problem of determining the first point of intersection between ray and surface (Roth 1982; Glassner 1989; Hanrahan 1983; Adamson and Alexa 2003). For the UAS mounted spectroradiometer, ray-casting enables computing the footprint by intersecting the spectroradiometer pointing direction with spatial reference (as a ray) and the topography (as a surface). The footprint extent may then be deduced based on the FOV, distance to the target being measured, speed of the UAS, pointing angle and the integration time

of the spectroradiometer.

The aim of this paper is to characterise the geolocation and extent of the footprint of a non-imaging spectroradiometer mounted on a UAS. We propose a direct-georeferencing algorithm based on a ray-casting approach that uses the spectroradiometer pose along with the DSM to compute the footprint geolocation and extent. We demonstrate the application of our algorithm at a study site with a mildly undulating terrain containing distinct natural targets. The geolocation accuracy of the footprint is validated by applying the algorithm to isolated pixels of the co-mounted camera and comparing its position with surveyed GCPs. The spectral signal of the UAS-based spectroradiometer is validated by comparing the acquired target-specific reflectance factor with the ground-measured reflectance factor taken as reference. Finally, a SIF map is produced with accurate spectral footprints based on direct georeferencing of the spectral signal.

5.2 The scientific sensor payload

5.2.1 The sensors and platform

A multirotor UAS (DJI Matrice 600 Dà-Jiāng Innovations Science and Technology Co., Ltd., China) is used as UAS platform for this study. The UAS sensor payload capacity is about 6 kg, and resulting flight time about 12 mins. Three sensor mounts are used on the UAS: the antenna boom placed on top of the airframe, the spectroradiometer/computer compartment below the airframe, and the gimbal underneath (see Figure 5.1).

The antenna boom contains two dual-frequency GNSS antennae (Antcom G5Ant-1.9A4-XTB-1, Torrance, California), a MEMS-based IMU (Lord MicroStrain 3DM-GX3-35, Vermont, USA), and the upward-looking irradiance channel of the spectroradiometer. The spectroradiometer (Ocean Optics QE Pro FL, Florida, USA), its shutter controllers, and the on-board computer are placed in the spectroradiometer/computer compartment. The gimbal contains a MEMS-based IMU (Advanced Navigation Spatial Dual, Sydney, Australia), a monochrome camera (FLIR Grasshopper GS3-U3-23S6M-C, British Colombia, Canada), and the downward-looking vegetation channel of the spectroradiometer.

5.2.2 Sensor geometry

The spectroradiometer has a bifurcated fibre optic cable with two optical pathways: the irradiance and the vegetation channel. The vegetation channel records the upwelling radiance (reflected and emitted), whereas the irradiance channel measures the downwelling solar irradiance (direct and diffuse). A Gershun tube is attached to the end

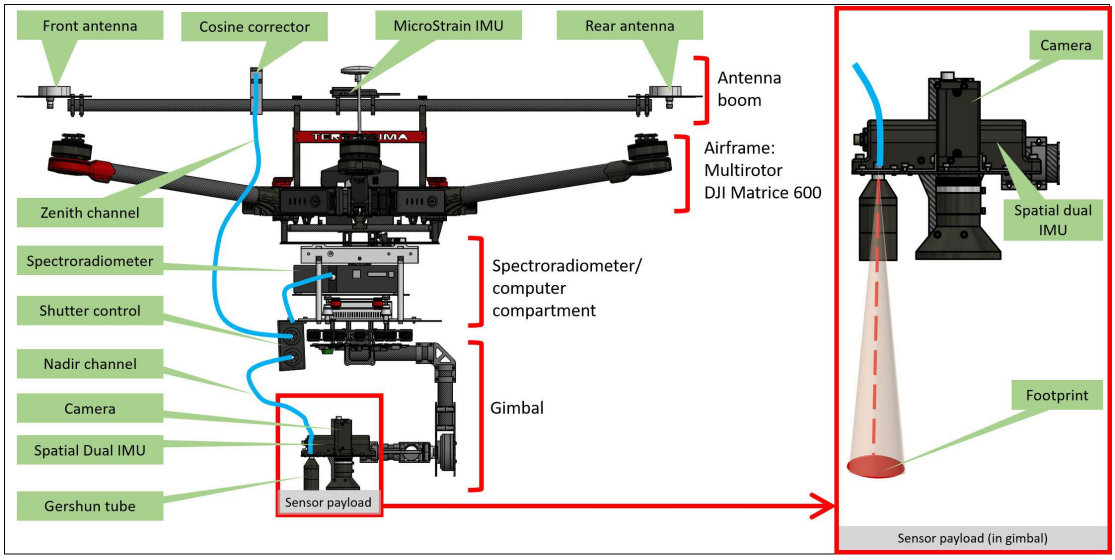

Figure 5.1: The UAS spectroradiometer system used in this study to investigate the geolocation of the footprint.

of the vegetation channel to restrict the FOV of the fibre optic cable. The irradiance channel is equipped with a cosine corrector to collect solar irradiance from 180° FOV. Two electronic shutters (Ocean Optics, INLINE-TTL-S) are used to regulate individual measurements from the bifurcated fibre optic cable: upwelling radiance, dark current, and downwelling solar irradiance.

The two GNSS antennae on the antenna boom are mounted at a distance of 1.04 m. The MicroStrain IMU, placed approximately in between the two antennae, is used to determine the roll and pitch angle of the antenna boom and the cosine corrector. The Spatial Dual IMU, mounted alongside with the with the spectroradiometer vegetation channel, is used to determine the orientation of the spectroradiometer. The alignment of the two antennae, from rear to front, is fixed with the mounting direction of the on-board IMUs and the camera. This fixed heading alignment enables the dual antenna assisted high accuracy heading to be used as the heading of all the sensors on board. The sensors mounted on the antenna boom and the sensor mounted on the gimbal are fixed in their heading alignment, however, detached in their roll and pitch angle. This loosely coupled configuration of GNSS and IMU is adopted to accommodate the gimbal. The gimbal serves three purposes: 1) provides a stabilised mount and sustain a near-nadir view of the spectroradiometer, 2) minimises the elongation in footprint, which occurs due to higher roll and pitch angles, and 3) reduces the impact of rotor-induced vibration and pose uncertainty associated with it. The gimbal carries the vegetation channel, the camera, and the IMU, however, the GNSS antennae require clear sky view, hence the mounting position of the antennae is above the airframe.

5.2.3 Sensor synchronisation

To compute a spatially accurate footprint, the data acquisition of each sensor (the spectroradiometer, the GNSS, and the IMUs) require accurate time synchronisation. The Spatial Dual IMU, camera, and the spectroradiometer are synchronised using hardware triggered pulses. For each data acquisition, the spectroradiometer and the camera transmit a synchronisation pulse, which is timestamped in the Spatial Dual IMU log file using GNSS time. The MicroStrain IMU/GNSS records orientation measurements in GNSS time, which enables time-matching with the Spatial Dual IMU log (see Figure 5.2).

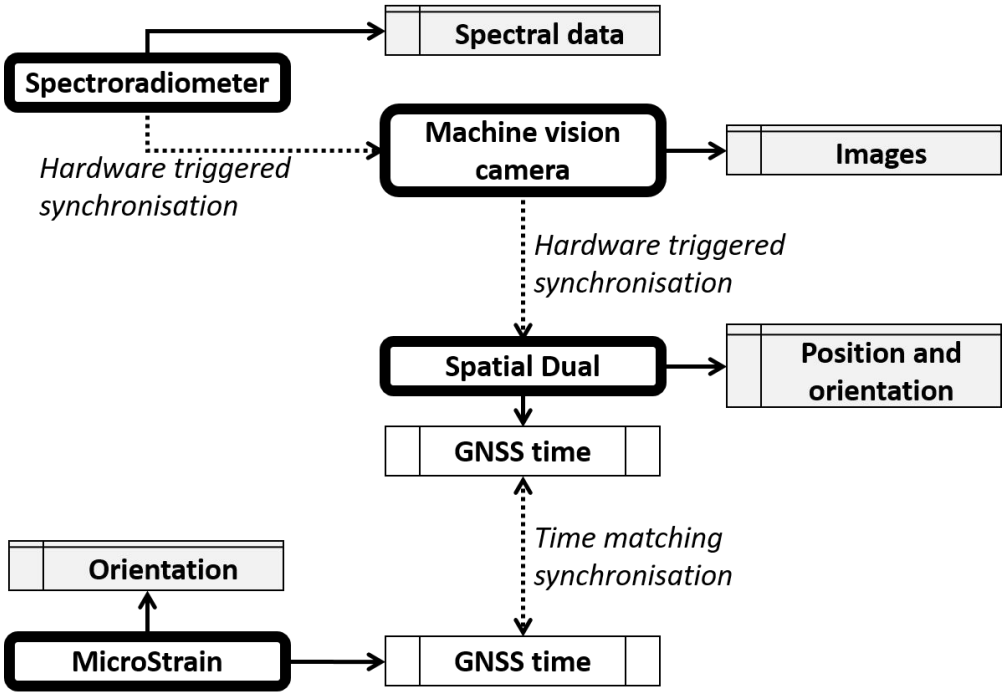

Figure 5.2: Synchronisation between the on-board sensors using hardware triggered synchronisation strobe and GNSS time matching.

5.3 Experimental setup

5.3.1 Test site

The University farm (42°47′44.37″S, 147°25′36.72″E) in Cambridge, Tasmania, Australia was used for this study. Two flight were performed at two plots within the test site. The first experiment focuses on the footprint geolocation of the UAS-based spectroradiometer. The second experiment demonstrates the georeferencing of UAS-retrieved SIF. A Leica 1200 GNSS base station was setup at a close baseline (within 100 m). An additional Leica 1200 rover was used to survey the GCPs and location of ground validation spectra within the study site.

The first plot had a complex terrain with mildly undulating height and distinct natural targets. The targets included water, grasses (button, sedge, short green), and dirt road. The targets had relatively distinct borders and were adequately sized (over 2×2 m) for UAS spectroradiometry from 10 m flying height with expected footprint size about 1.5 m. The second plot had slopy terrain with grazed and flowering alfalfa and dry grassland paddocks where a distinct variation in the SIF was expected.

5.3.2 The experiment

The two experiments were conducted at noon (local time), on 6^{th} February and 7^{th} March 2018. A DJI Phantom 4 Pro UAS with an in-built camera was used to acquire RGB imagery, and produce an orthophoto and DSM of the test site. Images were captured with 90% forward and 60% side overlap. Although the on-board monochrome camera fully satisfies the requirements of footprint computation, we also acquired RGB images with a DJI Phantom UAS to create an orthophoto map of the study area in natural colours for presentation purposes.

The February experiment consisted of the spectroradiometer payload flight in a cross-grid pattern at a height of about 10 m and flying speed of 3 m/s acquired in two consecutive flights. A white reference spectralon panel measurement was taken before take-off and after landing.

The March experiment consisted of four flight lines of the spectroradiometer payload at 10 m height, and two of the flight lines repeated at 20 m flying height. During flight, measurements of downwelling irradiance were recorded through the spectroradiometer's cosine-corrected channel at an interval of 30 s.

After the flight, each spectral reference target was sampled on the ground using the QE Pro from approximately 1 m height (0.14 m diameter footprint).

During the flight, the spectroradiometer was set to acquire spectral readings once every second with an integration time of 0.85 s and FOV of 8°, with additional dark current readings every 30 s. The reference spectralon panel was measured before the take-off and after landing. The irradiance channel was not used during this experiment due to technical reasons. The Spatial Dual GNSS receiver recorded the position at 20 HZ, the IMUs (Spatial Dual and MicroStrain) recorded orientation at 100 HZ, and the camera captured two images synchronous to each spectroradiometer observation: one at the start and another at the end of the integration time (see Figure 5.3).

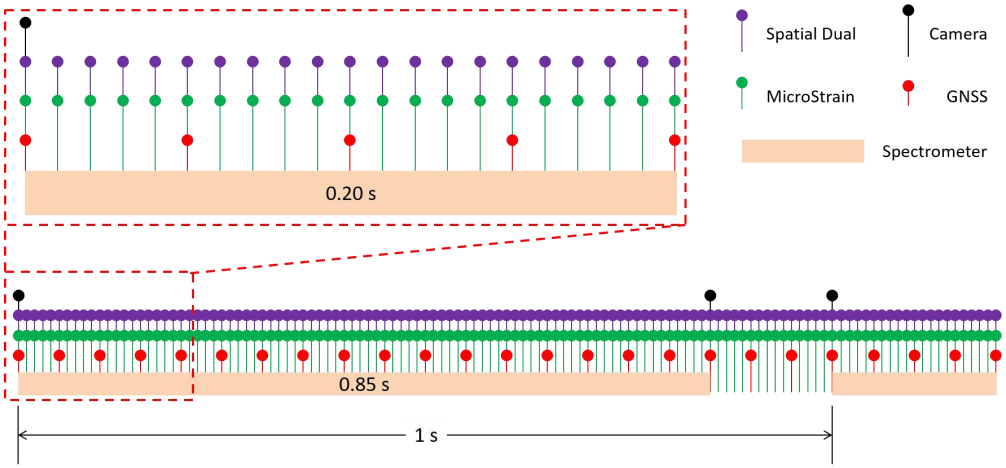

Figure 5.3: The data capture rate of multiple sensors on-board the UAS spectroradiometer system. One spectral data acquisition duration spans over 85 readings of the IMU, 17 readings of the GNSS, and two captures of images.

5.4 Methodology

5.4.1 Calibration and pre-processing

The sensors used in this study required multiple calibrations such as the radiometric and spectral calibration of the spectroradiometer, geometric calibration of the footprint, and distortion calibration of the co-mounted camera. Furthermore, pre-processing of the data is required such as processing of the GNSS data, and processing of aerial photos to compute the DSM.

Spectroradiometer spectral and radiometric calibration

The spectral and radiometric calibration are essential steps to process the spectroradiometer data (Slater 1985; Thenkabail and Lyon 2016). Through the spectral calibration, the spectroradiometer's centre wavelength and bandwidth at the full width half maximum (FWHM) of each band's spectral response function are determined.

The radiometric calibration converts energy of photons recorded in digital numbers (DN) to spectral radiance with physical units. Subsequently, *In situ* measurements during flight were used to compute the reflectance factor as a ratio of the radiant flux reflected by the target and by the 100% reflectance reference panel (i.e., Spectralon), see Equation 5.1 (Miura and Huete 2009; Schaepman-Strub et al. 2006).

$$R_T = \frac{DN_T - DN_O}{DN_R - DN_O} R_f \tag{5.1}$$

where, R_T a is the reflectance factor of the target. DN_T, DN_O, and DN_R are the raw DN value measurement of the target, dark current, and reference panel respectively. R_f is the reflectance factor of the reference panel, which is assumed to be Lambertian. The reference panel measurements recorded before the take-off and after landing were used to compute a mean spectral reference for all measurements taken during the flight (Slater 1985; Schaepman-Strub et al. 2006).

Lever-arm and boresight calibration

Spectroradiometer footprint geometry (geolocation and extent) required calibration of the lever-arm offset and boresight angle and determination of the FOV angle (Chiang et al. 2012a; Chiang et al. 2015; Daakir et al. 2016; Turner et al. 2017). Calibration of the lever-arm corrects for the shift in the geolocation of footprint induced due to the offset between primary GNSS antenna (located at the front) and the spectroradiometer. The boresight angle calibration further corrects the footprint geolocation through better estimation of the spectroradiometer's pointing direction. The determination of the FOV enables accurate computation of the footprint size as a function of the FOV and AGL height.

The position measured by the front GNSS antenna receiver was post-processed with reference to the base station using RTKLIB, an open source GNSS processing software package (Takasu and Yasuda 2009). To correct for the lever-arm, the offset between the front antenna and the spectroradiometer reference point (SRP) was determined in the Spatial Dual coordinate frame (G). The offset was measured in AutoCAD software (Autodesk AutoCAD 2016) using a scaled 3D point cloud of the UAS spectroradiometer system. The 3D point cloud was created from overlapping photos of the airframe and control points processed with the structure-from-motion (SfM) algorithm in Agisoft PhotoScan (Professional version 1.3.0). The front GNSS antenna position was corrected for lever-arm offset as presented in Equation 5.2 to compute the position of the spectroradiometer reference point (SRP).

$$SRP^W = A1^W + \mathbf{R}_B^W \times L1^B + \mathbf{R}_G^W \times L2^G \tag{5.2}$$

where $A1^W$ is the position of the front GNSS antenna in geographic coordinate frame W, attitude matrix $\mathbf{R}_B^W$ represents the orientation of the MicroStrain IMU, and $\mathbf{R}_G^W$ represents the orientation of the Spatial Dual IMU on the gimbal. $L1^B$, and $L2^G$ are the lever-arm offsets from the front antenna phase centre to the centre of gimbal, and from the centre of the gimbal to the SRP respectively.

To calibrate the boresight angle, the angular misalignment between the IMU, the camera and the spectroradiometer was required. These misalignments were estimated by computing the difference in pointing angles of each sensor, determined independently using controlled and stationary experiments. The pointing angles of the sensors were obtained using independent techniques: the IMU by averaging the orientation, the camera by using SfM, and the spectroradiometer by moving a spectrally distinct target into the FOV for the stationary experiments. Two boresight angles were determined using the stationary experiments: first between the IMU and the camera; and second between the camera and the spectroradiometer. The boresight angle between the IMU and camera was used to compute the orientation of the camera in the spatial validation step. Coupling the two boresights, the boresight between the IMU and the spectroradiometer was computed, which was required to determine the orientation of the spectroradiometer ($\mathbf{R}^{W}_{Spec}$) as presented in Equation 5.3.

$$\mathbf{R}^{W}_{Spec} = \mathbf{R}^{G}_{b} \times \mathbf{R}^{W}_{G} \tag{5.3}$$

where, $\mathbf{R}^{G}_{b}$ is the rotation matrix parametrised using the boresight angle between the Spatial Dual IMU and the spectroradiometer Gershun tube. Attitude matrix $\mathbf{R}^{W}_{G}$ represents the orientation of the Spatial Dual IMU. The detailed workflows for determination of the lever-arm offset and boresight angle specific to the UAS-mounted spectroradiometer used in this study are outlined in Chapter 4.

To determine the accurate FOV of the spectroradiometer, the footprint size was measured for a known distance. The size of the footprint was estimated by moving a spectrally distinct target onto the FOV of the spectroradiometer. The footprint size, determined for a known distance, enabled computation of the FOV, which allows computation of the footprint size as a function of flying height.

Camera calibration and topography model of the study area

Camera lens calibration enables extraction of 3D metric information from the images by adjusting the camera intrinsic parameters (Balletti et al. 2014). An accurate lens calibration was crucial for the spatial validation of the spectroradiometer, which isolates a pixel from an image to compute the correct ground location of the pixel. The computation relies on precise intrinsic as well as extrinsic parameters, thus demanding a dedicated calibration of the lens distortions. For the calibration, images of a checkerboard calibration panel were captured from different angles and distances (with the same lens settings, i.e. focus and aperture, as for UAS flight conditions). The images were

processed in Agisoft Lens software (Version 0.4.2) to estimate the lens geometric characteristics, which included the focal length, principal point, and the radial and tangential distortion parameters of the lens.

Additionally, the shutter speed of the fixed aperture camera needed optimisation. Camera shutter speeds were tested for different ambient light conditions (e.g. sunny, clear, partly cloudy, cloudy, and overcast sky condition) to estimate a suitable shutter speed for each condition. During flight experiments, the optimised shutter speed for the given sky condition was fed into the custom developed python application before image acquisition.

The aerial images captured using the DJI Phantom 4 Pro flight and the surveyed GCPs were processed in Agisoft PhotoScan (Professional version 1.3.0) to produce the orthomosaic and topography model. The topography model was represented by a triangle mesh, and exported from Agisoft PhotoScan in STL format.

5.4.2 Footprint computation

Here we determine the spectroradiometer footprint geolocation and extent (shape and size) expressed in a geographic coordinate frame based on a ray-casting approach. The algorithm takes spectroradiometer position, orientation, FOV, integration time, and the DSM as an input to compute the footprint (see Figure 5.4) and incorporates the effect of terrain and footprint elongation.

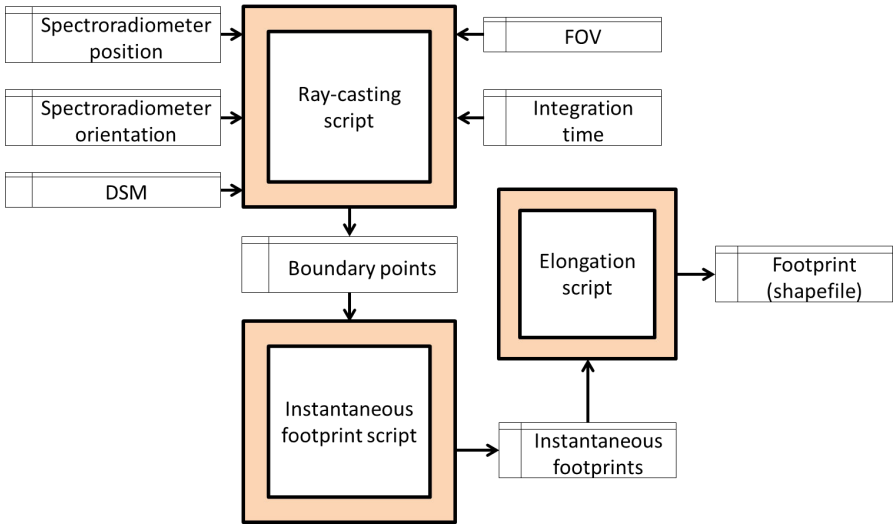

Figure 5.4: The data processing workflow to determine the geolocation, shape, and size of the spectroradiometer footprint, using lever-arm corrected position, boresight corrected orientation, DSM, FOV, and integration time.

Geolocation of the spectroradiometer footprint centre

The lever-arm offset corrected position and boresight angle corrected orientation were used to compute the instantaneous footprint geolocation. Let $\hat{agl}$ be a unit vector pointing vertically down from the SRP position to nadir. The unit vector when rotated using boresight corrected orientation $\mathbf{R}^{W}_{Spec}$ yields a unit vector $i\hat{F}P$, which is aligned with the spectroradiometer optical axis (see Equation 5.4).

$$i\hat{F}P = \mathbf{R}^{W}_{Spec} \times \hat{agl} \tag{5.4}$$

The vector $i\hat{F}P$ when positioned at the SRP essentially points to the direction of the instantaneous footprint and intersects with the topography surface when extended. The problem of the ray-surface intersection was solved using a ray-casting algorithm (Roth 1982; Glassner 1989; Hanrahan 1983; Adamson and Alexa 2003), which computes the point of intersection between a ray and a surface. In our case, the ray can be an $i\hat{F}P$ vector vector and the surface can be a topography model, both expressed in a geographic coordinate system. Using the above inputs, the ray-casting algorithm computes the point of intersection, which is the geolocation of the spectroradiometer footprint in a given geographic coordinate system.

Extent of footprint

Extent computation of the instantaneous footprint requires the spectroradiometer FOV, in addition to the pose, and the DSM. The FOV was determined from indoor experiments by measuring the footprint size yield for a known height (Chapter 4). Thus, the determined FOV allowed the computation of the instantaneous footprint size as a function of height above topography.

For a single GNSS/IMU epoch during spectral acquisition, 36 points on the edge of the circular FOV were generated at an angular interval of 10°. To generate these points, a vector orthogonal to the $i\hat{F}P$ was rotated about the $i\hat{F}P$ axis at an increment of 10° using Rodrigues rotation (Dai 2015; Belongie 2018). This stepwise rotation resulted in 36 points, which were used to construct 36 vectors, all originating from the spectroradiometer fibre optic end. The 36 vectors when geolocated using the ray-casting algorithm resulted in 36 boundary points over the topography. Collectively, the 36 boundary points represent the boundary of the instantaneous footprint (see Figure 5.5). These points connected together formed the instantaneous footprint polygon, which is irregular in shape and size subject to spectroradiometer pointing angle and the slope of the topography at each of the 36 boundary points.

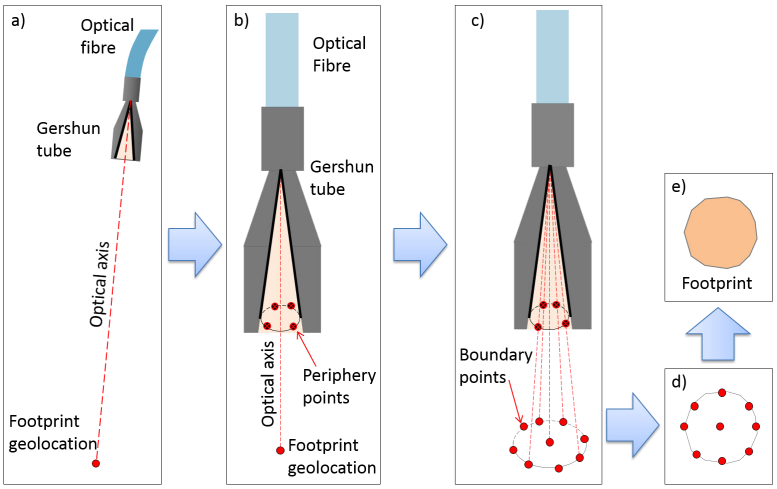

Figure 5.5: The workflow to determine the extent (shape and size) of the spectroradiometer instantaneous footprint in a geographic coordinate frame: a) instantaneous footprint geolocation is computed using ray-casting algorithm; b) 36 periphery points (only four shown) are selected on the circumference of the spectroradiometer FOV using Rodriguez rotation; c) the edge points are geolocated using ray-casting algorithm to populate the 36 boundary points (only eight shown) on the topography; d) the boundary points, when connected, form a closed polygon, which e) represents the shape, size, and geolocation of the footprint in geographic coordinate frame.

Elongation of the footprint

The computed footprint geolocation, shape, and size were only valid for a single epoch of GNSS/IMU observation (≈10 ms duration). However, the spectroradiometer required a longer integration time (typically about 1000 ms) to acquire a more reliable spectral signal. Combined with the flying speed of the UAS (typically 3–5 m/s), the longer integration time results in elongation of the footprint. This elongation is collectively represented by multiple instantaneous footprints computed throughout the integration time of the spectroradiometer. The elongated footprint is analogues to dragging or smearing of the instantaneous footprint over the topography along the flight direction for the duration of integration time. The footprint is generally elongated in the along-track direction, which is a function of spectroradiometer integration time and UAS flying speed. However, there is the added effect of roll and pitch angles on the extent and direction of the elongation, which yields a complex elongation in both along-track and across-track direction. For our test dataset involving the spectroradiometer integration time of 850 ms, 85 instantaneous footprints, determined independent of each other, were combined to yield an elongated footprint (see Figure 5.6).

5.4.3 Footprint validation

Validation of the footprint geolocation was achieved by applying the ray-casting technique of georeferencing on the co-mounted camera. Spectral validation of the UAS-based

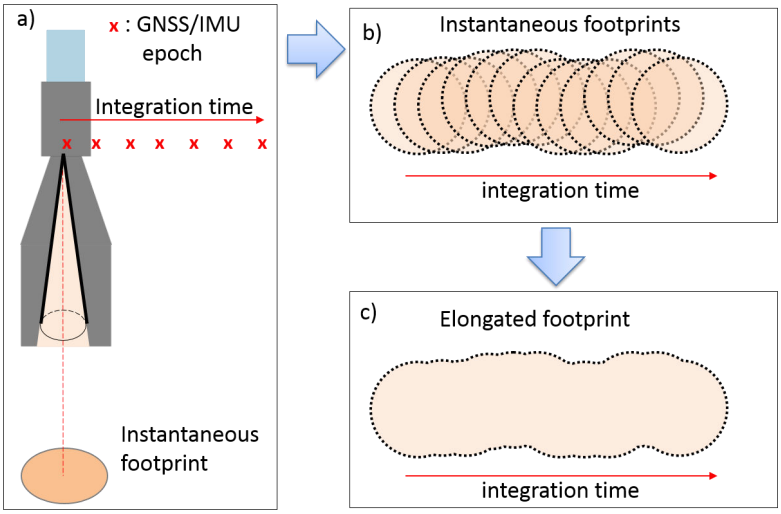

Figure 5.6: The workflow to determine elongated footprint during the spectroradiometer integration time: a) the instantaneous footprint is computed for each of the position/orientation epoch throughout the spectroradiometer integration time to yield b) multiple instantaneous footprints, which when merged together produce c) the elongated footprint of the spectroradiometer observation.

measurement was achieved by comparing with the ground measured reflectance factor.

Validation of footprint geolocation

The footprint geolocation has multiple sources of uncertainty originating from the GNSS, IMU, calibration, and distance to target. To validate the spectroradiometer footprint geolocation, we apply a ray-casting algorithm to isolated a pixel of the co-mounted camera (see Figure 5.7). The surveyed GCPs captured in the aerial images were used as checkpoints in this assessment to validate the footprint geolocation of the spectroradiometer. This indirect method of validation was justified because the same technique of georeferencing (ray-casting) was used for the spectroradiometer and the isolated pixel of the image. Thus, the uncertainty in geolocation of the isolated pixel is expected to be a close approximation of the uncertainty in the computed footprint geolocation of the spectroradiometer.

First, the images from the co-mounted camera were corrected for lens distortion. The pixel representing the centre of the surveyed GCP targets, referred to as GCP-pixel, is isolated from the aerial images. Only the clearly visible GCP-pixel within the centre part of the image (restricted to a central area of 300-pixel radius of the principal point) is isolated for assessment. The pointing angle of the GCP-pixel was computed using the boresight angle corrected orientation of the camera and the FOV of the camera pixel array. The position of the GCP-pixel was determined by applying the lever-arm

correction from the front GNSS antenna to the camera. The pose of the GCP-pixel is used to compute its geolocation using the technique outlined in Section 5.4.2. The computed geolocation of the GCP-pixel is then compared with the surveyed location of the GCP taken as a reference.

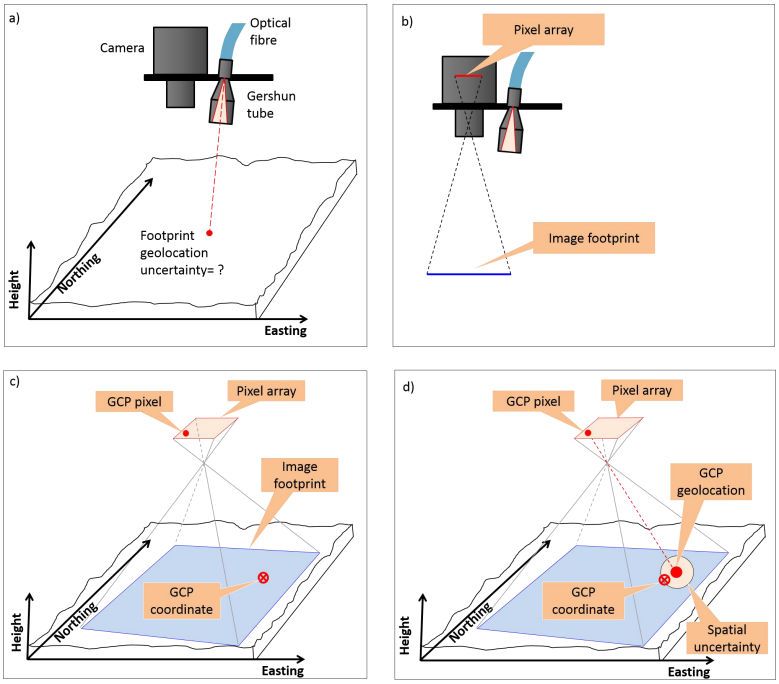

Figure 5.7: Method of footprint geolocation validation using a) a co-mounted camera as a proxy; b), c) a pixel in camera array containing surveyed GCP is isolated; d) ray-casting algorithm is applied to the isolated pixel to compute its geolocation, and compared with the surveyed GCP coordinate to estimate the achievable accuracy.

Validation of UAS-based reflectance factor

Ground sampled spectral measurements of the natural targets were used to validate the UAS-based spectral measurements. For each of the natural targets (sized about 3×3 m), ground reference measurements were taken using a random sampling method within the boundary of each target. About nine measurements were taken using the QE Pro spectroradiometer with 8° degrees FOV from an above-canopy height of 1 m. A dark current and a white reference Spectralon measurements were taken before moving on to next target. The ground- and the UAS-measured spectra were converted to the relative reflectance factor. The UAS-measured reflectance factors of individual targets within the footprint geolocations were retrieved and compared with the ground-based reflectance of the same targets.

5.5 Results

5.5.1 The footprint

A total of 705 footprint observations were made during the cross-grid pattern flight. Each individual 'blob' in Figure 5.8 represents a single observation. The observations at times come from a single target e.g. water, button grass, sedge grass, short green grass, or dirt road. However, mostly, the observed spectral response has multiple sources. This level of detailed information about the footprint is only possible with accurate footprint information. Thus, the combination of footprint location/extent and ancillary information, may assist in interpretation of the acquired spectral response. The ancillary information can be the information of constituent targets within a single footprint.

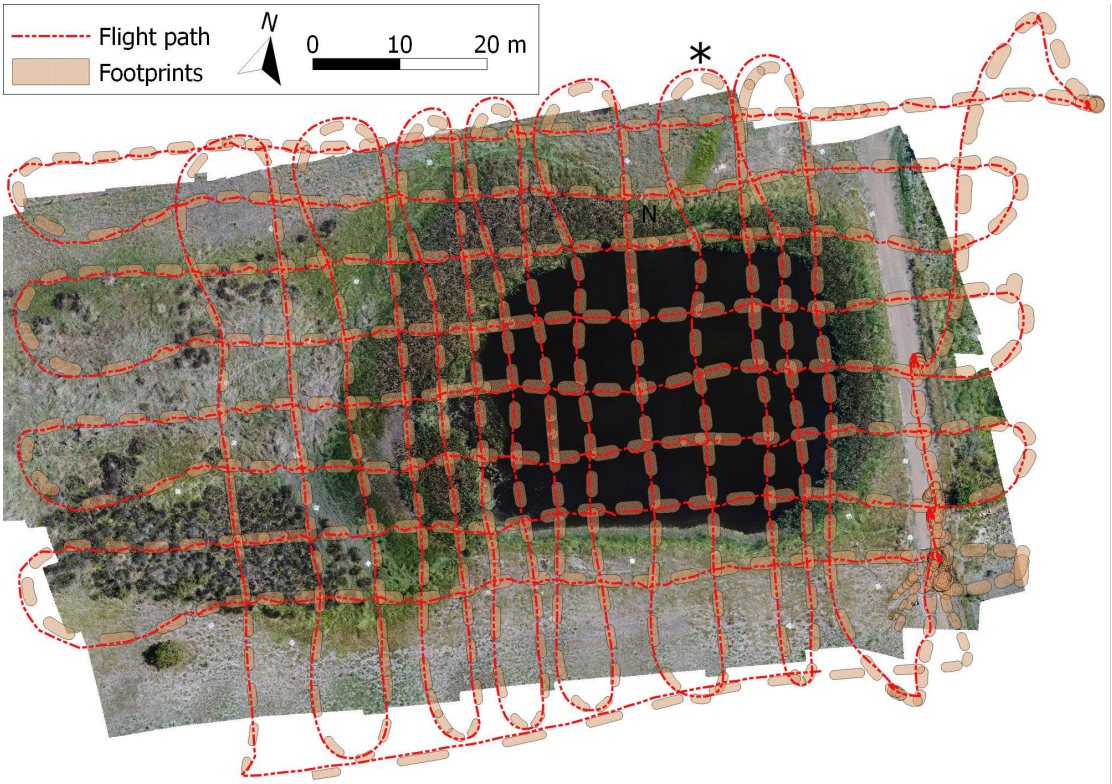

Figure 5.8: The footprint of the spectroradiometer observation taking into account its integration time, and terrain model. Note the base station is marked as $*$. Note the overlayed orthophoto mosaic was obtained for a visual presentation purpose from a separate UAS flight.

The footprints have varied shapes and sizes, subject to the combined effect from the spectroradiometer's FOV, integration time, flying speed, flying direction, roll and pitch angles, AGL height, and terrain. The footprint shape of the spectroradiometer is described as two semicircles connected with a rectangle (see Figure 5.9 a, b, c) . The elongation is a function of spectroradiometer integration time and UAS flying speed. The added complexity in the footprint is evident when the UAS is changing direction,

and when the roll/pitch angles are changing rapidly (see Figure 5.9 d, e, f). Furthermore, for a higher flying height, the footprint becomes larger and is less elongated (see Figure 5.9 c).

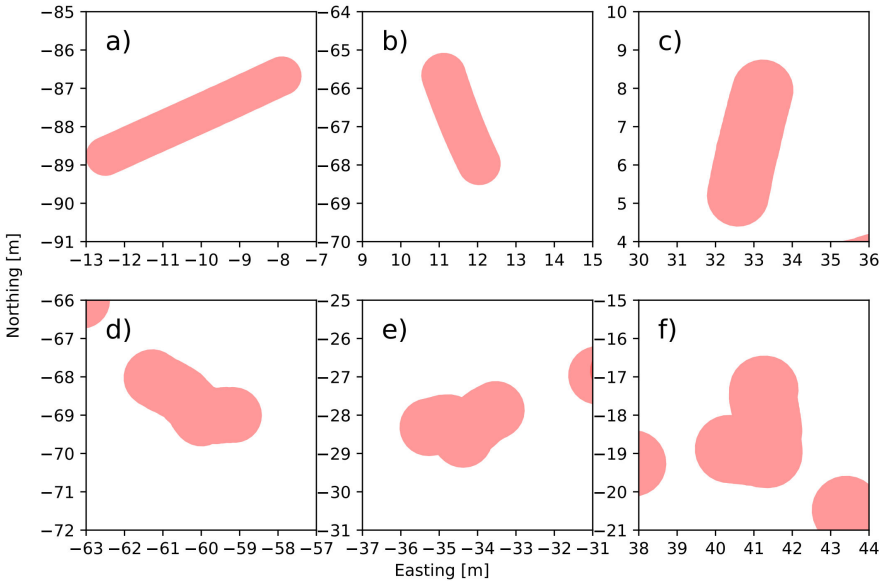

Figure 5.9: Some detailed examples of the spectroradiometer footprint for 8° FOV, 0.85 s integration time, ≈ 10 m AGL flying height, ≈ 3 m/s flying speed . The easting and northing coordinate are with reference to the base station operating within 100 m baseline. Note the variability in shape and size of the footprint.

5.5.2 Geolocation validation

A total of 135 GCP-pixels selected from 135 images of the co-mounted camera were used for the spectroradiometer geolocation validation. The difference in geolocation of the GCP-pixels when compared with the surveyed location of the GCPs was found to be ±15 cm 1σ (see Figure 5.10). This error in geolocation increased steadily with the distance of the GCP-pixel from the centre of the image, which corresponds to the distortion characteristics of the camera lens. The achieved geolocation accuracy of ±15 cm 1σ is consistent with the accuracy estimated by the error propagation model of the spectroradiometer footprint (see Chapter 3).

5.5.3 Validation of the UAS-acquired reflectance factor

Using the computed footprint, the UAS-acquired reflectance factor of each target is retrieved and compared with the ground-based reflectance factor of the same target. Median of spectral reflectance factors was used for comparison to avoid the influence of spectral outliers originating, among others, from pathes of dead scenescent grass leaves or larger stones on the dirt road having significantly different reflectance signatures. The comparison showed a reflectance RMSE of 0.007 for short green grass, 0.008 for button

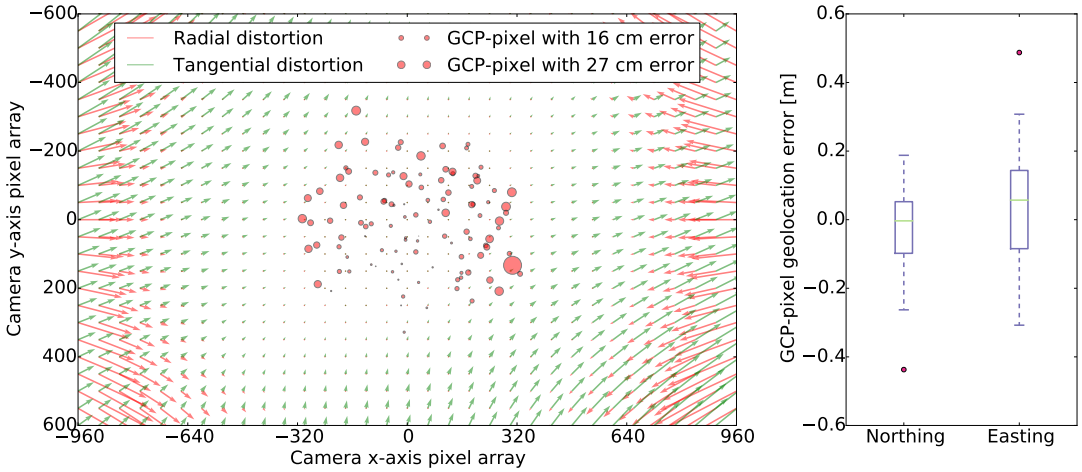

Figure 5.10: a) Selection of GCP-pixel from the camera pixel array (b) to compute footprint geolocation error of the GCP-pixel when compared with the surveyed GCP. Note the size of GCP-pixel location corresponds to the geolocation error.

grass, 0.010 for dirt road, and 0.014 for sedge grass (see Figure 5.11).

Figure 5.11 shows that the ground-based measurement had higher variability in reflectance factor as compared to the UAS-based reflectance factor. This high variability was associated with the total area on the ground that was being sampled using the two methods. The ground sampling measured a very small area at a time due to the low measurement height above the target (i.e. spectral footprint area was 0.02 m^2 for a sampling height of 1 m). Thus, the spectral data captured specific features within the target. For example, for the sedge grass, the ground sample can contain a healthy leaf, or an angled leaf, or an unhealthy leaf etc. Whereas UAS-based reflectance factor with a footprint area of about 5.0 m^2), always contains signal from multiple features within the target. Furthermore, despite maintaining similar observation angle, for the ground and aerial sensors, the anisotropic reflectance of the target is expected to affect in some degree the acquired spectrum.

The presented RMSE in spectral reflectance factor is a measure of the overall error for entire spectral bands from wavelength 500 nm to 850 nm. This RMSE may not appropriately represent each section of the spectral region. The absolute RMSE for NIR bands is likely to be larger due to the higher reflectance in the NIR region, however, relatively it might be smaller than the red and blue regions. Thus, we compute the relative RMSE (RRMSE) (Verrelst et al. 2014), defined by the absolute RMSE divided by the mean reflectance factor for four wavelength sections: green, red, red edge, and NIR (see Table 5.1). The relative surface reflectance varied by approximately 5%–7% in the Green region, 4%–6% in the Red region, 2%–7% around the red edge, and 3%–6%

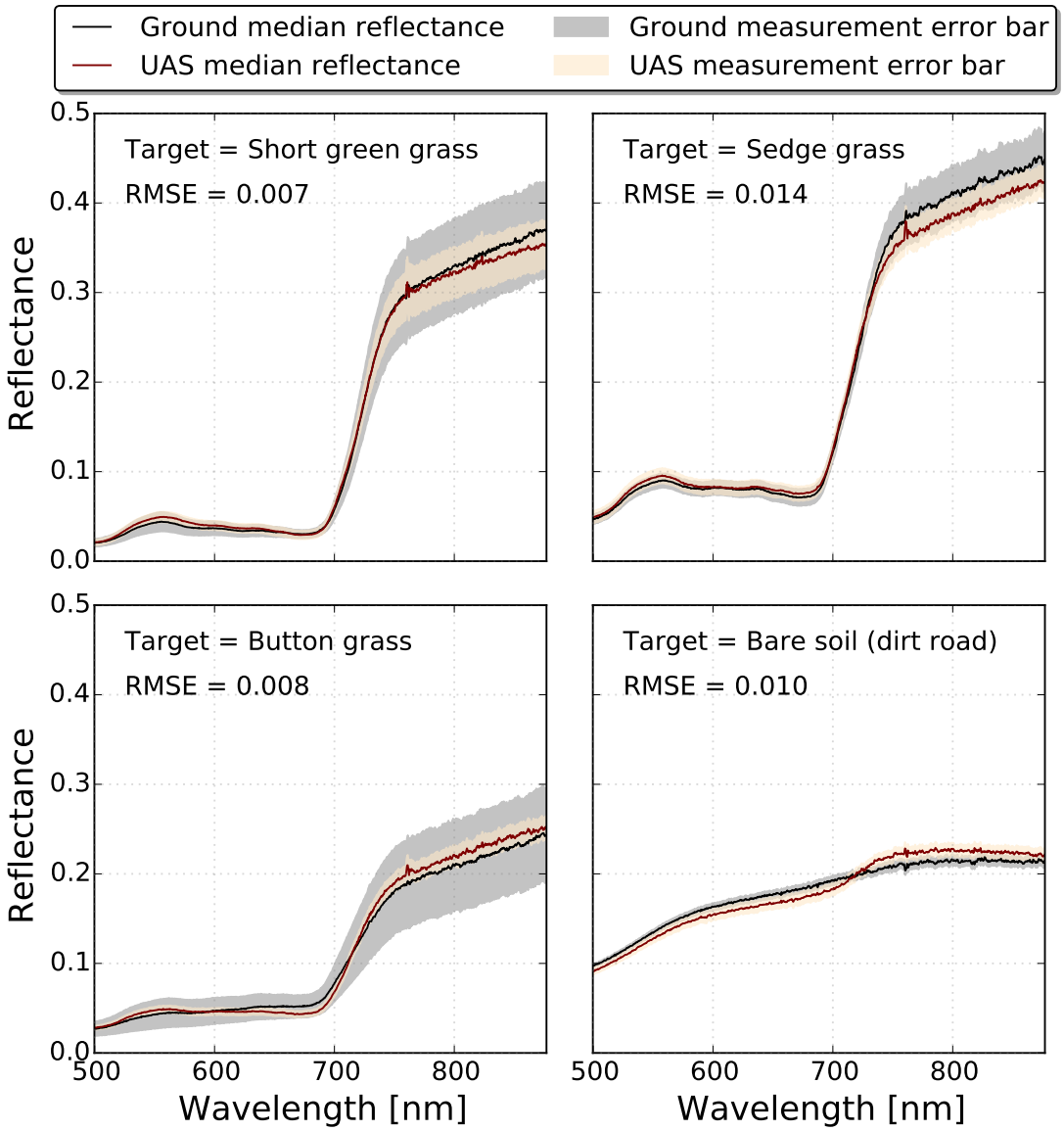

Figure 5.11: Comparing the UAS-based and ground-based median reflectance of four different natural targets present within the study site. The error bar around the reflectance curve represents the standard deviation of the measured reflectance.

in the NIR. Short green grass and button grass had a higher RRMSE in green (11%) and the red (13%) region respectively.

Table 5.1: Relative RMSE of the UAS-based reflectance factor in reference to the ground-based reflectance factor.

Spectral region	Green	Red	Rededge	NIR
Wavelength [nm]	500–600	600–690	690–750	750–850
Short green Grass	0.110	0.057	0.019	0.025
Sedge Grass	0.049	0.039	0.039	0.058
Button Grass	0.071	0.137	0.068	0.051
Road	0.058	0.059	0.042	0.052

5.5.4 A demonstration of SIF retrieval for the UAS-mounted spectroradiometer

To demonstrate the system's capability of measuring canopy SIF, we include key results from the case study conducted under clear sky conditions 07 March 2018. Both spectroradiometer channels were cross-calibrated with a spectralon panel before and after the flight. Data was processed to radiance as described above (Section 5.4.1) and SIF was calculated using the iFLD method (Alonso et al. 2008) by means of two R packages FieldSpectroscopyCC/DP (Julitta 2018a; Julitta 2018b). The final footprints of the spectroradiometer are displayed in Figure 5.12 and colour coded by SIF values between 0.01 and 2.9 $mWm^{-2}nm^{-1}sr^{-1}$. Flowering alfalfa shows the highest SIF values. It is followed by a more heterogeneous pattern of grazed alfalfa and low values over dry grassland. In the orthophoto, one can notice a more intensively grazed area in the southern part of the grazed alfalfa (marked by 'a)' in Figure 5.12) and a greener area in the northern part of the grassland (marked by 'b)' in Figure 5.12). These differences are clearly reflected in the acquired SIF measurements of these areas.

5.6 Discussion

The aim of this study was to characterise the footprint (geolocation and extent) of a non-imaging spectroradiometer mounted on an unmanned aircraft system. The main motivation of this study was the need to understand the spatial distribution of the SIF signal within a single pixel of the upcoming FLEX satellite mission. We presented a ray-casting algorithm to determine the footprint geolocation and extent. The effect of terrain slope, spectroradiometer pointing angle, and spectroradiometer integration time were included in the footprint computation. Surveyed GCPs on the ground and ground reference reflectance factor were used to validate the footprint geolocation and the UAS-retrieved reflectance.

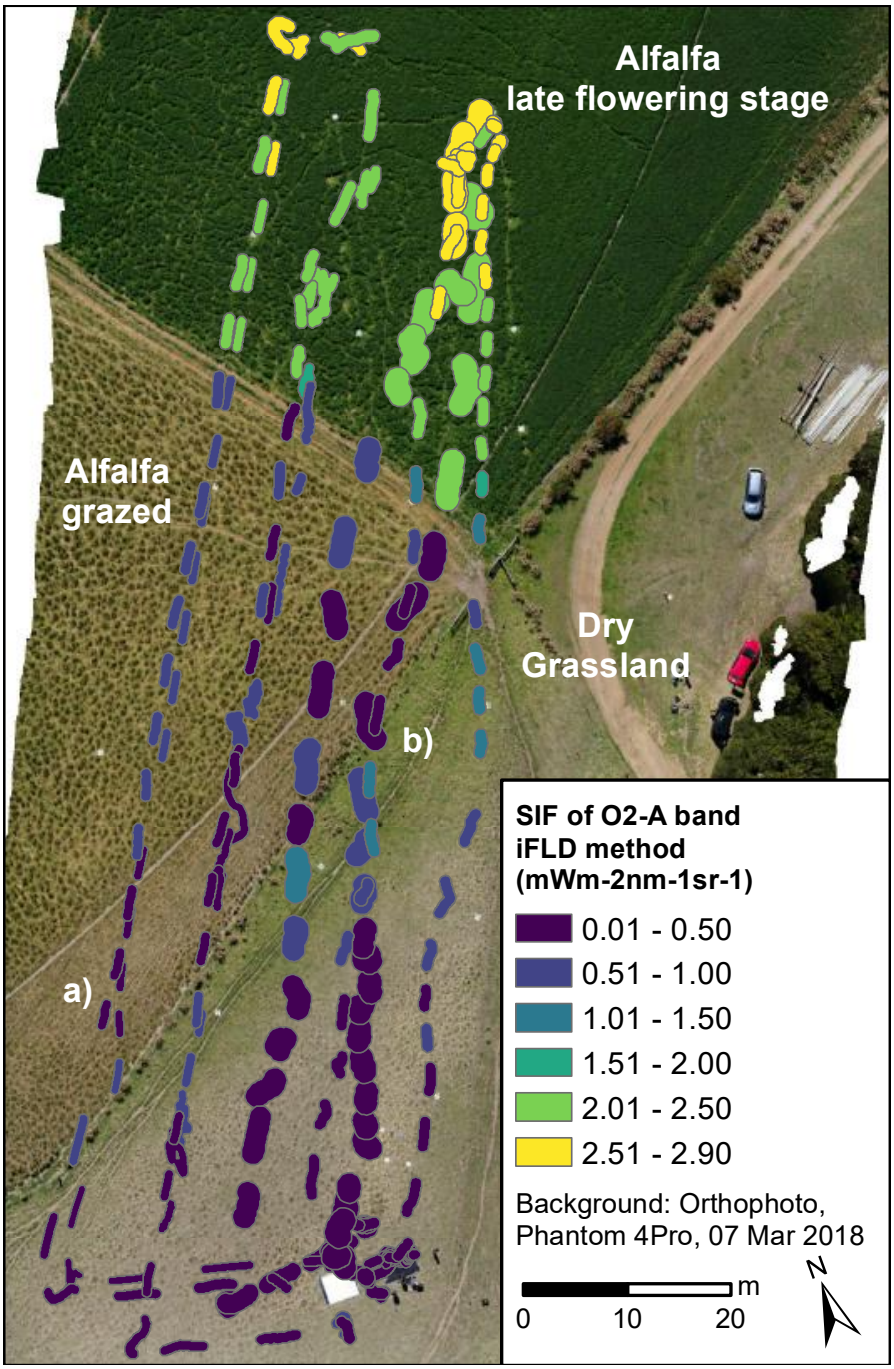

Figure 5.12: SIF acquired from UAS spectroradiometer over alfalfa and grassland in 07 March 2018 at noon local time in Cambridge, Tasmania, Australia. The footprint size is according to flying heights of 10 and 20 m. Background orthophoto acquired with Phantom 4 Pro. Notation 'a)' and 'b)' are the intensively grazed alfalfa, and greener grassland respectively.

A novel achievement of this study is the spatially detailed footprint characterisation of the spectroradiometer, which is not well understood for UAS-based applications. Using the methodology presented, the footprint of the spectroradiometer observation can be computed with high spatial detail and accuracy ($\pm$15 cm 1σ for 10 m AGL height).

The mildly undulating topography over which the footprint computation was demonstrated may be considered a limitation of this study. Nonetheless, the effect of undulating topography on footprint is a combined result of topography slope and the spectroradiometer pointing angle. For instance, a combination of flat terrain and a $\pm20^\circ$ pointing angle of the spectroradiometer is equivalent to a nadir-looking setup over a terrain with $\pm20^\circ$ slope. In a test flight (not presented here), the footprint computation over a flat terrain but with high pointing angle (within $\pm20^\circ$) of the spectroradiometer corresponded with the study presented here. Thus, similar performance is expected for operations over a highly complex topography such as forest canopies.

Another limitation of this study lies in the spatial validation of the footprint uncertainty. The footprint geolocation was validated, indirectly, using the co-mounted camera and not directly using the spectroradiometer for four reasons. First, the spectroradiometer measurement is a non-imaging instrument, which made identification of reference GCPs infeasible. Second, it is infeasible to keep the spectroradiometer pointing at a small static spectral target for the duration of the integration time from a dynamic UAS platform. Third, the co-mounted camera experienced identical flight dynamics and vibrations, which can potentially affect the footprint computation in similar ways to the spectroradiometer. Fourth, after isolating a pixel from the camera pixel array, the footprint computation problem for the spectroradiometer and the isolated pixel is the same. Hence, the proposed method validates the accuracy of the ray-casting algorithm to directly georeference the spectroradiometer observation for the *in situ* operation.

The choice of the GCP-pixel, especially its distance from the principal point, affects the achievable accuracy in geolocation verification. For instance, using a GCP-pixel at the edge of an image degraded the achievable georeferencing accuracy (in the order of 150 cm 1σ). This degradation is caused by the radial and tangential distortion present in the camera lens. Even the lens distortion correction applied to the images left traces of distortion still evident on the pixel array towards the edges (georeferencing accuracy in the order of 50 cm 1σ). Thus, to perform an unbiased validation of the spectroradiometer footprint geolocation, we restricted GCP-pixels within 300-pixel radius of the principal point. This restriction was carefully determined after investigating the radial and tangential distortion parameters of the camera. After applying the restriction, the

georeferencing uncertainty was found to be 15 cm 1σ. This restriction is backed up with the fact that the spectroradiometer pointing angle ($\pm 5°$) during the flight was well within the 300-pixel radius region (equals to $\pm 13°$ pointing angle) of the captured images.

Different spectral sampling strategies can be adopted for a UAS-based spectroradiometer: i) hover and measure, and ii) measure while in motion (Mac Arthur et al. 2013). The hover and measure strategy results in a near-circular footprint as the UAS is hovering over the same location for the duration of signal integration. This method is recommended for acquiring a "clean" spectra, as the footprint elongation is minimal and results in reduced spectral mixing between adjacent surfaces. The flight can be planned such that the hover and measure strategy can be used to measure in transect or quadrat as per the user requirement. The measure during motion strategy results in elongation of the footprint due to the signal being integrated as the UAS platform moves. This method is useful for obtaining spectral signatures of larger and spatially homogeneous study areas. Footprint computation proposed in this study suffices the computational necessity of all the aforementioned spectral sampling strategies.

The spatially detailed footprint is crucial when studying small or heterogeneous targets. However, a simpler footprint form (assuming a circular footprint) may suffice the necessity of other applications, for example measurements over homogeneous grassland. However, it should be noted that for a typical moving platform, the circular footprint alone represents an inappropriate and inaccurate footprint. For instance, in our experiments, a typical instantaneous footprint area (about 1.5 m^2) increased by over three fold (about 5.0 m^2) when considering the elongation caused by the movement of the UAS platform. This knowledge of footprint extent is crucial with regard to interpretation of the acquired spectral signal and the target being measured.

Further investigations will focus on an alternative georeferencing method such as spatial co-registration using the co-mounted camera (e.g. (Turner et al. 2014c)). This method may enable footprint computation using the co-mounted camera alone thus making the payload significantly lighter (without GNSS and IMUs). In addition, the operational UAS spectroradiometer system will be used to investigate the retrieval of the SIF signal, and geospatial interpretation based on the footprint extent. With the recent interest in remote retrieval of SIF, the footprint characterisation complements and improves existing UAS spectroscopy practices.

5.7 Conclusions

In this study, we presented a novel algorithm based on a ray-casting approach to determine and characterise the footprint of a non-imaging spectroradiometer mounted on an unmanned aircraft system. The algorithm used lever-arm corrected position and boresight corrected orientation of the spectroradiometer together with the signal integration time and the terrain topography model (slopes) to georeferenced and compute the footprint shape. The footprint geolocation was validated by applying the ray-casting algorithm on an isolated pixel of a co-mounted camera. The resulting geolocation of the isolated pixel was compared with ground surveyed GCPs. The inferred accuracy of the spectroradiometer footprint geolocation was ± 15 cm 1σ. Verification of the spectral responses within the footprints was conducted through ground sampling. The ground sampled reflectance functions were compared with the UAS-acquired reflectance factor for various natural ground targets, resulting in RMSE between 0.007and 0.014 in visible and near infrared wavelengths. In final step, an ability to create a SIF map of crop canopies with accurate georeferencing of the signal was demonstrated. With an accurate characterisation of the footprint, UAS-based spectroscopy presents a powerful tool for interpretation and validation of the coarser resolution air- and space-borne spectroscopy observations, such as surface reflectance derived from Landsat or Sentinel, or SIF signal observed by the future ESA FLEX satellite mission. Finally, an accurate footprint will provide us with improved insights into the contribution of the structural composition of spectral targets.

5.8 Thesis Context

This chapter provided the final outcome of the thesis which is the footprint (geolocation, shape, and size) characterisation of a spectroradiometer mounted on a UAS. A novel algorithm to characterise the footprint is developed, tested and validated. This chapter advances the UAS-spectroradiometry by enabling the georeferencing of the spectroradiometer measurements. With the accurate geolocation, an increased number of application using the UAS-spectroradiometer system for geospatial application is expected.

6 | Discussion and conclusion

6.1 Addressing the goal

The general goal of this study was to determine the footprint of a non-imaging spectroradiometer mounted on a UAS. Fulfilling the goal included: a) identification of suitable GNSS and IMU sensors, b) rigorous modelling of the footprint geolocation error budget, c) calibration of the actual lever-arm offset and boresight angle, d) computation of the footprint, e) spatial validation of the footprint geolocation, and f) spectral validation of the acquired reflectance signature.

Identification of suitable GNSS and IMU sensors

Performance of small form factor MEMS-based IMU/GNSS sensors was compared against specific selection criteria. The most suitable sensor was determined by assessing the performance accuracy, size and weight, and synchronisation compatibility with the spectroradiometer. Since the Spatial Dual IMU/GNSS presented a high accuracy position and absolute heading, moderate accuracy in roll and pitch, and straightforward hardware triggered synchronisation, it was selected as the best purpose fitting sensor at the time of this study (2014 and 2015).

Error budget modelling and assessment of footprint uncertainty

An extensive assessment of the error budget sensitivity to the change in input uncertainties and flight operational parameters was performed. The error budget model, developed to assess the spatial uncertainty in geolocation of the footprint, propagated uncertainties associated with the selected sensors, their calibrations, and the determination of AGL height. The AGL flying height was found to be the major determinant of spatial uncertainty in footprint geolocation. When the flying height was fixed, the dominant source of uncertainty was the orientation estimation by the MEMS-based IMU.

Correction of the lever-arm offset and boresight angle

Indoor and outdoor stationary experiments were performed to identify the lever-arm offset and boresight angle. The identified lever-arm offset and boresight correction was successfully validated by comparing the pose correction applied to the in-flight dataset and the reference pose obtained via the photogrammetric processing chain. The

improvement of the footprint geolocation resulting from the lever-arm and boresight correction was demonstrated on a UAS flight dataset.

Computation and spatial/spectral validation of footprint

The calibrated position and orientation data, together with a DSM, were used in a ray-casting algorithm to compute the footprint of the spectroradiometer. The effect of UAS flying speed, the spectroradiometer integration time, terrain slope, and the spectroradiometer viewing angle was incorporated in the footprint computation. The footprint of spectroradiometer observation (for 0.85 s integration time) was characterised using 85×30 boundary points each computed independently using a ray-casting algorithm. Such a spatial detail is sufficient for characterisation of a spectroradiometer footprint over a complex terrain and/or plant canopy.

Spatial validation of the determined footprint geolocation was performed by applying the ray-casting algorithm to an isolated pixel of the co-mounted camera. The errors were quantified by comparing the geolocation of the isolated pixel and the surveyed location of corresponding ground control points. Spectral validation of the footprint was performed by comparing the reflectance acquired from the UAS with the reflectance measured on the ground, and computing the root mean square error (RMSE). RMSE calculated for nadir reflectance of multiple natural targets resulted in acceptable similarity of coincidental UAS and field measurements.

6.2 Limitations

Although the GNSS/IMU selected at the time of this study met the selection criteria, rapid advances in MEMS technology have resulted in the development of inertial sensors with better specifications and a lower weight. Consequently, newer IMU sensors with better manufacturer specifications may achieve a higher geolocation accuracy.

The error budget presented in this thesis was crucial for initial testing and making a realistic estimate of a footprint geocoding uncertainty (Chapter 3), however, it cannot replace a direct experimental verification. The spectroradiometer footprint geolocation accuracy was verified using the digital images taken by the co-mounted camera as the reference. Due to time and logistic constraints, a thorough spectral and radiometric verification of the non-imaging spectroradiometer footprint accuracy using *in situ* radiance data was not conducted and needs still to be done.

The influence of flight dynamics and rotor induced vibration on the geolocation accu-

racy is not fully understood. The introduced method in Chapter 3 incorporated the IMU/GNSS readings taken during a flight to model the GNSS and IMU error. A more complex solution would require the MEMS-based GNSS/IMU to be mounted and assessed against a higher grade GNSS/IMU, such as a NovAtel SPAN, during a data acquiring flight. This would provide a better understanding of the influence of flight dynamics and the rotor-induced vibration on the footprint geolocation accuracy.

Our validation of boresight estimation in Chapter 4 covered the boresight between the IMU and the camera and not the boresight component between camera and spectroradiometer. The validation of the boresight between the camera and the spectroradiometer was not pursued for two reasons. First, the validation requires the knowledge of the improvement in the spectroradiometer footprint location before and after the boresight angle correction. However, determination of the reference footprint location of the spectroradiometer during flight was unfeasible. Second, the boresight estimation experiment for the camera to spectroradiometer component was equally rigorous to the IMU to camera component. Thus, validation of IMU to camera component provided an indirect validation for the camera to spectroradiometer component. Moreover, results of the footprint determination over natural heterogeneous targets (see Chapter 5) resulting in spectral similarity between ground and UAS measurements supports the assumption that the boresight angles were determined with the required level of accuracy.

Although the advantage of the spatially detailed footprint characterisation is obvious, the actual benefit of its computation is not easily quantifiable. Such a quantification would require the crossover of footprint extents collected over multiple targets. This scenario is likely to happen when flying over heterogeneous targets. On the other hand, acquisitions over homogeneous targets do not benefit equally from the detailed footprint geometry, hence an approximation of footprint as being circular may be sufficient.

The proposed sensor setup and data processing workflow has still room for improvements. At this moment, the approach requires GNSS and IMU sensors for position and orientation determination and a camera to produce a DSM and orthophoto map before computation of the footprint. A potential streamlining of this procedure can be done by computing the footprint using a co-mounted digital camera alone (Turner et al. 2014b). A single camera can suffice to perform both tasks: a) creation of the DSM and orthomosaic, and b) computation of the footprint. However, it should be noted that the GNSS/IMU operate in higher frequency as compared to the camera. Consequently, the footprint computed using the GNSS/IMU contains more spatial detail than the camera computed footprint.

The structure of vegetation targets, combined with the solar and observational angles, the optical characteristics of adjacent targets and the size of the sensor FOV, influences amplitude of recorded vegetation reflectance factor. This anisotropic reflectance behaviour is characterized by the bidirectional reflectance distribution function (BRDF) (Burkart et al. 2015; Weyermann et al. 2014). Although our experimental setup uses a gimbal, to maintain a constant observation angle, a certain level of the BRDF effect is expected to influence our reflectance readings, especially in cases of larger FOV (Tu et al. 2018). Similarly, the solar zenith angle, coupled with the UAS flight dynamic motions, is known to affect the irradiance measurement and subsequently the reflectance computation (Bendig et al. 2018). Additionally, the presence of spectrally bright objects adjacent to the observed area influences the recorded spectrum. Photons scattered and reflected by the adjacent object can be added to the reflectance signal of a target investigated through a wide FOV. Some level of influence could also originate from an occasional shadowing of the UAS airframe on the measured target. To achieve a high-quality spectrum that is required for solar-induced chlorophyll fluorescence (SIF) retrieval, it is important to provide an appropriate consideration to the aforementioned factors.

Spatial resolution and extent of remote sensing observations is an important issue to interpret the spectrum as well as SIF, as different sensors (e.g. proximal, UAS, satellite) operate at a different distance from the target. A footprint of a proximal sensor can be set to record spectrum of small-size Earth objects, whereas a space-borne image pixel of somewhat larger size usually contains a mixed spectrum of several, spectrally different, objects. Consequently, the leaf level SIF of vegetation, recorded by a proximal sensor, requires appropriate upscaling to the canopy level SIF acquired by an airborne and to plot level as retrieved by a space-borne sensor.

Coarse spatial resolution SIF observation made by the FLEX pixel (300×300 m) may be interpreted by upscaling from the leaf and canopy level SIF observation. The spatial upscaling can be performed by properly validated leaf-to-canopy radiative transfer (RT) models (Liu et al. 2017; Tol et al. 2018). A leaf-level model integrated in a canopy RT model can possibly be validated with the actual measurement acquired from UAS sensors. Integrating multiple canopies in one RT model may enable upscaling of leaf-emitted SIF to a larger satellite image pixel size. Another potential upscaling method is matching of footprints of two sensors (Mac Arthur et al. 2013), i.e. matching spatial resolution of an UAS sensor with an air-/space-borne pixel. For example, a 25° FOV spectroradiometer can potentially be flown at about 700 m altitude to achieve a similar sized footprint to the pixel size of a future fluorescence observing space mission FLEX.

When flown at a lower height, different points within a FLEX mission pixel can be sampled with an UAS and geostatistical methods such as kriging (Oliver and Webster 1990) could be applied to interpolate and subsequently to integrate the SIF signal. Similarly, machine learning are also used for spatial upscaling/downscaling of vegetation foliage spectral signals, including SIF (Liu et al. 2018).

A general limitation of this study in relation to chlorophyll fluorescence retrieval lies in interpretation of SIF acquired over spatially heterogeneous vegetated surfaces. This work establishes a detailed understanding of the footprint geolocation, nevertheless retrieved SIF values require further processing, especially when a single footprint covers multiple targets. In that case, ancillary information is required to assist unmixing of SIF into several signal endmembers within the footprint extent.

6.3 General synopsis and future outlooks

With the research conducted in this thesis, the spatial aspects of the spectroradiometer footprint were characterised. The proposed georeferencing algorithm is expected to function over complex terrain, such as agricultural fields, grasslands, and forest stands among others. This advancement supports novel UAS-based spectroscopy applications. Still, some considerations are required concerning the desired geolocation accuracy for user-specific domains. For example, taking a spot measurement over a very large homogeneous flat terrain (e.g. a large grassland), a navigation-grade IMU and single frequency GNSS is sufficient. To acquire measurement of features such as different crop fields, a navigation-grade IMU and a multi-constellation multi-frequency GNSS receiver (survey-grade) are required. Further smaller features such as a tree canopy requires a medium-grade IMU coupled with survey-grade GNSS receiver. Finally, studying fragmented vegetation in fine detail (e.g. individual vineyard rows) requires a high-grade IMU and a survey-grade GNSS combined with a narrow spectroradiometer FOV. Consequently, an amount of uncertainty acceptable for a particular application dictates the quality of the GNSS/IMU and the challenges in for example calibration of the sensors to achieve acceptable accuracy.

This study opens up multiple venues for further improvements opportunities. The first possible improvement is an increase in geolocation accuracy by incorporating techniques such as machine vision and Kalman filtering. These techniques help reduce the spectroradiometer position and orientation uncertainty. Additional improvement in the technique of geolocation may be achieved by adopting a vision-based instead of the GNSS/IMU-based footprint estimation. A next potential advancement is an identification and clas-

sification of various objects located within the footprint extent. The knowledge about heterogeneous targets within the footprint extent can assist with unmixing of acquired radiance. Depending on acquisition altitude, the footprint size can be relatively large. With object area identification and subsequent spectral un-mixing, the separation of spectrally distinct objects recorded within a single footprint signal may be achievable.

This study opens up multiple new application opportunities. The most prominent opportunity is the use of a UAS-mounted spectroradiometer in lieu of hand-held field-based spectroradiometer for non-invasive sampling of remote and inaccessible vegetation types (e.g. sampling of high tree canopies or sampling of fragile alpine and polar vegetation, etc.). With accurate geolocation, the spectroradiometer when co-mounted with other spectral sensors (such as a multispectral camera, spectral 2D imager, and a pushbroom spectrometer), can help with *in situ* spectral calibration and validation of the co-mounted sensors. Finally, the footprint information enables detail spatial interpretation of optical signals acquired within larger spatial units of medium and low spatial resolution satellite images, e.g. 300×300 m pixels of the future ESA's FLEX/FLORIS sensor. Thus, the UAS-mounted spectroradiometer is an ideal tool for upscaling to and validation of regional-to-global space-borne observations.

References

Aasen, H. and Bolten, A. (2018). Multi-temporal high-resolution imaging spectroscopy with hyperspectral 2D imagers–From theory to application. *Remote Sensing of Environment* 205, pp. 374–389.

Aasen, H., Burkart, A., Bolten, A., and Bareth, G. (2015). Generating 3D hyperspectral information with lightweight UAV snapshot cameras for vegetation monitoring: From camera calibration to quality assurance. *ISPRS Journal of Photogrammetry and Remote Sensing* 108, pp. 245–259.

Aasen, H., Honkavaara, E., Lucieer, A., and Zarco-Tejada, P. (2018). Quantitative Remote Sensing at Ultra-High Resolution with UAV Spectroscopy: A Review of Sensor Technology, Measurement Procedures, and Data Correction Workflows. *Remote Sensing* 10 (7), p. 1091.

Ač, A., Malenovský, Z., Olejníčková, J., Gallé, A., Rascher, U., and Mohammed, G. (2015). Meta-analysis assessing potential of steady-state chlorophyll fluorescence for remote sensing detection of plant water, temperature and nitrogen stress. *Remote sensing of environment* 168, pp. 420–436.

Adamson, A. and Alexa, M. (2003). Ray tracing point set surfaces. *Shape Modeling International, 2003.* IEEE, pp. 272–279.

Advanced Navigation Spatial Dual. Available online: `http://www.advancednavigation.com.au/product/spatial-dual/` (accessed on 16 Jan 2018).

Ahokas, E, Kaartinen, H, Kukko, A, and Litkey, P (2014). Test field for airborne laser scanning in Finland. *ISPRS-International Archives of the Photogrammetry, Remote Sensing and Spatial Information Sciences* 1, pp. 9–12.

Alonso, L., Gomez-Chova, L., Vila-Frances, J., Amoros-Lopez, J., Guanter, L., Calpe, J., and Moreno, J. (2008). Improved Fraunhofer Line Discrimination method for vegetation fluorescence quantification. *IEEE Geoscience and Remote Sensing Letters* 5 (4), pp. 620–624.

Atkinson, P.M. and Curran, P.J. (1995). Defining an Optimal Size of Support for Remote Sensing Investigations. *IEEE Transactions on Geoscience and Remote Sensing* 33 (3), pp. 768–776.

Autodesk AutoCAD. Available online: `https://www.autodesk.com/products/autocad/overview` (accessed on 16 Jan 2018).

Balletti, C., Guerra, F., Tsioukas, V., and Vernier, P. (2014). Calibration of action cameras for photogrammetric purposes. *Sensors* 14 (9), pp. 17471–17490.

Belongie, S. (2018). Rodrigues' rotation formula. *From MathWorld–A Wolfram Web Resource, created by Eric W. Weisstein.* *http://mathworld.wolfram.com/RodriguesRotationFormula.html*.

Belward, A.S. and Skøien, J.O. (2015). Who launched what, when and why; trends in global land-cover observation capacity from civilian earth observation satellites. *ISPRS Journal of Photogrammetry and Remote Sensing* 103, pp. 115–128.

Bendig, J., Gautam, D., Malenovsky, Z., and Lucieer, A. (2018). Influence of Cosine Corrector and Uas Platform Dynamics on Airborne Spectral Irradiance Measurements. *IGARSS 2018 - 2018 IEEE International Geoscience and Remote Sensing Symposium*, pp. 8822–8825.

Berner, P., Toms, R., Trott, K., Mamaghani, F., Shen, D., Rollins, C., and Powell, E. (2008). Technical Concepts Orientation, Rotation, Velocity and Acceleration, and the SRM. *TENA (Test & Training Enabling Architecture) project by SEDRIS*, p. 21.

Bhatt, D., Aggarwal, P., Bhattacharya, P., and Devabhaktuni, V. (2012). An enhanced mems error modeling approach based on nu-support vector regression. *Sensors* 12 (7), pp. 9448–9466.

Bueren, S.K. von, Burkart, A, Hueni, A, Rascher, U, Tuohy, M.P., and Yule, I.J. (2015). Deploying four optical UAV-based sensors over grassland: challenges and limitations. *Biogeosciences* 12 (1), pp. 163–175.

Burkart, A., Cogliati, S., Schickling, A., and Rascher, U. (2014). A novel UAV-based ultra-light weight spectrometer for field spectroscopy. *Sensors Journal, IEEE* 14 (1), pp. 62–67.

Burkart, A., Aasen, H., Alonso, L., Menz, G., Bareth, G., and Rascher, U. (2015). Angular Dependency of Hyperspectral Measurements over Wheat Characterized by a Novel UAV Based Goniometer. *Remote Sensing* 7 (1), pp. 725–746.

Caras, T., Karnieli, A., and Hedley, J. (2011). Exploring field-of-view non-uniformities produced by a hand-held spectroradiometer. *Journal of Spectral Imaging* 2 (1), a1.

Chiang, K.-W., Tsai, M.-L., and Chu, C.-H. (2012a). The development of an UAV borne direct georeferenced photogrammetric platform for ground control point free applications. *Sensors* 12 (7), pp. 9161–9180.

— (2012b). The Development of an UAV Borne Direct Georeferenced Photogrammetric Platform for Ground Control Point Free Applications. *Sensors* 12 (7), pp. 9161–9180.

Chiang, K.-W., Tsai, M.-L., Naser, E.-S., Habib, A., and Chu, C.-H. (2015). New calibration method using low cost mem imus to verify the performance of uav-borne mms payloads. *Sensors* 15 (3), pp. 6560–6585.

Cogliati, S., Rossini, M., Julitta, T., Meroni, M., Schickling, A., Burkart, A., Pinto, F., Rascher, U., and Colombo, R. (2015a). Continuous and long-term measurements of reflectance and sun-induced chlorophyll fluorescence by using novel automated field spectroscopy systems. *Remote Sensing of Environment* 164, pp. 270–281.

Cogliati, S, Verhoef, W, Kraft, S, Sabater, N, Alonso, L, Vicent, J, Moreno, J, Drusch, M, and Colombo, R (2015b). Retrieval of sun-induced fluorescence using advanced spectral fitting methods. *Remote Sensing of Environment* 169, pp. 344–357.

Colomina, I. and Molina, P. (2014). Unmanned aerial systems for photogrammetry and remote sensing: A review. *ISPRS Journal of Photogrammetry and Remote Sensing* 92, pp. 79–97.

Coppo, P., Taiti, A., Pettinato, L., Francois, M., Taccola, M., and Drusch, M. (2017). Fluorescence imaging spectrometer (FLORIS) for ESA FLEX mission. *Remote Sensing* 9 (7), p. 649.

Daakir, M, Pierrot-Deseilligny, M, Bosser, P., Pichard, F, Thom, C., and Rabot, Y (2016). Study of lever-arm effect using embedded photogrammetry and on-board GPS receiver on UAV for metrological mapping purpose and proposal of a free ground measurements calibration procedure. *The International Archives of Photogrammetry, Remote Sensing and Spatial Information Sciences* 40, p. 65.

Dai, J.S. (2015). Euler–Rodrigues formula variations, quaternion conjugation and intrinsic connections. *Mechanism and Machine Theory* 92, pp. 144–152.

Damm, A., Guanter, L., Paul-Limoges, E., Tol, C. van der, Hueni, A., Buchmann, N., Eugster, W., Ammann, C., and Schaepman, M.E. (2015). Far-red sun-induced chlorophyll fluorescence shows ecosystem-specific relationships to gross primary pro-

duction: An assessment based on observational and modeling approaches. *Remote Sensing of Environment* 166, pp. 91–105.

Diebel, J. (2006). Representing attitude: Euler angles, unit quaternions, and rotation vectors. *Matrix* 58 (15-16), pp. 1–35.

Drusch, M., Moreno, J., Del Bello, U., Franco, R., Goulas, Y., Huth, A., Kraft, S., Middleton, E.M., Miglietta, F., Mohammed, G., and Others (2016). The FLuorescence EXplorer Mission Concept-ESA's Earth Explorer 8. *IEEE Transactions on Geoscience and Remote Sensing*.

El-Osery, A, Bruder, S, and Laughlin, D (June 2013). High-accuracy heading determination. *System of Systems Engineering (SoSE), 2013 8th International Conference on*, pp. 308–313.

Fernandez-Jaramillo, A.A., Duarte-Galvan, C., Contreras-Medina, L.M., Torres-Pacheco, I., Romero-Troncoso, R.d.J., Guevara-Gonzalez, R.G., and Millan-Almaraz, J.R. (2012). Instrumentation in developing chlorophyll fluorescence biosensing: A review. *Sensors (Switzerland)* 12 (9), pp. 11853–11869.

Frankenberg, C., Fisher, J.B., Worden, J., Badgley, G., Saatchi, S.S., Lee, J.-E., Toon, G.C., Butz, A., Jung, M., Kuze, A., et al. (2011). New global observations of the terrestrial carbon cycle from GOSAT: Patterns of plant fluorescence with gross primary productivity. *Geophysical Research Letters* 38 (17).

Gabrlik, P., Jelinek, A., and Janata, P. (2016). Precise Multi-Sensor Georeferencing System for Micro UAVs. *IFAC-PapersOnLine* 49 (25), pp. 170–175.

Garzonio, R., Di Mauro, B., Colombo, R., and Cogliati, S. (2017). Surface Reflectance and Sun-Induced Fluorescence Spectroscopy Measurements Using a Small Hyperspectral UAS. *Remote Sensing* 9 (5), p. 472.

Gautam, D. and Ha, C. (2013). Control of a quadrotor using a smart self-tuning fuzzy PID controller. *International Journal of Advanced Robotic Systems* 10.

Gautam, D., Lucieer, A., Malenovský, Z., and Watson, C. (2017). Comparison of MEMS-Based and FOG-Based IMUs to Determine Sensor Pose on an Unmanned Aircraft System. *Journal of Surveying Engineering* 143 (4), p. 4017009.

Gautam, D., Watson, C., Lucieer, A., and Malenovskỳ, Z. (2018). Error budget for geolocation of spectroradiometer point observations from an Unmanned Aircraft System. *Sensors* 18 (10), p. 3465.

Geoscience Australia. Available online: `http://www.ga.gov.au/` (accessed on 16 Jan 2018).

Gerke, M. and Przybilla, H.-J. (2016). Accuracy Analysis of Photogrammetric UAV Image Blocks: Influence of Onboard RTK-GNSS and Cross Flight Patterns. *Photogrammetrie Fernerkundung Geoinformation* 2016 (1), pp. 17–30.

Glassner, A.S. (1989). *An introduction to ray tracing*. Elsevier.

Glennie, C. (2007). Rigorous 3D error analysis of kinematic scanning LIDAR systems. *Journal of Applied Geodesy jag* 1 (3), pp. 147–157.

Guanter, L., Zhang, Y., Jung, M., Joiner, J., Voigt, M., Berry, J.A., Frankenberg, C., Huete, A.R., Zarco-Tejada, P., Lee, J.-E., et al. (2014). Global and time-resolved monitoring of crop photosynthesis with chlorophyll fluorescence. *Proceedings of the National Academy of Sciences* 111 (14), E1327–E1333.

Habib, A., Bang, K.I., Kersting, A.P., and Chow, J. (2010). Alternative methodologies for LiDAR system calibration. *Remote Sensing* 2 (3), pp. 874–907.

Hanrahan, P. (1983). Ray tracing algebraic surfaces. *ACM SIGGRAPH Computer Graphics*. Vol. 17. 3. ACM, pp. 83–90.

Harwin, S. and Lucieer, A. (2012). Assessing the accuracy of georeferenced point clouds produced via multi-view stereopsis from Unmanned Aerial Vehicle (UAV) imagery. *Remote Sensing* 4 (6), pp. 1573–1599.

Harwin, S., Lucieer, A., and Osborn, J. (2015). The impact of the calibration method on the accuracy of point clouds derived using unmanned aerial vehicle multi-view stereopsis. *Remote Sensing* 7 (9), pp. 11933–11953.

Houborg, R., Fisher, J.B., and Skidmore, A.K. (2015). Advances in remote sensing of vegetation function and traits. *International Journal of Applied Earth Observation and Geoinformation*.

Hruska, R., Mitchell, J., Anderson, M., and Glenn, N.F. (2012). Radiometric and geometric analysis of hyperspectral imagery acquired from an unmanned aerial vehicle. *Remote Sensing* 4 (9), pp. 2736–2752.

Jaud, M., Le Dantec, N., Ammann, J., Grandjean, P., Constantin, D., Akhtman, Y., Barbieux, K., Allemand, P., Delacourt, C., and Merminod, B. (2018). Direct georeferencing of a pushbroom, lightweight hyperspectral system for mini-UAV applications. *Remote Sensing* 10 (2), p. 204.

Jiang, C., Xue, L., Chang, H., Yuan, G., and Yuan, W. (2012). Signal processing of MEMS gyroscope arrays to improve accuracy using a 1st order markov for rate signal modeling. *Sensors* 12 (2), pp. 1720–1737.

Joseph, G. (2005). *Fundamentals of remote sensing*. Universities press.

Jozkow, G, Toth, C, and Grejner-Brzezinska, D (2016). UAS topographic mapping with velodyne LiDAR sensor. *ISPRS Annals of the Photogrammetry, Remote Sensing and Spatial Information Sciences* 3, p. 201.

Julitta, T. (2018a). *R package for Characterization and Calibration of spectrometers*. `https://github.com/tommasojulitta/FieldSpectroscopyCC`.

— (2018b). *R package for processing fieldspectroscopy data*. `https://github.com/tommasojulitta/FieldSpectroscopyDP`.

Julitta, T., Corp, L.A., Rossini, M., Burkart, A., Cogliati, S., Davies, N., Hom, M., Arthur, A.M., Middleton, E.M., Rascher, U., Schickling, A., and Colombo, R. (2016). Comparison of sun-induced chlorophyll fluorescence estimates obtained from four portable field spectroradiometers. *Remote Sensing* 8 (2).

Kennedy, S. and Rossi, J. (2008). Performance of a deeply coupled commercial grade GPS/INS system from KVH and NovAtel Inc. *Position, Location and Navigation Symposium, 2008 IEEE/ION*. IEEE, pp. 17–24.

Kennedy, S., Hamilton, J., and Hinuber, E.v. (2005). Integration of Inertial Measurements with GNSS-NovAtel SPAN Architecture. *Symposium Gyro Technology*. Vol. 2005, p. 18.

Kennedy, S., Hamilton, J., and Martell, H. (2006). Architecture and system performance of SPAN–NovAtel's GPS/INS solution. *Proceedings of IEEE/ION PLANS 2006*, pp. 23–25.

Khodadadzadeh, M., Li, J., Plaza, A., Ghassemian, H., Bioucas-Dias, J.M., and Li, X. (2014). Spectral–spatial classification of hyperspectral data using local and global probabilities for mixed pixel characterization. *IEEE Transactions on Geoscience and Remote Sensing* 52 (10), pp. 6298–6314.

Kraft, S., Del Bello, U., Harnisch, B., Bouvet, M., Drusch, M., and Bézy, J.-L. (2017). Fluorescence imaging spectrometer concepts for the earth explorer mission candidate FLEX. *International Conference on Space Optics—ICSO 2012*. Vol. 10564. International Society for Optics and Photonics, 105641W.

Lange, M., Dechant, B., Rebmann, C., Vohland, M., Cuntz, M., and Doktor, D. (2017). Validating MODIS and sentinel-2 NDVI products at a temperate deciduous forest site using two independent ground-based sensors. *Sensors* 17 (8), p. 1855.

Li, D., Landry Jr, R., and Lavoie, P. (2008). Low-cost MEMS sensor-based attitude determination system by integration of magnetometers and GPS: A real-data test and performance evaluation. *Position, Location and Navigation Symposium, 2008 IEEE/ION*. IEEE, pp. 1190–1198.

Li, Y., Efatmaneshnik, M., and Dempster, A.G. (2012). Attitude determination by integration of MEMS inertial sensors and GPS for autonomous agriculture applications. *GPS solutions* 16 (1), pp. 41–52.

Lichti, D.D., Gordon, S.J., and Tipdecho, T. (2005). Error models and propagation in directly georeferenced terrestrial laser scanner networks. *Journal of surveying engineering* 131 (4), pp. 135–142.

Lin, Y., Hyyppa, J., and Jaakkola, A. (2011). Mini-UAV-borne LIDAR for fine-scale mapping. *IEEE Geoscience and Remote Sensing Letters* 8 (3), pp. 426–430.

Liu, L. and Cheng, Z. (2010). Detection of vegetation light-use efficiency based on solar-induced chlorophyll fluorescence separated from canopy radiance spectrum. *IEEE Journal of Selected Topics in Applied Earth Observations and Remote Sensing* 3 (3), pp. 306–312.

Liu, W., Atherton, J., Mõttus, M., MacArthur, A., Teemu, H., Maseyk, K., Robinson, I., Honkavaara, E., and Porcar-Castell, A. (2017). Upscaling of solar induced chlorophyll fluorescence from leaf to canopy using the dart model and a realistic 3D forest scene. *International Archives of the Photogrammetry, Remote Sensing & Spatial Information Sciences* 42.

Liu, X., Guanter, L., Liu, L., Damm, A., Malenovský, Z., Rascher, U., Peng, D., Du, S., and Gastellu-Etchegorry, J.P. (2018). Downscaling of solar-induced chlorophyll fluorescence from canopy level to photosystem level using a random forest model. *Remote Sensing of Environment* (9).

Lord Sensing MicroStrain. Available online: `http://www.microstrain.com/inertial/3dm-gx3-35/` (accessed on 16 Jan 2018).

Lucieer, A., Robinson, S., Turner, D., Harwin, S., and Kelcey, J. (2012). Using a micro-UAV for ultra-high resolution multi-sensor observations of Antarctic moss beds. *ISPRS - International Archives of the Photogrammetry, Remote Sensing and Spatial Information Sciences* XXXIX-B1, pp. 429–433.

Lucieer, A., Malenovský, Z., Veness, T., and Wallace, L. (2014). HyperUAS-Imaging Spectroscopy from a Multirotor Unmanned Aircraft System. *Journal of Field Robotics* 31 (4), pp. 571–590.

Mac Arthur, A., MacLellan, C.J., and Malthus, T. (2012). The fields of view and directional response functions of two field spectroradiometers. *IEEE Transactions on Geoscience and Remote Sensing* 50 (10 PART1), pp. 3892–3907.

Mac Arthur, A., Alonso, L., Malthus, T., and Moreno, J. (2013). Spectroscopy field strategies and their effect on measurements of heterogenious and homogenious Earth surfaces. *ESA Living Planet Symposium* 2013 (December).

Maier, S.W. (2002). Remote sensing and modelling of solar induced fluorescence. *Remote Sensing of Solar-Induced Vegetation*. Vol. 527, p. 6.

Malenovský, Z., Mishra, K.B., Zemek, F., Rascher, U., and Nedbal, L. (2009). Scientific and technical challenges in remote sensing of plant canopy reflectance and fluorescence. *Journal of Experimental Botany* 60 (11), pp. 2987–3004.

Malenovský, Z., Homolová, L., Zurita-Milla, R., Lukeš, P., Kaplan, V., Hanuš, J., Gastellu-Etchegorry, J.-P., and Schaepman, M.E. (2013). Retrieval of spruce leaf chlorophyll content from airborne image data using continuum removal and radiative transfer. *Remote Sensing of Environment* 131, pp. 85–102.

Malenovský, Z., Ac, A., Olejnickova, J., Galle, A., Rascher, U., and Mohammed, G. (2014). Knowledge gap analysis assessing steady-state chlorophyll fluorescence as an indicator of plant stress status. *Proceeding of the 5th International Workshop on Remote Sensing of Vegetation Fluorescence*.

Malenovský, Z., Lucieer, A., King, D.H., Turnbull, J.D., and Robinson, S.A. (2017). Unmanned aircraft system advances health mapping of fragile polar vegetation. *Methods in Ecology and Evolution*.

Mancini, F., Dubbini, M., Gattelli, M., Stecchi, F., Fabbri, S., and Gabbianelli, G. (2013). Using unmanned aerial vehicles (UAV) for high-resolution reconstruction of topography: The structure from motion approach on coastal environments. *Remote Sensing* 5 (12), pp. 6880–6898.

McCoull, C. (2016). Calibration and accuracy assessments of an unmanned aerial vehicle laser scanning system. MA thesis. Hobart, Tasmania, Australia: University of Tasmania.

Meroni, M., Rossini, M., Guanter, L., Alonso, L., Rascher, U., Colombo, R., and Moreno, J. (Oct. 2009). Remote sensing of solar-induced chlorophyll fluorescence: Review of methods and applications. *Remote Sensing of Environment* 113 (10), pp. 2037–2051.

Middleton, J.H., Cooke, C.G., Kearney, E.T., Mumford, P.J., Mole, M.A., Nippard, G.J., Rizos, C, Splinter, K.D., and Turner, I.L. (2013). Resolution and accuracy of an airborne scanning laser system for beach surveys. *Journal of Atmospheric and Oceanic Technology* 30 (10), pp. 2452–2464.

Mirzaei, F.M. and Roumeliotis, S.I. (2008). A Kalman filter-based algorithm for IMU-camera calibration: Observability analysis and performance evaluation. *IEEE transactions on robotics* 24 (5), pp. 1143–1156.

Mitishita, E., Debiasi, P., Kersting, A.P., Centeno, J.A.S., and Machado, A.L. (2016). A study on in situ calibration of an off-the-shelf digital camera integrated to a LIDAR system. *IEEE Journal of Selected Topics in Applied Earth Observations and Remote Sensing* 9 (12), pp. 5513–5523.

Miura, T. and Huete, A.R. (2009). Performance of three reflectance calibration methods for airborne hyperspectral spectrometer data. *Sensors* 9 (2), pp. 794–813.

Mohammed, G.H., Colombo, R., Moreno, J., Tol, C. van der, Rascher, U., Ač, A., Alonso, L., Celesti, M., Cogilati, S., Damm, A., Fawcett, D., et al. (2016). FLEX/Sentinel-3 Tandem Mission FLEX Bridge Study. *Final report. ESA ESTEC Contract No. 4000112341/14/NL/FF/gp*.

Moreno, J, Goulas, Y, Huth, A, Middelton, E, Miglietta, F, Mohammed, G, Nebdal, L, Rascher, U, and Verhof, W (2015). Report for mission selection: CarbonSat flex - An earth explorer to observe vegetation fluorescence.

Moreno, J.F., Goulas, Y., Huth, A., Middleton, E., Miglietta, F., Mohammed, G., Nedbal, L., Rascher, U., Verhoef, W., and Drusch, M. (2016). Very high spectral resolution imaging spectroscopy: The Fluorescence Explorer (FLEX) mission. *Geoscience and Remote Sensing Symposium (IGARSS), 2016 IEEE International*. IEEE, pp. 264–267.

Mulla, D.J. (2013). Twenty five years of remote sensing in precision agriculture: Key advances and remaining knowledge gaps. *Biosystems Engineering* 114 (4), pp. 358–371.

Natesan, S., Armenakis, C., Benari, G., and Lee, R. (2018). Use of UAV-Borne Spectrometer for Land Cover Classification. *Drones* 2 (2), p. 16.

NovAtel SPAN-CPT. Available online: `https://www.novatel.com/products/span-gnss-inertial-systems/span-combined-systems/span-cpt/` (accessed on 16 Jan 2018).

Oliver, M.A. and Webster, R. (1990). Kriging: a method of interpolation for geographical information systems. *International Journal of Geographical Information System* 4 (3), pp. 313–332.

Pajares, G. (2015). Overview and Current Status of Remote Sensing Applications Based on Unmanned Aerial Vehicles (UAVs). *Photogrammetric Engineering & Remote Sensing* 81 (4), pp. 281–330.

Panigada, C., Rossini, M., Meroni, M., Cilia, C., Busetto, L., Amaducci, S., Boschetti, M., Cogliati, S., Picchi, V., Pinto, F., Marchesi, A., and Colombo, R. (2014). Fluorescence, PRI and canopy temperature for water stress detection in cereal crops. *International Journal of Applied Earth Observation and Geoinformation* 30 (1), pp. 167–178.

Parr, A.C., Datla, R., and Gardner, J. (2005). *Optical radiometry*. Vol. 41. Academic Press.

Petovello, M.G., O'Driscoll, C, and Lachapelle, G (2007). Ultra-tight GPS/INS for carrier phase positioning in weak-signal environments. *Proceedings of NATO RTO SET-104 Symposium on Military Capabilities Enabled by Advances in Navigation Sensors*.

Pinchin, J., Hide, C., Park, D., and Chen, X. (2008). Precise kinematic positioning using single frequency GPS receivers and an integer ambiguity constraint. *Position, Location and Navigation Symposium, 2008 IEEE/ION*. IEEE, pp. 600–605.

Pinto, F., Damm, A., Schickling, A., Panigada, C., Cogliati, S., Müller-Linow, M., Balvora, A., and Rascher, U. (2016). Sun-induced chlorophyll fluorescence from high-resolution imaging spectroscopy data to quantify spatio-temporal patterns of photosynthetic function in crop canopies. *Plant, cell & environment*.

Porcar-Castell, A., Tyystjärvi, E., Atherton, J., Tol, C. van der, Flexas, J., Pfündel, E.E., Moreno, J., Frankenberg, C., and Berry, J.A. (2014). Linking chlorophyll a fluorescence to photosynthesis for remote sensing applications: mechanisms and challenges. *Journal of experimental botany* 65 (15), pp. 4065–4095.

Rascher, U., Alonso, L, Burkart, A, Cilia, C, Cogliati, S, Colombo, R, Damm, A, Drusch, M, Guanter, L, Hanus, J, and Others (2015). Sun-induced fluorescence–a new probe of photosynthesis: First maps from the imaging spectrometer HyPlant. *Global change biology* 21 (12), pp. 4673–4684.

Rehak, M., Mabillard, R., and Skaloud, J. (2013). A micro-UAV with the capability of direct georeferencing. *Int. Arch. Photogramm. Remote Sens. Spatial Inf. Sci*, pp. 317–323.

Remondino, F., Barazzetti, L., Nex, F., Scaioni, M., and Sarazzi, D. (2011). UAV photogrammetry for mapping and 3d modeling–current status and future perspectives. *International archives of the photogrammetry, remote sensing and spatial information sciences* 38 (1), p. C22.

Rieger, P, Studnicka, N, Pfennigbauer, M, and Zach, G (2010). Boresight alignment method for mobile laser scanning systems. *Journal of Applied Geodesy* 4 (1), pp. 13–21.

Rossini, M, Nedbal, L, Guanter, L, Ač, A, Alonso, L, Burkart, A, Cogliati, S, Colombo, R, Damm, A, Drusch, M, and Others (2015). Red and far red Sun-induced chlorophyll fluorescence as a measure of plant photosynthesis. *Geophysical Research Letters*.

Rossini, M., Meroni, M., Celesti, M., Cogliati, S., Julitta, T., Panigada, C., Rascher, U., Tol, C. van der, and Colombo, R. (2016). Analysis of Red and Far-Red Sun-Induced Chlorophyll Fluorescence and Their Ratio in Different Canopies Based on Observed and Modeled Data. *Remote Sensing* 8 (5), p. 412.

Roth, S.D. (1982). Ray casting for modeling solids. *Computer graphics and image processing* 18 (2), pp. 109–144.

Ruiz, J.J., Diaz-Mas, L, Perez, F, and Viguria, A (2013). Evaluating the accuracy of DEM generation algorithms from UAV imagery. *Int. Arch. Photogramm. Remote Sens. Spatial Inf. Sci* 40, pp. 333–337.

Schaepman, M.E. (1998). Calibration of a field spectroradiometer. PhD thesis. Zurich University.

Schaepman-Strub, G., Schaepman, M.E., Painter, T.H., Dangel, S., and Martonchik, J.V. (2006). Reflectance quantities in optical remote sensing-definitions and case studies. *Remote Sensing of Environment* 103 (1), pp. 27–42.

Schaer, P, Skaloud, J, Landtwing, S, and Legat, K (2007). Accuracy Estimation for Laser Point Cloud Including Scanning Geometry. *The International Archives of the Photogrammetry, Remote Sensing and Spatial Information Sciences*. TOPO-CONF-2008-015, N/A.

Schwarz, K.P. and El-Sheimy, N. (2004). Mobile Mapping Systems – State of the art and future trends. *TS SS3 - Mobile Multi-sensor System*.

Skaloud, J. and Lichti, D. (2006). Rigorous approach to bore-sight self-calibration in airborne laser scanning. *ISPRS journal of photogrammetry and remote sensing* 61 (1), pp. 47–59.

Slater, P.N. (1985). Radiometric considerations in remote sensing. *Proceedings of the IEEE* 73 (6), pp. 997–1011.

Suomalainen, J., Anders, N., Iqbal, S., Roerink, G., Franke, J., Wenting, P., Hünniger, D., Bartholomeus, H., Becker, R., and Kooistra, L. (2014). A lightweight hyperspectral mapping system and photogrammetric processing chain for unmanned aerial vehicles. *Remote Sensing* 6 (11), pp. 11013–11030.

Takasu, T. and Yasuda, A. (2009). Development of the low-cost RTK-GPS receiver with an open source program package RTKLIB. *international symposium on GPS/GNSS*. International Convention Centre Jeju, Korea, pp. 4–6.

Thenkabail, P.S. and Lyon, J.G. (2016). *Hyperspectral remote sensing of vegetation*. CRC Press.

Tol, C. van der, Verhoef, W., and Rosema, A. (Jan. 2009). A model for chlorophyll fluorescence and photosynthesis at leaf scale. *Agricultural and Forest Meteorology* 149 (1), pp. 96–105.

Tol, C. van der, Vilfan, N., Yang, P., Bayat, B., and Verhoef, W. (2018). Modeling Reflectance, Fluorescence and Photosynthesis: Development of the Scope Model. *IGARSS 2018 - 2018 IEEE International Geoscience and Remote Sensing Symposium* 2 (1), pp. 5968–5971.

Tu, Y.-H., Phinn, S., Johansen, K., and Robson, A. (2018). Assessing Radiometric Correction Approaches for Multi-Spectral UAS Imagery for Horticultural Applications. *Remote Sensing* 10 (11), p. 1684.

Turner, D, Lucieer, A, McCabe, M., Parkes, S., and Clarke, I (2017). Pushbroom hyperspectral imaging from an unmanned aircraft system (UAS)–geometric processing workflow and accuracy assessment. *The International Archives of Photogrammetry, Remote Sensing and Spatial Information Sciences* 42, p. 379.

Turner, D., Lucieer, A., and Watson, C. (May 2012a). An Automated Technique for Generating Georectified Mosaics from Ultra-High Resolution Unmanned Aerial Vehicle (UAV) Imagery, Based on Structure from Motion (SfM) Point Clouds. en. *Remote Sensing* 4 (12), pp. 1392–1410.

— (2012b). An automated technique for generating georectified mosaics from ultra-high resolution unmanned aerial vehicle (UAV) imagery, based on structure from motion (SfM) point clouds. *Remote Sensing* 4 (5), pp. 1392–1410.

Turner, D., Lucieer, A., and Wallace, L. (2014a). Direct georeferencing of ultrahigh-resolution UAV imagery. *IEEE Transactions on Geoscience and Remote Sensing* 52 (5), pp. 2738–2745.

Turner, D., Lucieer, A., Malenovský, Z., King, D.H., and Robinson, S.A. (2014b). Spatial co-registration of ultra-high resolution visible, multispectral and thermal images acquired with a micro-UAV over antarctic moss beds. *Remote Sensing* 6 (5), pp. 4003–4024.

Turner, D., Lucieer, A., Malenovský, Z., King, D.H., and Robinson, S.A. (2014c). Spatial co-registration of ultra-high resolution visible, multispectral and thermal images acquired with a micro-UAV over Antarctic moss beds. *Remote Sensing* 6 (5), pp. 4003–4024.

Uysal, M, Toprak, A., and Polat, N (2015). DEM generation with UAV Photogrammetry and accuracy analysis in Sahitler hill. *Measurement* 73, pp. 539–543.

Vali, V. and Shorthill, R.W. (1976). Fiber ring interferometer. *Appl. Opt* 15 (5), pp. 1099–1100.

Verrelst, J., Rivera, J.P., Leonenko, G., Alonso, L., and Moreno, J. (2014). Optimizing LUT-based RTM inversion for semiautomatic mapping of crop biophysical parameters from Sentinel-2 and-3 data: Role of cost functions. *IEEE Transactions on Geoscience and Remote Sensing* 52 (1), pp. 257–269.

Verrelst, J., Tol, C. van der, Magnani, F., Sabater, N., Rivera, J.P., Mohammed, G., and Moreno, J. (2016). Evaluating the predictive power of sun-induced chlorophyll fluorescence to estimate net photosynthesis of vegetation canopies: A scope modeling study. *Remote Sensing of Environment* 176, pp. 139–151.

Wallace, L., Lucieer, A., Turner, D., Watson, C., and Others (2011). Error assessment and mitigation for hyper-temporal UAV-borne LiDAR surveys of forest inventory. *Proceedings of Silvilaser*.

Wallace, L., Lucieer, A., Watson, C., and Turner, D. (May 2012). Development of a UAV-LiDAR system with application to forest inventory. *Remote Sensing* 4 (6), pp. 1519–1543.

Weiss, S., Achtelik, M.W., Chli, M., and Siegwart, R. (2012). Versatile distributed pose estimation and sensor self-calibration for an autonomous MAV. *Robotics and Automation (ICRA), 2012 IEEE International Conference on*. IEEE, pp. 31–38.

Weyermann, J., Damm, A., Kneubuhler, M., and Schaepman, M.E. (2014). Correction of reflectance anisotropy effects of vegetation on airborne spectroscopy data and derived products. *IEEE Transactions on Geoscience and Remote Sensing* 52 (1), pp. 616–627.

Wieneke, S, Ahrends, H, Damm, A, Pinto, F, Stadler, A, Rossini, M, and Rascher, U (2016). Airborne based spectroscopy of red and far-red sun-induced chlorophyll fluorescence: Implications for improved estimates of gross primary productivity. *Remote Sensing of Environment* 184, pp. 654–667.

Wilkinson, B.E., Mohamed, A.H., Dewitt, B.A., and Seedahmed, G.H. (2010). A novel approach to terrestrial LiDAR georeferencing. *Photogrammetric Engineering & Remote Sensing* 76 (6), pp. 683–690.

Williams, K., Olsen, M.J., Roe, G.V., and Glennie, C. (2013). Synthesis of transportation applications of mobile LiDAR. *Remote Sensing* 5 (9), pp. 4652–4692.

Woodman, O.J. (2007). *An introduction to inertial navigation.* Tech. rep. University of Cambridge, Computer Laboratory.

Wu, C., Niu, Z., Tang, Q., and Huang, W. (2008). Estimating chlorophyll content from hyperspectral vegetation indices: Modeling and validation. *agricultural and forest meteorology* 148 (8), pp. 1230–1241.

Wyber, R. (2018). Linking spectral signals with novel photosynthetic parameters from the leaf to the canopy. PhD thesis. University of Wollongong.

Wyber, R., Malenovský, Z., Ashcroft, M.B., Osmond, B., and Robinson, S.A. (2017). Do Daily and Seasonal Trends in Leaf Solar Induced Fluorescence Reflect Changes in Photosynthesis, Growth or Light Exposure? *Remote Sensing* 9 (6), p. 604.

Yang, P., Tol, C. van der, Verhoef, W., Damm, A., Schickling, A., Kraska, T., Muller, O., and Rascher, U. (2018). Using reflectance to explain vegetation biochemical and structural effects on sun-induced chlorophyll fluorescence. *Remote Sensing of Environment* (November).

Yastikli, N. and Jacobsen, K. (2005). Influence of system calibration on direct sensor orientation. *Photogrammetric Engineering & Remote Sensing* 71 (5), pp. 629–633.

Zarco-Tejada, P.J., Berni, J.A.J., Suárez, L., Sepulcre-Cantó, G, Morales, F, and Miller, J.R. (2009). Imaging chlorophyll fluorescence with an airborne narrow-band multispectral camera for vegetation stress detection. *Remote Sensing of Environment* 113 (6), pp. 1262–1275.

Zarco-Tejada, P., Miller, J., Haboudane, D., Tremblay, N., and Apostol, S. (2003). Detection of chlorophyll fluorescence in vegetation from airborne hyperspectral CASI imagery in the red edge spectral region. *IGARSS 2003. 2003 IEEE International Geoscience and Remote Sensing Symposium. Proceedings (IEEE Cat. No.03CH37477)* 1.

Zarco-Tejada, P., Catalina, A., González, M., and Martín, P. (Sept. 2013a). Relationships between net photosynthesis and steady-state chlorophyll fluorescence retrieved from airborne hyperspectral imagery. *Remote Sensing of Environment* 136, pp. 247–258.

Zarco-Tejada, P., Morales, A., Testi, L., and Villalobos, F. (2013b). Spatio-temporal patterns of chlorophyll fluorescence and physiological and structural indices acquired from hyperspectral imagery as compared with carbon fluxes measured with eddy covariance. *Remote Sensing of Environment* 133, pp. 102–115.

Zarco-Tejada, P., González-Dugo, M., and Fereres, E (2016). Seasonal stability of chlorophyll fluorescence quantified from airborne hyperspectral imagery as an indicator of net photosynthesis in the context of precision agriculture. *Remote sensing of environment* 179, pp. 89–103.

Zecha, C., Link, J, and Claupein, W (2013). Mobile sensor platforms: categorisation and research applications in precision farming. *Journal of Sensors and Sensor Systems* 2 (1), pp. 51–72.

Zeng, C., King, D.J., Richardson, M., and Shan, B. (2017). Fusion of Multispectral Imagery and Spectrometer Data in UAV Remote Sensing. *Remote Sensing* 9 (7), p. 696.

Zhang, C. and Kovacs, J.M. (2012). The application of small unmanned aerial systems for precision agriculture: a review. *Precision agriculture* 13 (6), pp. 693–712.

Zhang, Y., Guanter, L., Berry, J.A., Joiner, J., Tol, C., Huete, A., Gitelson, A., Voigt, M., and Köhler, P. (2014). Estimation of vegetation photosynthetic capacity from space-based measurements of chlorophyll fluorescence for terrestrial biosphere models. *Global change biology* 20 (12), pp. 3727–3742.

Zhang, Y. and Shen, X. (2013). Direct georeferencing of airborne LiDAR data in national coordinates. *ISPRS journal of photogrammetry and remote sensing* 84, pp. 43–51.

Zhao, Y., Horemuz, M., and Sjöberg, L.E. (2011). Stochastic modelling and analysis of IMU sensor errors. *Archiwum Fotogrametrii, Kartografii i Teledetekcji* 22.